Kelly, Damien P.:

Paraxial wave optics

URN: urn:nbn:de:gbv:ilm1-2017000390

Paraxial wave optics

Dissertation zur Erlangung des
akademischen Grades Doktor-Habilitation (Dr. Habil)

vorgelegt der Fakultaet Maschinenbau
der Technischen Unierstitaet Ilmenau

von Juniorprofessor Damien P. Kelly, B.E., PhD

Doktorvater Prof. Dr. John T. Sheridan

1. Gutachter: Prof Dr. rer. nat. habil Stefan Sinzinger
2. Gutachter Prof. Dr. Pascal Picart
3. Gutacther Prof. Dr. Steen Hanson

Tag der Einreichung: 14.03.2016
Tag der Wissenschaftlichen Aussprache: 4.07.2017

urn:nbn:de:gbv:ilm1-2017000390

Contents

Acknowledgements

What began in August 2010 was another chapter in my life. I had been home, employed on a happy post-doc contract under the guidance my good fellow-traveller Bryan Hennelly. And now, an opportunity for a solid six years research project - in a foreign land. No sooner than I left Ireland, I witnessed from abroad its surreal collapse; there wasn't a happier German taxpayer!

My position was funded by the Carl-Zeiss-Stiftung. I was left alone for my studies, submitting only occasional progress reports and I am grateful, entirely grateful, for this period of monastic study. It is a testament to the longevity and quality of the German academic system that the concept of 'research independence' is not yet expressed in the 'mathematical' form of a Gantt chart.

I must of course first acknowledge my new German colleagues who have made my time here in Germany the success it has been. Stefan Sinzinger has welcomed me into his extended group, allowed me to work within it and to contribute where possible and in an always open manner to any on-going project. It is difficult to overstate how much I have learned from him during this intense period - from mathematics to simple experimental detail. Karolin Schuster has always been able to help untangle administrative knots, Thomas Meinecke to help me understand speckle and sport, Matthias Hillenbrand taught me much about non-paraxial diffraction integrals, Beate Mitschunas about geometric optics, Ralf Weber about cinema and laser safety. There has been a continuous stream of PhD students and post-docs from Ireland during my time who have contributed so much in terms of successful projects, publications and positivity. Special mentions to the Chinese, Dayan Li, Yang Wu, and Liang Zhao. There are of course so many more.

My parents too have always been there, supporting and counselling. Other family as well; my sister Amelia and Ollie, Madeleine and Sam whose hospitality this time last year gave me a lift when I needed it. And, after so much circling to my love Bediha. I

met her shortly after I arrived in Germany, in a small dance club in Berlin. We have been together ever since. None of this would have been possible without her, she has been unwavering in her support and tells funny jokes. It is to her that I dedicate this work.

Damien P. Kelly,

Berlin, 14 March 2016.

Preface

The material presented in this thesis is based on some of the research work I have conducted since I completed my PhD in 2006. The totality of this research work takes the form of 41 technical papers that are cited in the References section. These papers are both conference proceedings and journal papers as well as several book chapters. Naturally the work of a great many researchers the world over and over many generations have contributed to a very broad literature in optics, which are liberally cited in my own publications but are not cited in this thesis.

Here I have decided to emphasise my own contributions to the field. All of the arguments I make in this thesis are based on conclusions and insights from my own research work and hence it is only that work which I reference. I hope that the interested reader will understand my motivation for this unusual approach and can find extra supporting material in my own papers.

Damien P. Kelly,
Berlin, 14 March 2016.

Chapter 1

The propagation of light

And God said, "let there be light," and there was light. God saw that the light was good, and he separated the light from the darkness. God called the light 'day' and the darkness 'night.' And there was evening, and there was morning - the first day.

1.1 Useful models

The most widely published and one of the more controversial books in the Western canon gives some indication of the importance the ancients attached to this mysterious phenomenon which was widely studied then, particularly in the Islamic world. Initial study of this problem developed some of the fundamental principles of geometrical optics. Light was thought of as being made up of rays that travelled along straight lines. This model led to the development of structures to focus and bend light to a geometrical point to create burning mirrors and lenses, which is first attributed to an Iraqi scholar Ibn Sahl. The initial study of light was and remains inextricably interlinked with the nature of matter. Newton's view for example is summarized as follows:

"All space is permeated by an elastic medium or aether, which is capable of propagating vibrations in the same way as the air propagates the vibrations of sound, but with far greater velocity. This aether pervades the pores of all material bodies, and is the cause of their cohesion; its density varies from one body to another, being greatest in the free interplanetary spaces. It is not necessarily a single uniform substance: but just as air contains aqueous vapour, so the aether may contain various 'aethereal spirits,' adapted to produce the phenomena of electricity, magnetism and gravitation. The vibrations of the aether cannot, for the reasons already mentioned, be supposed in themselves to constitute light. Light is therefore taken to be something of a different kind, propagated from lucid bodies. They, that will, may suppose it an aggregate of various peripatetic qualities.

Others may suppose it multitudes of unimaginable small and swift corpuscles of various sizes, springing from shining bodies at great distances one after another; but yet without any sensible interval of time, and continually urged forward by a principle of motion, which in the beginning accelerates them, till the resistance of the aethereal medium equals the force of that principle, much after the manner that bodies let fall in water are accelerated till the resistance of the water equals the force of gravity. But they, that like not this, may suppose light any other corporeal emanation, or any impulse or motion of any other medium or aethereal spirit diffused through the main body of aether, or what else they can imagine proper for this purpose. To avoid dispute, and make this hypothesis general, let every man here take his fancy; only whatever light be, I suppose it consists of rays differing from one another in contingent circumstances, as bigness, form or vigour." [1]

Here Newton describes some properties of the aether and appears to indicate that he views light as consisting of rays. A second viewpoint, also alluded to, considers light to be vibrations of the aether. A position which was advocated by an older colleague, Hooke - a bitter dispute. Maxwell derived a set of equations which provided a unified theory for magnetism, electricity, current and light - viewing light as an electromagnetic wave propagating through the aether. The search for the aether was subsequently given up following that most famous negative result in physics - the Michelson-Morley experiment. Einstein won the Nobel prize in physics for his explanation of the photo-electric effect, which lay outside Maxwell's theoretical framework. Within a few years everything was swept away with the emergence of quantum theory and matter waves. While Euclid would have been comfortable with modern ray tracing for optic design, quantum optics would be unexpected.

It is not our purpose here to weigh in on a long-standing philosophical debate - we have nothing to say about it. The engineer picks a model suitable for her purposes; sometimes that may be a quantum mechanical model or sometimes it reduces to tracing the path of optical rays through a Euclidian space. For our purposes, a model is sensible when it provides unique and consistent explanations and a methodology for analysis; and is deemed useful when the resulting theoretical predictions conform to observable results.

Polarization was recognized as a significant problem for the wave theory of light until Fresnel provided an explanation consistent with wave motion. Light was now seen as being a transverse wave which oscillates perpendicularly to the direction of motion in

[1] This viewpoint is attributed to Newton in the following text: 'A history of the theories of Aether and Electricity' by E. Whittaker

free space. Different polarizations of light thus vibrate along orthogonal axes. This is different from sound which is a longitudinal wave - oscillating along the direction of propagation. Fresnel made further contributions supporting a wave interpretation of light. Fresnel's diffraction theory won him a prestigious award from the 'French Academy of Sciences' in 1818 for his explanation of the propagation of light. But not before Poisson, a member of the committee, used Fresnel's theory to predict an outrageous result. A prediction that was later confirmed to be true by Arago in an experiment. Fresnel's diffraction model is a scalar theory of light propagation, i.e. it only considers a single polarization component of a light field. A scalar diffraction integral can be derived from Maxwell's equations provided some important assumptions hold, see [40], and the references within. When these conditions hold we speak of light as being a scalar phenomena or better: The different orthogonal vectorial components of light do not 'see' each other and hence each component can be treated as separate scalar problems. Using a scalar theory for light greatly simplifies analysis. And as Poisson found out, it also provides a valid description of the behavior of light for a large range of situations. Scalar theory becomes increasingly inaccurate in the following situations:

- Diffraction from apertures when the aperture size is comparable to the wavelength,
- Propagation through in-homogenous media,
- Focusing by high numerical apertures,
- Anisotropic media including some crystals.

In all the considerations presented in this, it is assumed that the scalar description of light phenomena is valid.

Within the scalar description of light propagation it is useful to distinguish two sub-groups: Non-paraxial and paraxial diffraction integrals. Both types of diffraction integrals can be derived from Maxwell's equations, [11], however the paraxial treatment requires that more approximations are made in the derivation process. Hence the paraxial model seems further removed from the real underlying physical processes of diffraction, with the result that the non-paraxial diffraction integrals are considered to be more accurate. We accordingly catagorize the Kirchhoff or Raleigh-Sommerfeld I and II as non-paraxial diffraction integrals [4, 5]. The Fresnel transform is a paraxial diffraction integral and now serves as our 'useful model' for describing the propagation of light.

1.2 The Fresnel transform

We must begin by first discussing some fundamental properties of this scalar optical field. The idea of scalar optical field is of something that permeates both space and time. Initially we will examine light at a given instant in time, which is standard in the treatment of paraxial optical problems. However later in this chapter we will discuss the propagation of light pulses re-introducing a time component.

The scalar optical fields examined here are thus defined in space; at each spatial location the optical field is given by a complex number having both a real part and an imaginary part. Or equivalently an intensity (square of the magnitude) and a phase value. We shall see that measuring the intensity of an optical field is not difficult, however detecting the correct phase value is much more problematic. We begin our analysis by considering the schematic shown in Fig. 1.1. In this diffraction problem it is given that we know the complex amplitude of a particular optical wavefield in the input plane, defined with the spatial variable X. The diffraction problem then amounts to determining what the optical field is in other optical planes.

In what follows, for notational simplicity, we will perform a 1-D analysis. The field in Plane 1, denoted with uppercase letters $U(X)$, is assumed to be known and our task is to find an expression for the diffracted field, $u_z(x)$ in Plane 2. We now write the formal definition of the Fresnel transform [19]:

$$\begin{aligned} u_z(x) &= \mathrm{FST}_z\left\{U(X)\right\}(x) \\ &= \frac{\exp\left(j2\pi z/\lambda\right)}{\sqrt{j\lambda z}} \int_{-\infty}^{\infty} U(X) \exp\left[\frac{j\pi}{\lambda z}\left(x-X\right)^2\right] dX, \end{aligned} \tag{1.1}$$

where λ is the wavelength of the monochromatic and coherent (both temporally and spatially) light, z is the axial distance between Plane 1 and Plane 2 (see Fig. 1), $j = \sqrt{-1}$, and the variables X and x refer to the spatial coordinates in Plane 1 and Plane 2 respectively. We will drop the leading phase term, $\exp\left(j2\pi z/\lambda\right)$, for the rest of the analysis but reintroduced during our later discussion of pulses.

In some diffraction problems it is possible to solve the integral in Eq. (1.1) analytically. These solutions are important for several reasons; they provide significant insight into the diffraction process, and they also serve as a means of assessing the accuracy of a numerical approach. This can be achieved by comparing the results of a numerical calculation directly against those produced by the correct analytical solution.

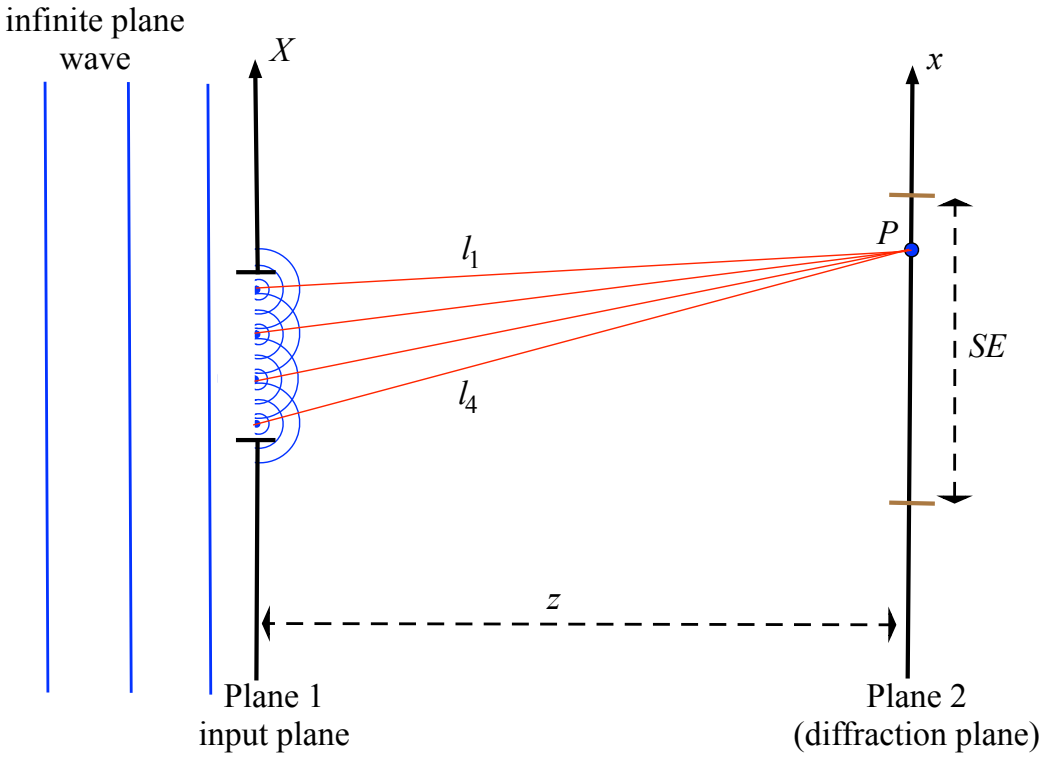

Figure 1.1 – Illustration of the diffraction process. An infinite plane wave is incident on the aperture in Plane 1, denoted by the spatial variable X. Consider how to calculate the complex amplitude at $P(x, z)$. Only the light that lies within the aperture opening can contribute to the complex amplitude at $P(x, z)$. We envisage the light within the aperture opening as consisting of an infinite number of secondary Point Sources (PS), each with an intensity and phase value, (only a few PS are shown here). Since the aperture is illuminated with an ideal plane wave, each secondary PS will have an identical intensity and phase value in Plane 1, nevertheless each PS will accumulate a different phase value a $P(x, z)$ due to the different path lengths, compare the distance l_1 and l_4, taken from Ref. [11].

Some relevant properties of the Fresnel transform are discussed in more detail here: [11]. We first examine the analytical solution of Eq. (1.1) for the following function:

$$U(X) = \exp\left(-\frac{X^2}{\alpha_i^2}\right)\cos\left(2\pi f_{\mathrm{x}} X\right), \tag{1.2}$$

which can also be expressed as

$$U(X) = \frac{1}{2}\exp\left(-\frac{X^2}{\alpha_i^2}\right)\left[\exp\left(j2\pi f_{\mathrm{x}} X\right) + \exp\left(-j2\pi f_{\mathrm{x}} X\right)\right]. \tag{1.3}$$

α_i is related to the spatial extent of $U(X)$. Although $U(X)$ spans an infinite extent, more than 99.9% of the signal's power lies within the following range: $-2\alpha_i \leq X \leq 2\alpha_i$ [9,11,17]. $U(X)$ also has an explicit spatial frequency component, f_x. Subbing Eq. (1.2) into Eq. (1.1) and integrating the gives the following result:

$$u_z(x) = \frac{1}{2}\left[u_z^+(x) + u_z^-(x)\right], \tag{1.4}$$

with

$$u_z^+(x) = K_z \exp\left[-\frac{\left(x - \lambda z f_{\mathrm{x}}\right)^2}{\alpha_z^2}\right]\exp\left[j\left(\phi_z^l x + \phi_z^q x^2\right)\right]. \tag{1.5}$$

$$\alpha_z = \left(\frac{\pi\alpha_i}{\sqrt{\pi^2\alpha_i^4 + z^2\lambda^2}}\right)^{-1}, \tag{1.6}$$

$$K_z = \left(\sqrt{1 + \frac{jz\lambda}{\pi\alpha_i^2}}\right)^{-1}\exp\left(\frac{-j\pi\alpha_i^4\pi^2 f_{\mathrm{x}}^2 z\lambda}{\pi^2\alpha_i^4 + z^2\lambda^2}\right), \tag{1.7}$$

$$\phi_z^l = \frac{2\pi^3 f_{\mathrm{x}}\alpha_i^4}{\pi^2\alpha_i^4 + z^2\lambda^2}, \tag{1.8}$$

and

$$\phi_z^q = \frac{\pi z^2\lambda^2}{\pi^2\lambda z\alpha_i^4 + z^3\lambda^3}. \tag{1.9}$$

We note that the input modulated Gaussian function under a Fresnel transform maps into another Gaussian function with a spatial extent of $4\alpha_z$. The location of the center of the Gaussian function, $u_z^+(x)$, lies at $x = \lambda z f_x$, ($u_z^-(x)$, lies at $x = -\lambda z f_x$). Thus we see that $U(X)$, will after a Fresnel transform, have a Spatial Extent, SE, in Plane 2 of

$$SE = 2(\lambda z f_x + 2\alpha_z). \tag{1.10}$$

This is our first important result. It indicates that a signal; that has effectively finite support and a given spatial frequency component, f_x, will increase in extent, as it propagates, due to two separate factors: f_x, and α_z. This analytical form has been chosen because of the relative simplicity of the result, which allows one to imagine how the power, associated with specific spatial frequencies, 'walks-off' the optical axis under propagation, remaining localized within Gaussian envelope, see Ref. [17]. The higher f_x is, the more it 'walks-off' the optical axis under propagation. In following sections we will use both Eq. (1.3) and Eq. (1.10) to predict SE for general input fields. For example all optical fields that we wish to calculate numerically will have a finite extent which must be related to α_i and an effective maximum spatial frequency f_x - once these parameters can be estimated then we shall see that Eq. (1.10) gives a reliable estimate for the actual spatial extent of the field in the diffraction plane.

In the previous example the input function $U(X)$ had an explicit mathematical form. It is possible however, in certain circumstances, to make predictions about the form of the diffracted field when only the statistical properties of the input field are known. We now consider the diffraction pattern we might expect to see when the object in the input plane is an optically rough diffuser. A diffuser is a piece of glass like shower glass that has an uneven surface profile. Since the optical wavelength is so small, for example 500 nm, then even small differences in the thickness of the glass will cause phase changes in the incident plane wave that are much larger than 2π. This is the meaning of 'optically rough'. We will examine how an object modifies an incident wavefield in much more detail in Chapter 2. For now however we provisionally accept the idea that the phase profile, $\arg\{u_z(x)\}$ of the field immediately after the diffuser is randomly distributed between 0 and 2π.

We now reconsider the conceptual idea behind the Fresnel transform: The complex field at a particular spatial location in the diffraction plane arises from a sum (integration) of contributions from an infinite number of secondary point sources in the input plane; see Fig. 1.1 and its caption in particular. Furthermore after the diffuser each of these contributing secondary point sources has a random phase associated with it (more

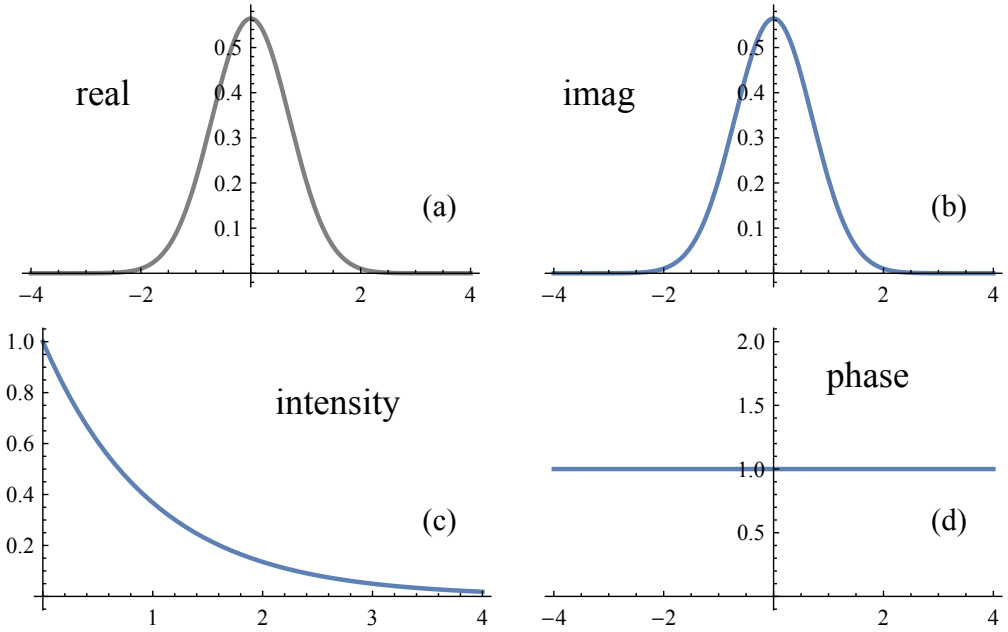

Figure 1.2 – Illustration of the probability distribution functions for (a) the real part of the optical field (normal distribution), (b) the imaginary part of the optical field, (c) the intensity of the optical and (d) the expected phase value of the field.

generally each point source can have a random complex amplitude associated with it). Hence we see that to calculate the complex amplitude consisting of the real and imaginary part of the optical field, we must sum together a large number of random numbers that vary between known limits. Provided that the number of contributing point sources is very large then this problem reduces to a well known statistical problem called the random or drunken walk. Applying this statistical concept it can be shown that both the real and imaginary parts of the optical field follow Gaussian statistics or follow a 'normal' statistical distribution. We can also derive the statistical distribution that describes the expected value of the intensity and the phase of the optical field. The intensity follows what is known as a negative exponential distribution, while the phase follows a uniform distribution where each possible value is equally likely. We summarize the result of these considerations in Fig. 1.2. In Fig. 1.3, we present a typical experimental result - this type of intensity pattern is known as a speckle patten. It is possible to examine the statistical distribution of the intensity values for such a

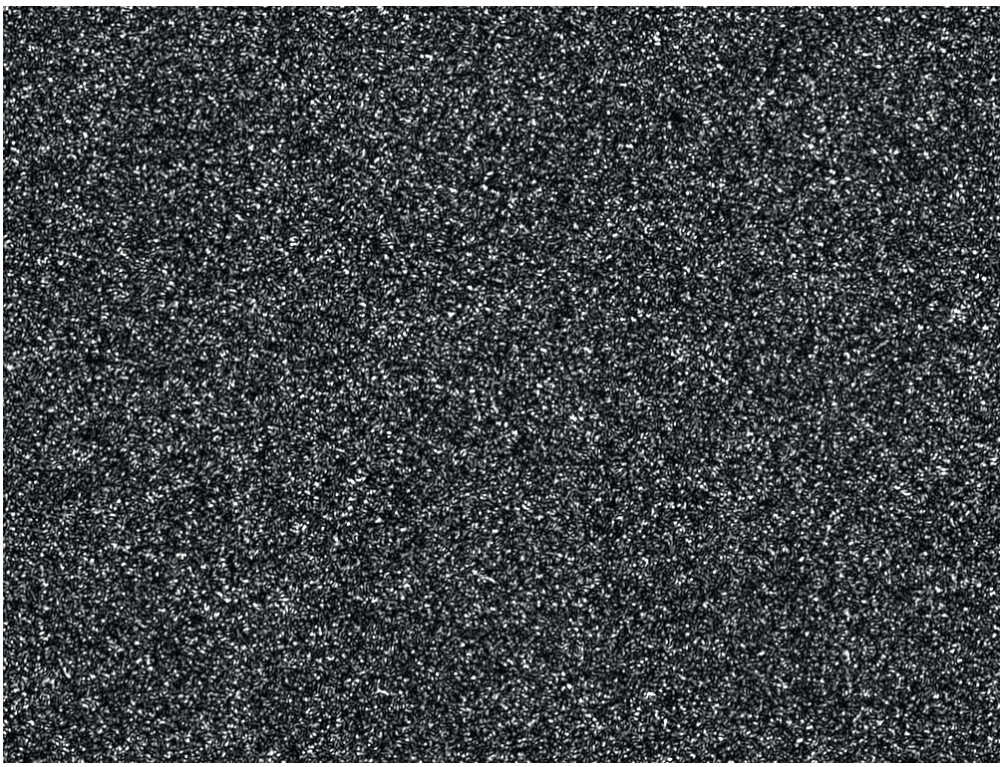

Figure 1.3 – An experimental result illustrating a typical speckle pattern.

speckle pattern which we present in Fig. 1.4 - it is clear that the distribution closely follows that predicted from these theoretical considerations.

1.3 Diffraction calculations

We have just examined the principles behind performing the Fresnel transform and have examined a specific analytical example and a second statistical problem. Analytical examples however are far from common and hence we now turn our attention to the calculation of the Fresnel transform numerically. We will examine two different algorithms that can be used to calculate the Fresnel transform numerically. These algorithms are the 'Direct Calculation' (DC) and the 'Spectral Calculation' (SC). It is important to realize that these approaches are different from the fast numerical calculation techniques commonly referred to as the Direct and Spectral Method and which are examined here [11]. The 'Direct Calculation' and the 'Spectral Calculation' do not make use of the FFT algorithm and importantly we have control over the output spatial coordinate, x, which can be chosen freely. To begin we first clearly state the input to our numerical algorithm, which takes the form of two vectors; a spatial vector and a vector of complex values representing our signal. Once these vectors are defined we can then compare the

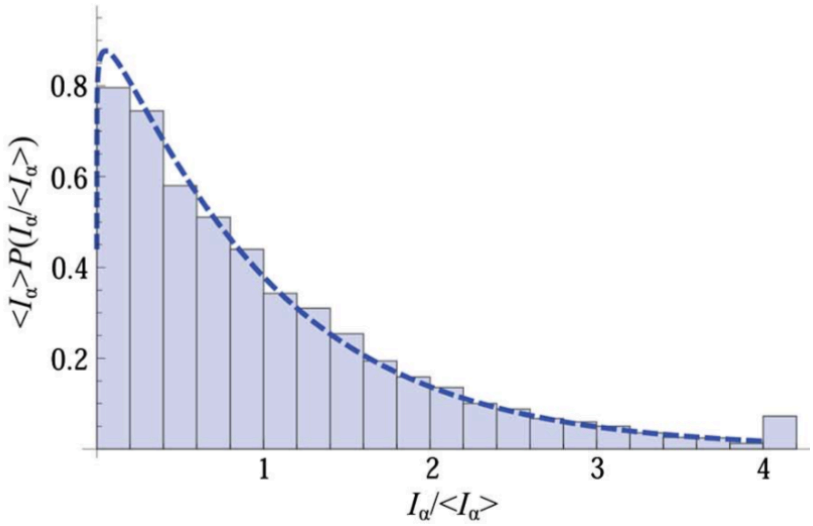

Figure 1.4 – An experimental result taken from [24], showing a histogram of the intensity values from a speckle field which has been detected with a CCD array where the speckle size is greater than the pixel size of the CCD array, see [24] for more detail.

properties of each algorithm.

To begin our numerical analysis, we assume that we have a vector of complex values, $\mathbf{U}$, that correspond to the actual values of the function, $U(X)$ at uniformly spaced sampling points, (separated from each other by δX), defined with the spatial vector, X, i.e.

$$\begin{aligned} \mathbf{U} &= [U(X_1), U(X_2), ...U(X_N)]\,, \\ &= [U_1, U_2, ...U_N] \end{aligned} \tag{1.11}$$

where

$$\mathbf{X} = [X_1, X_2, ...X_N] \tag{1.12}$$

and where N is the total number of samples. In the rest of the manuscript we use bold faced letters to indicate a vector. These two vectors, with a given λ and z, define the input parameters for the numerical calculation.

The Direct Calculation

Since we are now using only a finite number of samples to define the input field in Plane 1, the diffraction integral in Eq. (1.1) reduces to a finite summation,

$$\begin{aligned} u_z^S(x) &= \frac{\delta X}{\sqrt{j\lambda z}} \sum_{n=1}^{N} U_n \exp\left[\frac{j\pi}{\lambda z}(x - X_n)^2\right], \\ &= \frac{\delta X}{\sqrt{j\lambda z}} \exp\left(\frac{j\pi x^2}{\lambda z}\right) \\ &\times \left\{\sum_{n=1}^{N} U_n \exp\left(\frac{j\pi X_n^2}{\lambda z}\right) \exp\left(\frac{-j2\pi x X_n}{\lambda z}\right)\right\}, \end{aligned} \tag{1.13}$$

where n is an integer. We note that $u_z^S(x)$ is a continuous function of x that has been calculated from a finite set of data points and we indicate this with the superscript 'S'. Hence the DC, Eq. (1.13), can be considered as the following:

- Multiplication by a chirp,
- A scaled Fourier transform,
- Multiplication by a second another chirp.

To better understand the consequences of representing the input field using a finite set of uniformly spaced samples it is instructive to perform the numerical calculation of $u_z^S(x)$ for a specific example,

$$U(X) = p_L(X)\cos(2\pi\Gamma X), \tag{1.14}$$

where

$$p_L(x) = \begin{cases} 1, & \text{when } |x| < L \\ 0, & \text{otherwise.} \end{cases} \tag{1.15}$$

We sample $U(X)$, taking $N = 100$, over the range $-L \leq X \leq L$, where $L = 0.1$ mm, giving a δX of 2 μm. The other parameters were chosen to be: $z = 1$ cm, $\lambda = 505.7$ nm, and $\Gamma = 30$ lines/mm. In Fig. 1.5 and Fig. 1.6, we present the result of this calculation over the ranges: $-SE/2 \leq X \leq \lambda z/\delta X$, and $0 \leq X \leq \delta X$ mm respectively. In Fig. 1.5 we present the magnitude distribution while the phase distribution is plotted in Fig. 1.6.

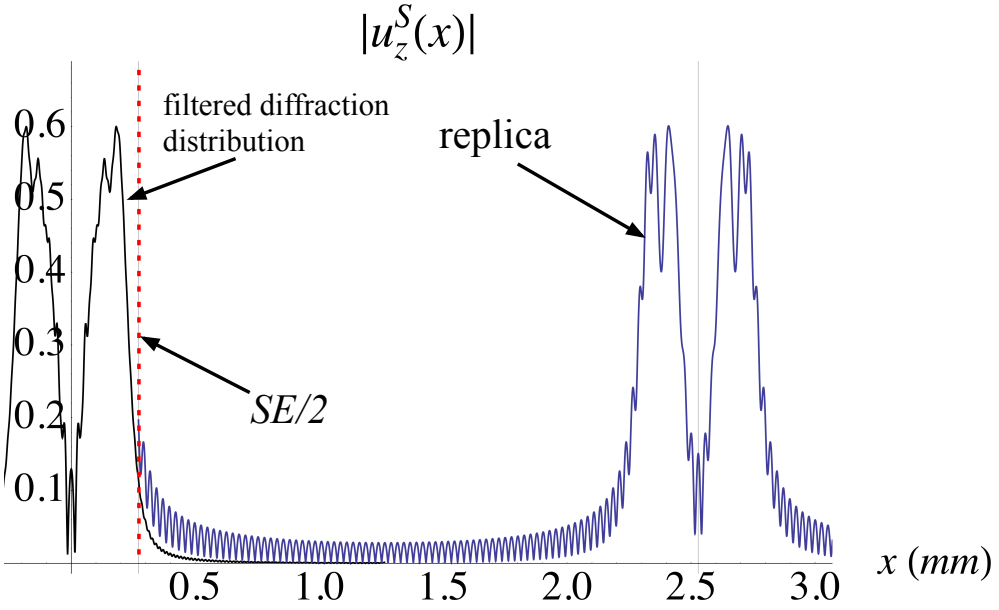

Figure 1.5 – Result of diffraction calculation. The presence of a replica is clearly visible located at $x = 2.5$ mm, also the red dotted line indicates the location of $SE/2$, illustrating the extent of the diffracted field. The distribution plotted in black has been spatially filtered and contains no spatial frequencies higher than 35 lines/mm. Note the finite extent of the signal in comparison to the blue plot. (For presentation purposes the central order replica in blue is not plotted over the range $-SE/2 \leq x \leq SE/2$), taken from [11]

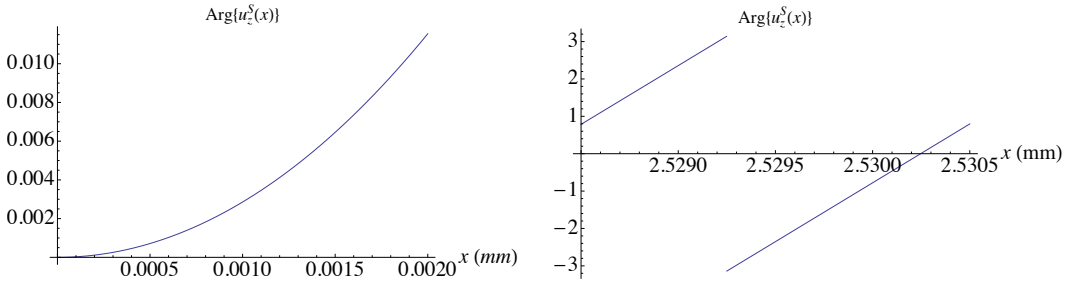

Figure 1.6 – Result of diffraction calculation, for the phase distributions. Both plots are over a range of δX. The plot on the left is the phase of the zero order replica (off-set to zero). The plot on the right is for the first replica; there is a constant phase off-set of $\pi/4$, and a linear phase with slope $1/\delta X$, taken from [11].

Now we refer back to our discussion of that important parameter, SE. We would like to extend the usefulness of the analytical result given by Eq. (1.10) to this numerical example. For this figure we initially choose a value for the maximum effective spatial frequency by setting $f_x = \Gamma$ lines/mm, however as we shall see, Eq. (1.14), contains power in spatial frequencies higher than Γ due to the rectangular function that limits the finite spatial extent of the signal. We shall later demonstrate that the best way to determine an appropriate value for the maximum effective spatial frequency extent is to consider the distribution of the signals power in its Fourier domain.

Now to calculate the value of α_z, we must to relate α_i to the finite extent of the rectangular function, defined in Eq. (1.15), i.e. we set $4\alpha_i = 2L$. The result is plotted in Fig. 1.5. From Fig. 1.5, we can also see that there is a replica present, centered at the location $x = \lambda z/\delta X = 2.5$ mm. Comparing the phase of the central and first order replicas, we find that the first order phase distributions has an additional linear phase and constant phase. We note there are an infinite number of replicas in Plane 2 as a result of this calculation, which can be verified by simply plotting $u_z^S(X)$ over a wider range of x. The following relationship holds [11, 17]. We recongize that these replicas arise due to the sampling of the input field.

$$\begin{aligned} u_z^S(x) &= \sum_{m=-\infty}^{\infty} u_z\left(x - \frac{m\lambda z}{\delta X}\right) \\ &\times \exp\left(\frac{j\pi\lambda z m^2}{\delta X^2}\right)\exp\left(\frac{j2\pi m x}{\delta X}\right). \end{aligned} \tag{1.16}$$

From these considerations we find that the following sampling guideline is appropriate:

$$SE < \lambda z/\delta X, \tag{1.17}$$

in order to ensure that neighboring replicas do not overlap introducing error into the numerically calculated diffraction distribution.

When the DC is used to calculate the Fresnel integral all spatial frequencies propagate and contribute to the complex distribution in Plane 2, even those spatial frequencies that are sampled below the so-called Nyquist sampling rate. The presence of spatial frequencies at spatial locations greater than $SE/2$ is evident from Fig. 1.5, where an oscillating signal extends outwards from $x \geq SE/2$ (distribution plotted in blue). This oscillation is due to spatial frequencies in the input signal that are

higher than Γ. A poor choice of $f_x = \Gamma$ leads to a value for $SE/2$, (as presented in Fig. 1.5), that does not reflect the proper output extent of the diffracted signal. A proper choice for f_x should be made on the basis of how the input signal's power is distributed in its Fourier domain. Shortly we examine in more detail how to choose an appropriate value for f_x based on concepts from the space-bandwidth product of a signal.

It is possible however to limit the spatial frequency extent of $u_z^S(x)$ by subjecting it to a filtering operation in the Fourier domain and hence controlling SE in accordance with Eq. (1.10). Here we spatially filter all frequencies higher than $f_x^{\max} = 35$ lines/mm. In practice we can perform this filtering operation with the following steps:

- The continuous field $u_z^S(x)$ is sampled at a very high rate,
- These samples are Fourier transformed using an FFT operation,
- The resulting spatial frequency distribution is multiplied by a rectangular aperture to remove spatial frequencies above $f_x^{\max}$,
- This filtered spatial frequency distribution is then subject to an inverse FFT operation

In Fig. 1.5 the results of such a filtering operation can be seen by examining the black plot. This distribution has a much clearer finite spatial extent and is more in agreement with the value for SE, Eq. (1.10), calculated for a value of $f_x = \Gamma = 30$ lines/mm. The distribution (plotted in black) now has a spatial extent agreeing with the results presented in Section 2, however the distribution is not as accurate when compared to the correct analytical solution. The filtering operation has removed some of the structural details evident in the replica distribution (blue) located at $x = 2.5$ mm.

Nevertheless, if the spatially filtered result (distribution plotted in black) presented in Fig. 1.5, is considered satisfactory for a given application, we note that an almost identical result can be achieved by reducing the number of samples by a factor of 3.5, ≈ 28 samples. Reducing the number of samples for a given input extent, reduces the separation between the replicas; the spatial frequency filtering operation controls SE.

We suggest the relation, Eq. (1.17), as sampling guideline, to be used when the spatial and spatial frequency extent of the input signal are known. When we use this sampling guideline for the specific example discussed, Eq. (1.14), we find that for a range of different values for z and Γ, an absolute minimum of about 98% of the signal's power lies within $-SE/2 < x < SE/2$, when $f_x = 60$ lines/mm. Although the SE

criterion has been specifically examined for Eq. (1.14), in fact this relationship holds for a range of different signal types, including random signals of finite spatial frequency extent.

An important point relating to the first sampling rule is that as z becomes smaller, the replicas move closer together. This effect can be compensated for by increasing N (while maintaining the same input extent of $2L$) and thereby reducing δX, however after a certain point this calculation becomes extremely numerically intensive and hence unfeasible for practical calculations.

In closing this section we calculate the total power associated with the input signal, P_i with the following expression

$$P_i = \int_{-\infty}^{\infty} \|U(X)\|^2 \, dX, \tag{1.18}$$

which for the numerical example presented here amounts to a value $P_i = 0.0001$ arbitrary units at Plane 1.

The Spectral Calculation

This approach makes use of the Fourier transform in order to perform the Fresnel transform. It is appropriate here to define the forward and inverse Fourier transform for some complex signal $f(x)$:

$$\begin{aligned} \tilde{f}(v) &= \mathrm{FT}\left\{f(x)\right\}(v) \\ &= \int_{-\infty}^{\infty} f(x) \exp\left(-j2\pi xv\right) dx, \end{aligned} \tag{1.19}$$

and

$$\begin{aligned} f(x) &= \mathrm{IFT}\left\{\tilde{f}(v)\right\}(v) \\ &= \int_{-\infty}^{\infty} f(x) \exp\left(j2\pi xv\right) dv, \end{aligned} \tag{1.20}$$

where v is the spatial frequency coordinate and the functions $f(x)$ and $\tilde{f}(v)$ are Fourier transform pairs (indicated by the tilde).

We now write Eq. (1.1) is a different by mathematically equivalent form

$$u_z(x) \quad = \quad \mathrm{IFT}\{\exp\left(-j\pi\lambda z v^2\right) FT\{U(X)\}(v)\}(x)\,. \tag{1.21}$$

There are several different steps that occur when Eq. (1.21) is implemented numerically. We now introduce a discrete form of the Fourier transform where again the superscript 'S' indicates that this continuous function is generated from a finite set of complex data points, in our case from the vector **U**.

$$\tilde{U}^S(v) \quad = \quad \delta X \sum_{n=1}^{N} U_n \exp\left(-j2\pi v X_n\right), \tag{1.22}$$

where n is an integer.

We note that the distribution described by Eq. (1.22) also contains an infinite number of replicas whose centers are separated from each other in the Fourier domain by a distance $\Delta B = 1/\delta X$. We shall refer to these replicas as 'Fourier replicas' so as to distinguish them from the replicas that arose during the DC calculation.

The inverse Fourier transform operation

Replacing the function, $FT\{U(X)\}(v)$, in Eq. (1.21), with Eq. (1.22) we get

$$u_z^S(x) \quad = \quad \int_{-\infty}^{\infty} \exp\left(-j\pi\lambda z v^2\right) \tilde{U}^S(v) \exp\left(j2\pi x v\right) dv, \tag{1.23}$$

where we have explicitly included the inverse Fourier transform integral in Eq. (1.23) to emphasize that the integration takes place over the entire Fourier plane and therefore will include a contribution from every 'Fourier replica' that lies along this plane. The distribution along entire Fourier plane is multiplied by a 'lens' or 'chirp function' of infinite extent and of effective focal length, $f = 1/-(\lambda^2 z)$, see also Ref. [9].

In practice however the integration limits of the inverse Fourier transform, Eq. (1.23), are limited to a finite extent of the Fourier domain and to a finite number of samples. We note that usually when the fast Fourier transform is used to implement the SC calculation the finite extent taken when calculating this integral is ΔB, and is uniformly sampled with N samples. It is precisely this limiting of the Fourier extent and the secondary sampling procedure that takes place here that causes the fast Fourier transform

based DC and SC calculations to have fundamentally different properties with regard to the output extent. We refer the reader to the following reference where the contributions of Fourier replica's to the output of the Fresnel transform are specifically examined [9].

Choosing the Fourier extent - power considerations

Again we note that $\tilde{U}^S(v)$ is actually a continuous function. Hence we have the freedom to choose any sampling interval, δv, and we may also in principle choose any Fourier domain extent. Parseval's theorem states that a Fourier transform conserves power and therefore we should expect the total power in the Fourier domain is equal to P_i. It is a feature of the sampling operation this power P_i, is contained within each 'replica window', i.e. within the range $-\Delta B/2 \leq v \leq \Delta B/2$. It is the fact that in the numerically calculated Fourier transform this total power P_i now lies within a Fourier replica window instead of being spread over the infinite extent of the Fourier plane that is responsible for the errors that sampling introduces.

A signal can have a finite extent in only one domain, see Ref. [11]. Since $U(X)$ is bounded the power of its Fourier transform pair $\tilde{U}(v)$ must be distributed over the entire Fourier domain. This means that when a signal of finite extent is sampled, it creates 'Fourier replicas' of infinite extent. Since each replicas itself has an infinite extent, power from neighboring replicas must leak into each other. And they will do so in such a manner that the total power in each 'replica window' is P_i. It is this 'leaking' of power that causes the aliasing effect but it can be made arbitrarily small by increasing ΔB. And we can increase ΔB by increasing the number of samples N for a given input extent. If we define the spatial extent and a spatial frequency extent of signal in this manner we arrive at the idea of a space-bandwith product. This concept has been discussed here [11], and a region in the Fourier domain can be defined such that $P_v/P_i > R$, where

$$P_v = \int_{-FR/2}^{FR/2} \left\| \tilde{U}(v) \right\|^2 dv, \tag{1.24}$$

and where R can be chosen so as to approach unity. As FR, in Eq. (1.24), increases and R approaches 1, the distributions $\tilde{U}^S(v)$ and $\tilde{U}(v)$ become more increasingly alike over the range $-\Delta B/2 \leq v \leq \Delta B/2$, indicating a reduction in errors introduced by aliasing. From these considerations we can define a region in the Fourier domain that contains 100 $R = 90$ % of the signal's power.

Spectral calculation - sampling guideline

We have just considered how to define an extent in the Fourier domain based on power considerations. We now would like to define a vector of complex values in the Fourier plane that describe our signal. Keeping $N = 100$, we can define a spatial frequency step size $\delta v = FR/N$ and then a spatial frequency vector as

$$\mathbf{v} = [-FR/2, -FR/2 + \delta v + ... + FR/2 - \delta v], \tag{1.25}$$

and using this vector we sample the continuous field

$$\begin{aligned} \tilde{\mathbf{U}}^{\mathbf{S}} &= \left[\tilde{U}^S(v_1), \tilde{U}^S(v_2), ...\tilde{U}^S(v_N)\right], \\ &= \left[\tilde{U}_1^S, \tilde{U}_2^S, ...\tilde{U}_N^S\right]. \end{aligned} \tag{1.26}$$

We now substitute these vectors into Eq. (1.23) and again replace the integral with a finite summation to arrive at

$$u_z^{S^{SC}}(x) = \delta v \left\{ \sum_{n=1}^{N} \tilde{U}_n^S \exp\left(-j\pi\lambda z v_n^2\right) \exp\left(+j2\pi x v_n\right) \right\}, \tag{1.27}$$

where $u_z^{S^{SC}}(x)$ is a continuous function which has been calculated from a finite set of data points, $\tilde{\mathbf{U}}^{\mathbf{S}}$. This new function is the result of the numerical implementation of the SC. It is fundamentally a different result from $u_z^S(x)$, which is reflected in the superscript: 'S^{SC}'. Similar to $u^S(x)$, an infinite set of replicas is also generated in the output plane (Plane 2) however there are two important differences:

- The spacing between the replicas in Eq. (1.27) is $1/\delta v$,
- These higher order replicas do not have any linear or constant phase terms associated with them, $u_z^S(x)$.

We now outline the sampling rule that governs the SC

$$SE < 1/\delta v. \tag{1.28}$$

This result indicates that there are fundamental differences between the replicas that arise in the direct and spectral calculations. The most important is that there is a different spacing between them given by: $(\lambda z/\delta X)$, and $(1/\delta v)$, for the DC and SC, cases respectively.

1.4 The propagation of light pulses

Ultrashort and few-cycle pulses are important in modern optics, particularly as new femto-second sources become more reliable and affordable. Such pulses are used in areas such like optical coherence tomography (the spatial coherence of the source can be controlled with a pinhole), confocal microscopy, terahertz (THz) generation and detection, and spectroscopy [6]. Pulses generated in femto-second sources have a broad spectrum which consists of many different wavelengths. This is fundamentally different to the approximately monochromatic light produced by most standard lasers and that we have until now been considering. In general, there is a complicated relationship between different spectral components, that is related to the temporal coherence properties of the light sources.

Calculating the diffraction pattern for these pulses we must consider the contribution from each spectral component. Introducing the different spectral frequencies components actually will re-introduce a time component to our new diffraction problem. To understand how these diffracted pulses behave in space and time we have to first consider the spatial diffraction pattern formed by an individual spectral component. In fact this is the diffraction problem that we have been considering in this chapter so far. Thus the propagation of each spectral component is described using the Fresnel transform. This diffraction calculation is repeated for each spectral component to yield what we term a spatial-spectral distribution. And finally the diffracted spatial-temporal pulse is found by performing an inverse Fourier transform with respect to the temporal frequency on this spatial-spectral distribution [6]. And as we note while sometimes analytical solutions for pulse diffractions exist, in order to analyze general diffraction problems, a complementary numerical techniques must also be developed [6].

We continue with a 1-D analysis (x) and we further assume that the pulse filling the aperture has a spatially invariant spectrum at that plane (z = 0) - corresponding to a Type I pulse [6]. Now under these conditions we proceed to define the sampling rules that allow accurate implementation of our numerical technique for calculating diffraction of pulses. We begin by writing an expression for an individual spectral component:

$$\tilde{u}_K(x, K) = u_K(x, K) \exp\left(\frac{jz\omega}{c}\right), \tag{1.29}$$

where

$$u_K(x,K) = \sqrt{\frac{1}{jK}} \int_{-\infty}^{\infty} U(X) \exp\left[\frac{j\pi}{K}(x-X)^2\right] dX, \tag{1.30}$$

and where we recognize that Eq. (1.29) is in fact a Fresnel transform that we write in slightly different notational form that is more convenient for our analysis. We also note that c is the speed of light and that $K = \lambda z = 2\pi z c/\omega$, and naturally where λ refers to the wavelength of the particular spectral component, and z is the propagation distance, ω is the temporal frequency of the light. We now define that the pulse has a temporal frequency distribution given by $V(\omega)$ and thus write the spatial-spectral distribution as

$$u(x,K) = \tilde{u}_K(x,K)\, V(\omega). \tag{1.31}$$

We can then write the final distribution of the pulse with the following expression:

$$u_z(x,z,t_R) = \int_0^{\infty} \tilde{u}_K(x,K)\, V(\omega) \exp(-j\omega t_R)\, d\omega, \tag{1.32}$$

where we have introduced the retarded time, t_R.

$$t_R = t - \frac{z}{c}. \tag{1.33}$$

Eq. (1.29) to Eq. (1.33) are the equations that describe the diffraction of a pulse. By introducing the retarded time we cancel the effect of the linear phase term on the right hand side of Eq. (1.29). We now specifically examine an analytical solution to this problem, with the hope that this solution will provide some insight into the pulse diffraction calculation. We imagine that the $U(X) = p_L(X)$ where

$$\begin{aligned} p_L(X) &= 1, \text{if } |X| < L \\ &= 0, \text{ otherwise,} \end{aligned} \tag{1.34}$$

where $2L$ is the diameter of the aperture opening. With this expression for $U(X)$ we find that a single spatial-spectral component is now given by

$$u_K(x,K) = -\frac{1}{2}\left\{\text{erf}\left(\sqrt{\frac{\pi}{K}}(-1)^{\frac{3}{4}}\right)(L-x) + \text{erf}\left(\sqrt{\frac{\pi}{K}}(-1)^{\frac{3}{4}}\right)(L+x)\right\} \tag{1.35}$$

We wish to calculate Eq. (1.32) with a finite number of contributing spectral components N_ω therefore we re-write the continuous integral form as a finite summation to arrive at

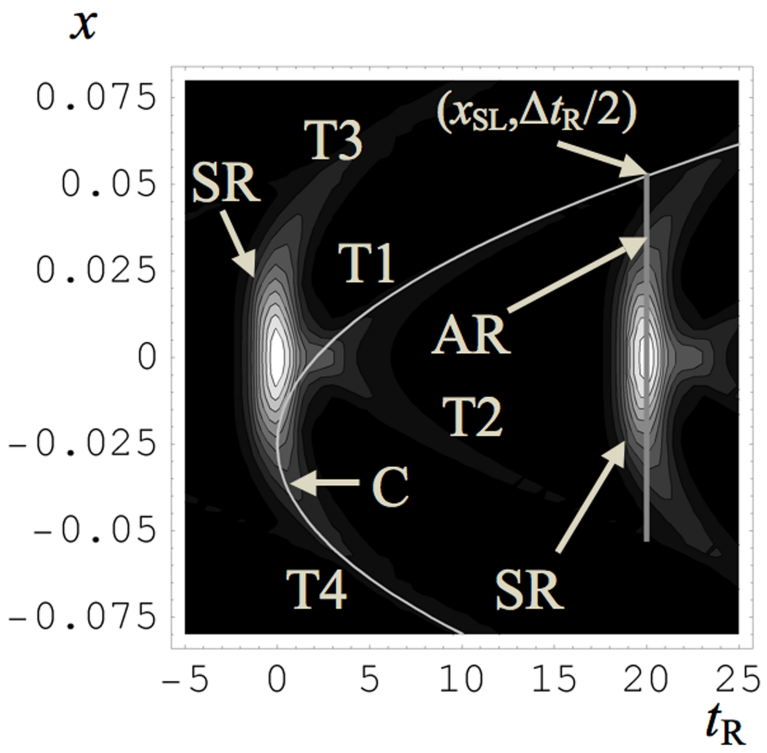

Figure 1.7 – Contour plot of $|u_z^S(x, z = 1, t_R)|$ for $-0.075 \leq x \leq 0.075$ m and $-5 \leq t_R/T \leq 25$. There are ten contour levels spanning the range $0 \leq |u_z^S(x, z = 1, t_R)| \leq 3.56 \times 10^6$. T1, T2, T3, T4, pulse tails 1 to 4; AR, aliasing free region delimited by (x_{SL}, t_R); SR, sampled replica; C, curve plotted using Eq. (1.44).

the following expression:

$$u_z^S(x, z, t_R) = \delta_\omega \sum_{n=1}^{N_\omega} u_K(x, K) V(\omega) \exp\left(-j\omega t_R\right), \tag{1.36}$$

where again the subscript S distinguishes between the ideal analytical signal $u(x, z, t_R)$ and its sampled counterpart which is calculated using the vectors $K_n = [K_1, K_2, ...K_{N_\omega}]$ and $\omega_n = [\omega_1, \omega_2, ...\omega_{N_\omega}]$ and where δ_ω is the temporal frequency spacing between each contributing spectral component. There are significant differences between these two representations, i.e. between Eq. (1.32) and Eq. (1.36). For example we expect from sampling theory that the discretization of the spectral components will produce an infinite number of replicas - now however in the time domain which have the following properties:

- Copies of the pulse distribution are are repeated periodically in time,
- The separation between time-replicas is related to N_ω and δ_ω

If we wish to recover our signal we need to ensure that N_ω is sufficiently high so that successive replicas do not overlap with each other. However, it is not sufficient to consider the ω and t_R variables, the spatial variable x also plays a role. Before we consider how changing the spatial variable x effects the sampling considerations, we first examine the form of the pulse spectrum, $V(\omega)$, of the optical pulse that fills the aperture in the plane. We also consider again an important concept introduced earlier in this chapter and to which we shall again turn. This time however we discuss the concept of time-frequency (temporal) product instead of a space-bandwidth product. to begin we consider some temporal signal, defined as $g(t)$. If the energy of the signal $g(t)$ is localised within some finite region in both the time and temporal-frequency domains, i.e.

$$\int_{-\Delta\omega/2+\omega_0}^{\Delta\omega/2+\omega_0} |\tilde{g}(\omega)|^2 = \int_{-\Delta t/2}^{\Delta t/2} |\tilde{g}(t)|^2 = \nu E_\omega \tag{1.37}$$

where E_ω is the energy contained over the entire temporal spectrum, and where ν is a fraction that can be chosen to be arbitrarily close to 1. In Eq. (1.37), it is assumed that the signal $g(t)$ and $\tilde{g}(\omega)$ are centered at the coordinates, $t = 0$ and $\omega = \omega_0$, respectively. Using uniform sampling steps of δ_ω, the number of samples required to represent $g(t)$ can be determined by the time-frequency product:

$$N_\omega = \frac{\Delta t \Delta\omega}{4\pi}. \tag{1.38}$$

In order to proceed further we must assume a particular form for $V(\omega)$ which for simplicity we set to be a Gaussian pulse of the form,

$$V(\omega) = \sqrt{T} \exp\left\{ - \left[\frac{T\left(\omega - \omega_0\right)}{\sqrt{2}} \right]^2 \right\} \tag{1.39}$$

and that has a corresponding Fourier transform (with respect to the temporal frequency),

$$v(t) = \frac{1}{\sqrt{T}} \exp\left(-j\omega_0 t\right) \exp\left[- \left(\frac{t}{\sqrt{2}T} \right)^2 \right], \tag{1.40}$$

We note that the parameter T is related to the width of the Gaussian pulse in both the time and temporal frequency domains. In the time domain, the full width half maximum is given by $2\sqrt{2\ln(2)}T$ and ω_0 is the central frequency of the pulse. It can be shown that 99% of the energy in the Gaussian pulse is contained between $-4T \leq t \leq < 4T$ in the time domain, and between $-4/T + \omega_0 \leq \omega \leq 4/T + \omega_0$ in the frequency domain. Applying these energy considerations we define our temporal frequency extent as $\Delta\omega = 8/T$. So

as to ensure that successive replicas do not overlap we propose that N_ω be chosen such that the time extent of the signal, $\Delta t = 1/\delta_\omega = 40T$. This choice is somewhat arbitrary, however from performing many numerical simulations we have found that it is suitable for most of the calculations we have wished to perform. Then with the assumption of uniform sampling, N_ω can be estimated from the time-frequency product to give, $N_\omega = 40/T$ and $\Delta t = 4\pi N_\omega/\Delta\omega$. We now wish to examine the pulse distribution in the diffraction plane. So, substituting Eq. (1.38) into Eq. (1.36) and following the sampling guidelines for $V(\omega)$, we calculate $|u_z^S(x, z, t_R)|$ and plot the result in Fig. 1.7. The simulation values are as follows: $T = 0.5 \times 10^{-12}$ s, and $z = 1$ m, $\omega_0 = 1.6 \times 10^12$ rad s^{-1}, $L = 25$mm. In these numerical results we can see the presence of two replicas; the first at $t_R = 0$ and the second at $t_R = \Delta t/2 = 20T$. The pulse's energy spreads out into four individual tails (see Fig. 1.7) which trail behind each pulse replica. These residual tails overlap with the other sampled replicas, see Fig. 1.7, which causes aliasing in the calculated distribution. The resulting numerical error that arises is a form of temporal-spatial aliasing unlike the spatial aliasing we have previously seen. If we were to reduce N_ω then the replicas would move closer together and the tails that spread out from the pulse center would overlap with the replicas sooner. Although we have only presented one specific case, we have performed these numerical calculations for a variety of different values of z and ω and believe this is a representative example, (see figure caption for details about the range of the contour plot). It now remains to find a relationship between x and t_R that allows us to predict where the trailing tails of one replica intercept the following replica. The trails appear to emanate from locations at the aperture edges. Here in Ref. [6] it has been shown that this relationship is given with the following two expressions:

$$x = \pm\sqrt{2zct_R} + L, \tag{1.41}$$

and

$$x = \pm\sqrt{2zct_R} - L. \tag{1.42}$$

With Eq. (1.41) and Eq. (1.42), we now have an analytical expression describing the path taken by the tails, which trail each pulse replica. Aliasing will occur when the tails from one replica overlap with a subsequent replica. The spacing in time between these successive replicas is determined by time-frequency product considerations we discussed earlier. For example when $t_R = \Delta t/2$ marks the arrival of the second replica's peak pulse amplitude. In order to discuss aliasing in the pulse distribution about this peak amplitude point, we introduce the variable t_v setting $t_R = (\Delta t/2 + t_v)$ in Eq. Eq. (1.41)

and Eq. (1.42). Then we can identify a region in space and time [delimited by the point $x_{SL}(t_v)$], where the pulse can be calculated without the effects of aliasing. This region is given by

$$x_{SL1}(t_v) = \pm\sqrt{2zc\left(\frac{2\pi N_\omega}{\Delta\omega}\right)} + L, \tag{1.43}$$

and

$$x_{SL2}(t_v) = \pm\sqrt{2zc\left(\frac{2\pi N_\omega}{\Delta\omega}\right)} - L. \tag{1.44}$$

We note the following results from Eq. (1.42) and Eq. (1.42): (i) x_{SL} varies as a function of t_v, and (ii) the aliasing free region delimited by x_{SL}, may be made larger by increasing N_ω, however this increase occurs at a rate of $\sqrt{N_\omega}$. Eq. (1.42) has been overlayed on Fig. 1.7.

We now present some numerical results for some 2-D diffraction patterns formed when a pulse is incident upon either a square or a circular aperture. Furthermore we are going to examine the diffraction process numerically for a spectral profile that is no longer Gaussian in shape to demonstrate that the results just derived also apply for a wider class of time-frequency pulse envelopes. We now assume that our spectral distribution is given by

$$\begin{aligned} V(\omega) &= \tfrac{s+1}{\omega_b}^{s+1} \tfrac{(\omega-\omega_a)^s}{\Gamma(s+1)} \exp\left[-(s+1)\tfrac{\omega-\omega_a}{\omega_b}\right], \text{for } \omega > \omega_a \\ &= 0, \text{ otherwise,} \end{aligned} \tag{1.45}$$

In the subsequent simulations we have set, $s = 1$, $\omega_b = 6 \times 10^{12}$, $\omega_a = 100 \times 10^{12}$, we choose $z = 0.1$ m, $L = 0.1$ mm for the square aperture of total side $2L$ and for the circular aperture we assume a radius also given by $L = 0.1$ mm.

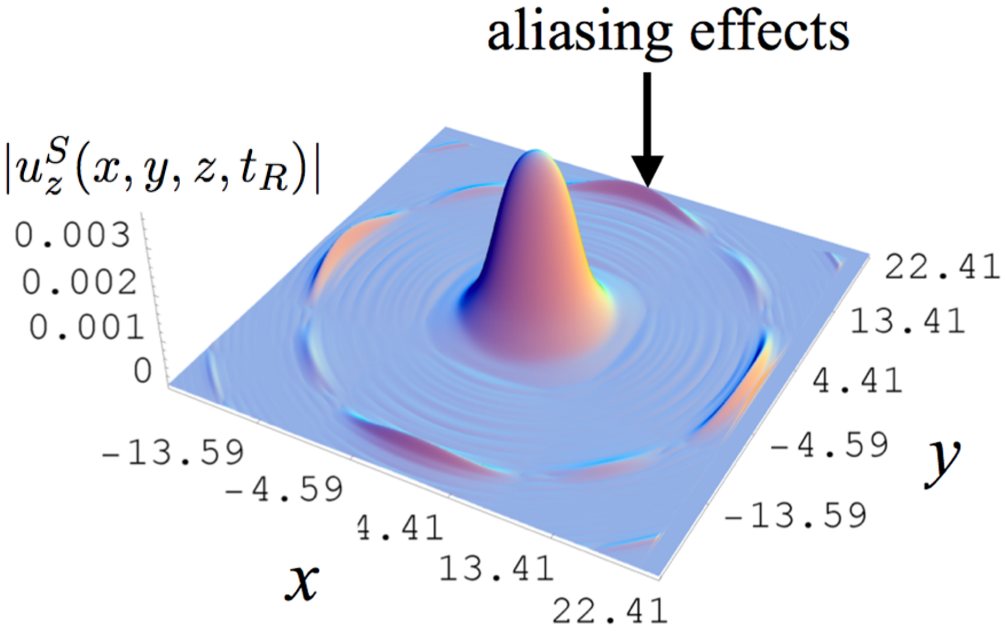

Figure 1.8 – Numerical results of $|u_z^S(x,y,z,t_R)|$ for a square aperture, with $t_v = 0$ s, $z = 0.1$m, $L = 0.1$ mm over the range $-23 \leq x \leq 23$ mm, $-23 \leq y \leq 23$, figure taken from [6].

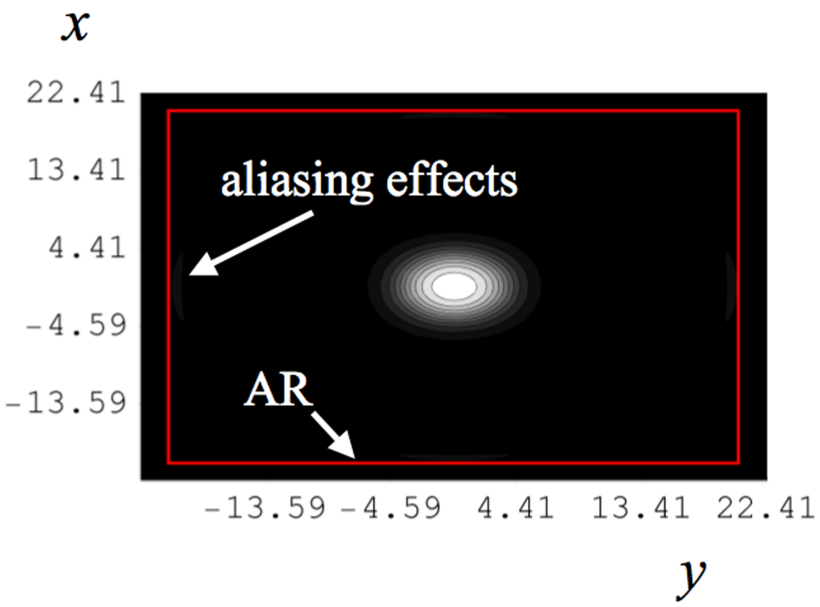

Figure 1.9 – Contour plot of numerical results of $|u_z^S(x, y, z, t_R)|$ for a square aperture, with $t_v = 0$ s, $z = 0.1$m, $L = 0.1$ mm over the range $-23 \leq x \leq 23$ mm, $-23 \leq y \leq 23$, figure taken from [6].

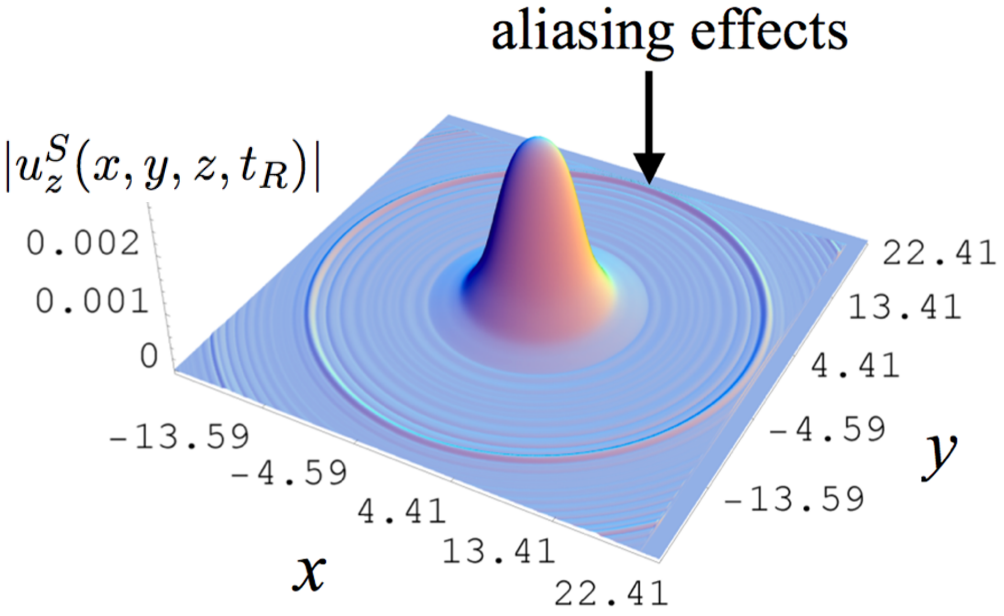

Figure 1.10 – Numerical results of $|u_z^S(x,y,z,t_R)|$ for a circular aperture, with $t_v = 0$ s, $z = 0.1$m, $L = 0.1$ mm over the range $-23 \leq x \leq 23$ mm, $-23 \leq y \leq 23$, figure taken from [6].

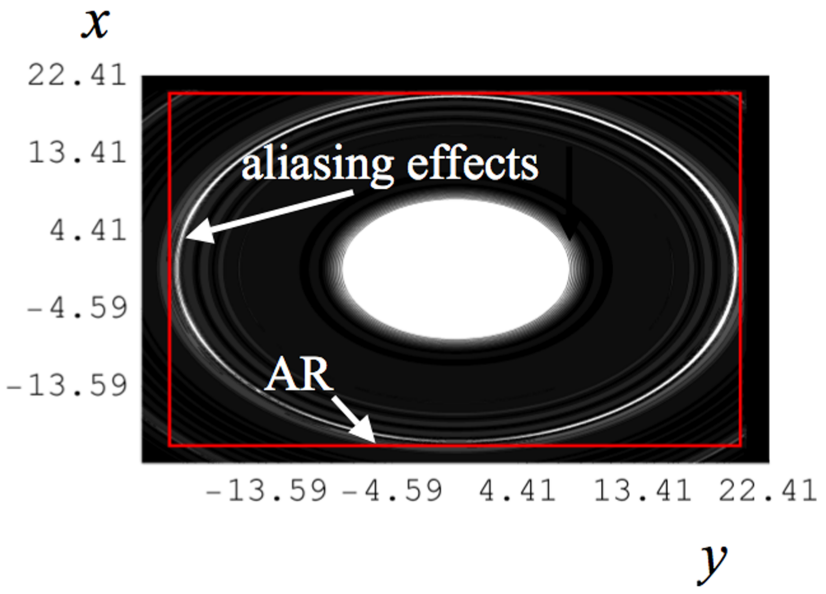

Figure 1.11 – Contour plot of numerical results of $|u_z^S(x, y, z, t_R)|$ for a circular aperture, with $t_v = 0$ s, $z = 0.1$m, $L = 0.1$ mm over the range $-23 \leq x \leq 23$ mm, $-23 \leq y \leq 23$, figure taken from [6].

2.1

Chapter 2

Optical signal processing.

2.1 The 'thin' element approximation

In previous chapter we specifically examined the propagation of a wavefield in free space, which we model in the paraxial regime using the Fresnel transform. In this chapter we examine how different optical elements can be used to modify an optical wavefield and to perform different types of signal processing operations on an optical signal. To proceed we must first address the question of how different optical elements, such as a lens or a diffraction grating, interact with an incident optical wavefield. Once we have established this we will then consider several important optical signal processing systems. The model that we use is the so-called 'thin element approximation' or TEA.

We begin our analysis by examining the optical system depicted in Fig. 2.1. Here a plane wave is incident on an object located in the input plane. The field immediately in the input plane is defined as $U(X)$ and we now use the Fresnel transform to describe the optical wavefield propagating in free space that is incident upon an optical element, in this case a 'thin lens'. From our previous considerations we can now use the Fresnel transform to relate the field in the input plane, $U(X)$, to the field 'just before' the optical element, $u_z^-(x')$, specifically we write:

$$u_z^-(x) = \frac{\exp\left(\frac{j2\pi z}{\lambda}\right)}{\sqrt{j\lambda z}} \int_{-\infty}^{\infty} U(X) \exp\left[\frac{j\pi}{\lambda z}(x-X)^2\right] dX. \tag{2.1}$$

Now we wish to model the effect of the 'thin element' and to relate the field $u_z^-(x')$, 'just before' the optical element to that 'just after' the optical element. We refer to the field just after the 'thin element' as $u_z(x)$ and relate it to $u_z^-(x')$ with the following

expression:

$$u_z(x) = u_z^-(x')t(x'), \tag{2.2}$$

where $t(x')$ is referred to as the transmittance function and describes how the optical element effects the optical wavefield. It is quite a simplistic assumption. For one implicit in this description is that the element is 'thin'. This means that we ignore the physical volume of the element itself assume that the x' plane and x plane in fact lie on top of each other - this is what is meant by 'thin'. The function $t(x')$ is usually derived

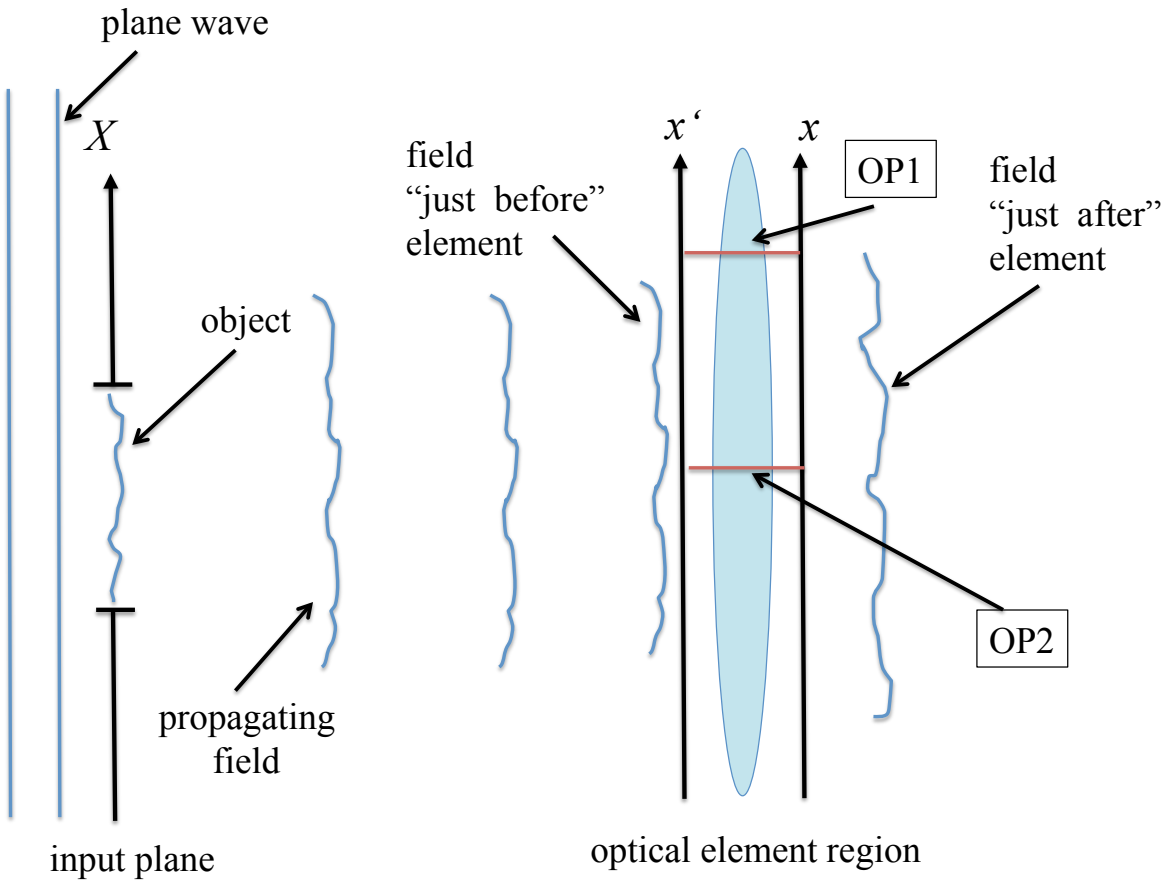

Figure 2.1 – Schematic illustrating the 'thin' element approximation. A field is incident on an optical element and we wish to relate the field at plane x' to that at x. The two red lines through the optical element, OP1 and OP2, are two ray traces through the optical element. We note that in general the optical element will have a refractive index different from free space, i.e. $n_e \neq 1$. Hence the ray traveling along OP1 will accumulate a different amount of phase than the ray that moves along OP2.

by using a ray optics approach. In general the refractive index of the optical element, $n_e \neq 1$, and hence rays that transverse different parts of the optical element acquire different amounts of phase, or equivalently the optical path length that each ray sees depends on its location in x'. For example if we imagine the optical element as being a thin converging glass lens with $n_e \approx 1.5$, then the physical structure of the element will perform a space dependent phase transformation on the incident optical field. In the case of the a 'thin' converging lens, the transmittance function takes the form

$$t(x) = \exp\left(\frac{-j\pi x^2}{\lambda f}\right), \tag{2.3}$$

where f is the focal length of the lens.

It is interesting to compare the expression in Eq. (2.2) to that of an on-axis paraxial point source that we saw in previous lectures (on-axis implies that $X_0 = 0$)

$$\frac{\exp(jkz)}{\sqrt{z}} \exp\left[\frac{j\pi (x - X_0)^2}{\lambda z}\right]$$

The most significant difference apart from the constant complex term,
$\exp(jkz)/\sqrt{z}$, is that the sign of the quadratic phase term in $t(x)$ is negative. In the following sections we will discuss how a simple converging lens can be used to implement a Fourier transform.

We conclude this section by noting that all optical elements in this document will be modelled as 'thin' elements, where we define a plane 'just before' and 'just after' the optical element and relate the field before and after the optical element using a transmittance function to describe the effect of the optical element on the field. The derivation of this transmittance function relies on ray or geometrical optics which in general will modify both the phase and amplitude of the incident optical field. This relationship is summarized with Eq. (2.2).

2.2 The optical Fourier transform

It is convenient here to first consider the formal definition of the Fourier transform, operating on some signal $u(x)$. This can be expressed mathematically as

$$\begin{aligned} \tilde{u}(v) &= FT\{u(x)\}(v) \\ &= \int_{-\infty}^{\infty} u(x) \exp(-j2\pi xv) dx, \end{aligned} \tag{2.4}$$

and the inverse Fourier transform operation is defined as

$$\begin{aligned} u(x) &= IFT\left\{\tilde{u}(v)\right\}(x) \\ &= \int_{-\infty}^{\infty} \tilde{u}(v)\exp(+j2\pi xv)dv, \end{aligned} \tag{2.5}$$

where x and v are the spatial and spatial frequency coordinates. The Fourier transform is a mathematical tool that allows us to decompose any signal into its constituent frequency components. It is more convenient to decompose the signal onto the periodic function $\exp(j2\pi vt) = \cos(2\pi vt) + j\sin(2\pi vt)$. In general $u(v)$ is a complex signal. The function $\arg\{\tilde{u}(v)\}$, is the phase distribution. It is a property of the Fourier transform that for a real signal, i.e. one that does not have a complex conjugate, that $|\tilde{u}(v)| = |\tilde{u^*}(-v)|$, where $*$ indicates a complex conjugate operation.

Temporal signals are often analyzed for their positive frequency components, negative frequencies have a more difficult interpretation that must take causality into consideration. In the paraxial optics regime however we consider complex signals that can have positive and negative spatial frequencies. For us, negative and positive spatial frequencies have an intuitive physical interpretation: they are the angles which plane waves propagate relative to the optical axis, the angle being related to the size spatial frequency component, higher angles imply a higher spatial frequency. We will now examine how two different optical systems: System A and B, can reproduce an integral relationship of the form of Eq. (2.4). Once we have established this result we can then interpret the relationship between the input and output distribution using a Fourier transform relationship. This relationship will allow us to interpret many different optical systems in terms of signal processing operations, for example later we will consider an important imaging system - the 4f imaging system - in terms of two successive Fourier transforms. This interpretation of optics is known as Fourier optics.

System A

As we have just noted it is possible to perform a Fourier transform optically using a simple converging lens. Before we consider a lens in these terms we first observe that one of the most important properties of a lens is that it collects light and concentrates the associated power in the focus of that lens. From an optical design viewpoint it is important to understand how this works, for the design of solar concentrators. The practical implication is that one could imagine placing a solar cell in the focus of a lens (or as we shall later see other optical concentrators) to improve the amount of electricity

we can generate for a given amount of sunlight. Hence when we consider the optical system depicted in Fig. 2.2, we expect that there will be a concentration of light at the geometrical focus.

$$u_z(x) = \frac{\exp\left(\frac{j2\pi z}{\lambda}\right)}{\sqrt{j\lambda z}} \int_{-\infty}^{\infty} U(X) \exp\left\{\frac{j\pi}{\lambda z}\left[(x-X)^2\right]\right\} dX,$$

and consider how to calculate the output distribution when we set the input function $U(X) = t(X)O(X)$, where $O(X)$ is the transmittance function of some general 'thin' object. The optical problem we are examining is depicted in Fig. 2.2. Subbing $t(X)O(X)$

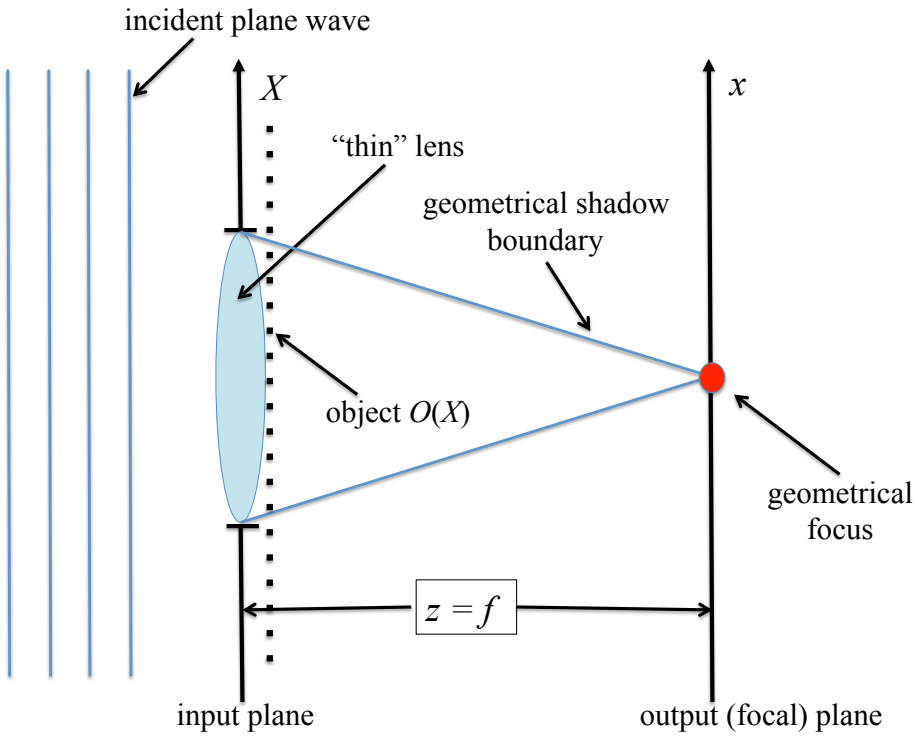

Figure 2.2 – Fresnel transform of a 'thin' converging lens

into the Fresnel transform we find that

$$u_z(x) = \frac{\exp\left(\frac{j2\pi z}{\lambda}\right)}{\sqrt{j\lambda z}} \int_{-\infty}^{\infty} O(X) \exp\left(\frac{-j\pi X^2}{\lambda f}\right) \exp\left\{\frac{j\pi}{\lambda z}\left[(x-X)^2\right]\right\} dX, \tag{2.6}$$

Dropping the leading complex constant, $\exp\left(\frac{j2\pi z}{\lambda}\right)/\sqrt{j\lambda z}$, we now expand the squared expression in Eq. (2.6) to give

$$u_z(x) = \exp\left(\frac{j\pi x^2}{\lambda z}\right)\int_{-\infty}^{\infty} O(X)\exp\left[\frac{j\pi X^2}{\lambda}\left(\frac{1}{z}-\frac{1}{f}\right)\right]\exp\left(\frac{-j2\pi xX}{\lambda z}\right)dX. \tag{2.7}$$

On examination of Eq. (2.7), we can see that when $z = f$, i.e. at the focal plane then the quadratic phase terms cancel out and the integral reduces to

$$\begin{aligned} u_z(x) &= \exp\left(\frac{j\pi x^2}{\lambda f}\right)\int_{-\infty}^{\infty} O(X)\exp\left(\frac{-j2\pi xX}{\lambda f}\right)dX. \\ &= \exp\left(\frac{j\pi x^2}{\lambda f}\right) FT\left\{O(X)\right\}\left(\frac{x}{\lambda f}\right) \end{aligned} \tag{2.8}$$

Comparing Eq. (2.8) to Eq. (2.4), we see that both integrals have a similar form with two important differences.

- There is a leading quadratic phase factor: $\exp\left(\frac{j\pi x^2}{\lambda f}\right)$ in Eq. (2.8), which will disappear when we examine the intensity of the Fourier distribution in the focal plane.
- We also recognize that the spatial frequency variable, v in Eq. (2.4), is now given by $v = x/(\lambda f)$. Hence the optical system performs a scaled Fourier transform where the spatial frequency variable depends on both the wavelength and focal length of the converging lens.

A rectangular aperture

It is perhaps useful at this stage to examine a specific and important example so as to gain some insight into the behaviour of this system. Setting $O(X) = p_L(X)$, where

$$\begin{aligned} p_L(X) &= 1, \text{if } |X| < L \\ &= 0, \text{ otherwise,} \end{aligned}$$

and subbing into Eq. (2.8), we find that the distribution in the focal plane is given by

$$\begin{aligned} u_z(x) &= \exp\left(\frac{j\pi x^2}{2f}\right)\int_{-L}^{L}\exp\left(\frac{-j2\pi xX}{\lambda f}\right)dX. \\ &= \exp\left(\frac{j\pi x^2}{2f}\right)\frac{\lambda f}{\pi}\frac{\sin\left[2\pi\left(\frac{L}{\lambda f}\right)x\right]}{x}. \end{aligned} \tag{2.9}$$

The expression above, which actually is a scaled sinc function, describes the field in the focal plane of a lens - we plot the intensity of this field in Fig. 2.3. The field in the input plane extends over a distance $2L = 20$ cm, see figure caption for details. However from Fig. 2.3, we can see that now most of this power lies approximately between $-1 \leq x \leq 1$ microns. This results in an approximately 100,000 factor increase in the power density.

We also recognize that the width of the sinc function depends on the width of the aperture function $p_L(X)$, and furthermore that as we limit $L \to \infty$, or if we limit $\lambda \to 0$, then Eq. (2.9) limits to a Dirac delta function which is equivalent to a geometrical ray tracing model.

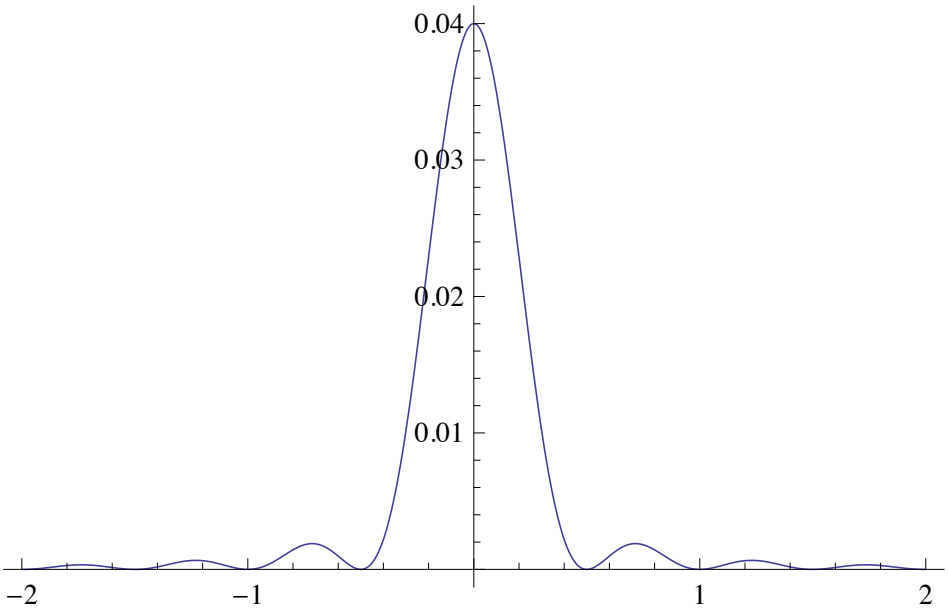

Figure 2.3 – Plot of Eq. (2.9) when $L = 10$ cm, $f = 20$ cm, $\lambda = 500$ nm, the units along x axis are in microns (10^{-6}).

Inclusion of a grating

We now consider what happens when we examine another special function, a sinusoidal grating, in combination with an apertured lens. In this case the input field $U(X)$ becomes

$$O(X) = [1 + \cos(2\pi\Gamma X)]\, p_L(X), \tag{2.10}$$

where Γ is the grating frequency. Making use of the familiar relationship $\cos(\Theta) + j\sin(\Theta) = \exp(j\Theta)$, it is also possible to solve this Fresnel integral analytically and we plot the result in Fig. 4, see caption for details. The first thing we observe is that there are now three intensity peaks in the focal plane:

- A peak at the center of the distribution as in Fig. 2.3
- Two additional peaks located at $x \approx \pm\Gamma(\lambda f)$.

We can understand this result by making use of some Fourier transform pairs, for example we note the following well known relationships:

$$\begin{aligned} FT\{\cos(2\pi\Gamma x)\}(v) &= \frac{1}{2}[\delta(v-\Gamma) + \delta(v+\Gamma)] \\ FT\{1\}(v) &= \delta(0). \end{aligned} \tag{2.11}$$

We also make use of the convolution property of the Fourier transform. We define two general functions $f(x)$ and $g(x)$ that have Fourier transforms given by $\tilde{f}(v)$ and $\tilde{g}(v)$. The following relationship then follows

$$FT\{f(x)g(x)\}(v) = \tilde{g}(v) \star \tilde{f}(v), \tag{2.12}$$

where $\star$ represents a convolution relationship which we explicitly define as

$$\tilde{g}(v) \star \tilde{f}(v) = \int_{\infty}^{\infty} \tilde{f}(X)\tilde{g}(x-X)dX. \tag{2.13}$$

We remember that for this optical system there is a scaled Fourier relationship between the field in the input plane and the output plane, [neglecting the leading quadratic phase factor in Eq. (2.8)], hence we can use the result from Eq. (2.9) is convolved with the Dirac delta functions from Eq. (2.11) resulting in the two additional peaks to yield:

$$u_z(x) = \exp\left(\frac{j\pi x^2}{2f}\right)\frac{\lambda f}{\pi}\frac{\sin\left[2\pi\left(\frac{L}{\lambda f}\right)x\right]}{x} \star \left[\delta(0) + \frac{1}{2}\delta(x-\lambda f\Gamma) + \frac{1}{2}\delta(x+\lambda f\Gamma)\right] \tag{2.14}$$

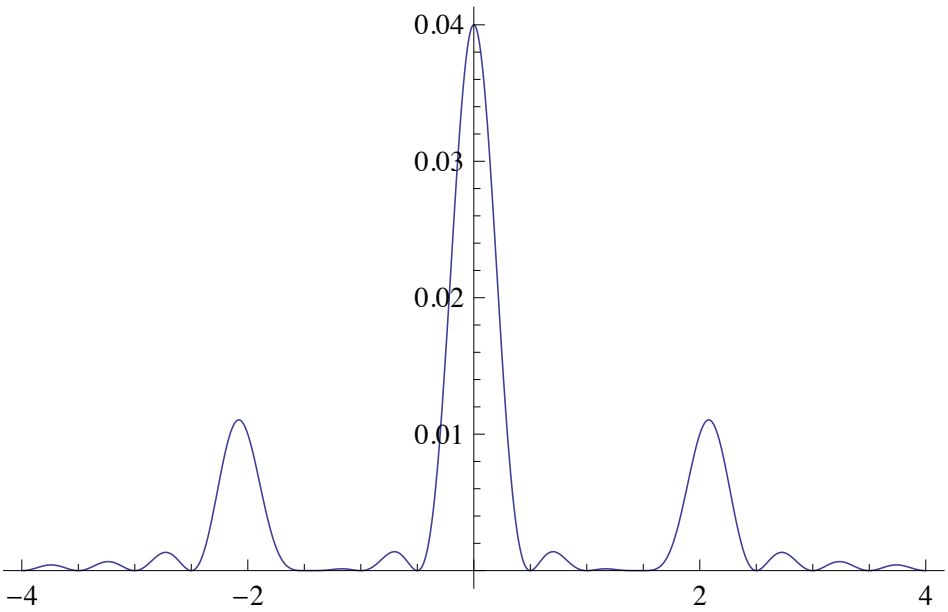

Figure 2.4 – Plot of Eq. (2.14) when $L = 10$ cm, $f = 20$ cm, $\lambda = 500$ nm, and $\Gamma = 20$, the units along x axis are in micrometers (10^{-6}).

System B

We now examine a second optical system for performing optical Fourier transforms depicted in Fig. 2.5. Unlike the Fourier transforming system in Fig. 2.2, the object that we wish Fourier transform is not placed up against the lens but rather is located in a plane a distance d from the lens plane. In this figure we denote the lens plane with the coordinates X_{L}. In order to simplify the analysis of this optical system we now make an important assumption namely that the extent of the lens is infinite. Examining Fig. 2.5, we recognize that there is a Fresnel transform relationship between the input plane and the lens plane and secondly that we have already, in our analysis of System A, explored the relationship between the distribution at the lens plane and that in the back focal plane of the lens. This relationship is expressed mathematically by Eq. (2.8).

Again in Fig. (2.5), we note that the field immediately after the object, which illuminated with a normally incident plane wave, is given by $U(X)$. This field is then Fresnel transformed a distance d whereupon it is incident upon the lens situated in the lens plane, and with a coordinate system, X_{L}. We refer to the field in the lens plane as $u_d(X_{\mathrm{L}})$. We now make use of a result from an earlier discussion of the Fresnel transform, noting again that the Fresnel transform can be described as a convolution relationship,

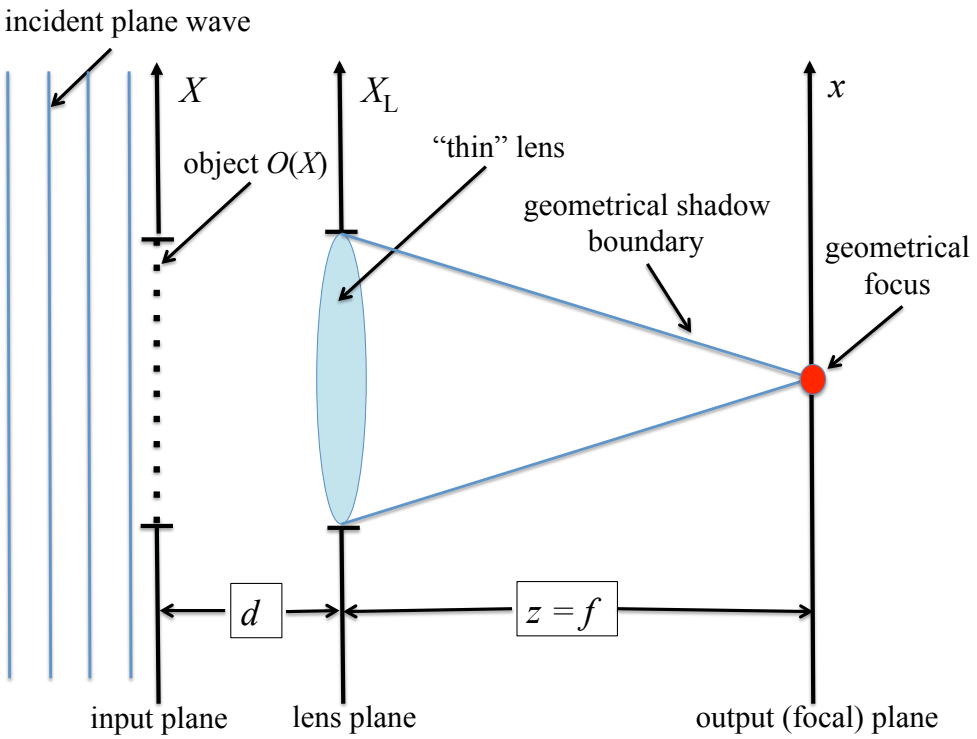

Figure 2.5 – Schematic of a second optical system for performing the Fourier transform, i.e. System B.

i.e.

$$u_d(X_{\mathrm{L}}) \quad = \quad O(x) \star \exp\left(\frac{j\pi x^2}{\lambda d}\right), \tag{2.15}$$

where we drop the complex constant $\exp\left(\frac{j2\pi d}{\lambda}\right)/\sqrt{j\lambda d}$. We will now examine the Fourier transform of Eq. (2.15), making use of the following analytical result: the Fourier transform of $\exp\left(\frac{j\pi x^2}{\lambda d}\right)$ is $\exp\left(-j\pi\lambda z v^2\right)$.

$$\tilde{u}_d(v) \quad = \quad \tilde{O}(v)\exp\left(-j\pi\lambda d v^2\right), \tag{2.16}$$

where

$$\tilde{O}(v) = FT\left\{O(X)\right\}(v) \tag{2.17}$$

and where

$$\tilde{u}_d(v) = FT\left\{u_d(X_{\mathrm{L}})\right\}(v). \tag{2.18}$$

We note from Eq. (2.8) that there is a scaled Fourier transform relationship between the field incident on the lens and the back focal plane of that lens (which is assumed to be infinite in extent, see integration limits), and hence that the following relationship for System B holds:

$$\begin{aligned} u_z(x) &= \exp\left(\frac{j\pi x^2}{\lambda f}\right) \int_{-\infty}^{\infty} u_d(X_{\mathrm{L}}) \exp\left(\frac{-j2\pi x X_{\mathrm{L}}}{\lambda f}\right) dX_{\mathrm{L}}. \\ &= \exp\left(\frac{j\pi x^2}{\lambda f}\right) FT\left\{u_d(X_{\mathrm{L}})\right\}\left(\frac{x}{\lambda f}\right) \\ &= \tilde{O}\left(\frac{x}{\lambda f}\right) \exp\left[-\frac{j\pi x^2}{\lambda f}\left(1-\frac{d}{f}\right)\right]. \end{aligned} \tag{2.19}$$

So we can see that at the back focal plane of the lens again we have a scaled FT relationship between the input field, $O(X)$ and $u_z(x)$. Again we note the presence of a leading quadratic phase factor. However for the special case when $d = f$ we see that this quadratic phase factor disappears completely yielding a pure scaled FT relationship between input and output planes.

Beam shaping

We now consider the following question: Is it possible to produce a desired intensity in the focal plane of a lens from a specially designed transmittance function? There are many practical applications for this type of problem such as the ability to produce particular intensity patterns for lithography or image projection. From Eq. (2.14), we see that gratings of different spatial frequencies can produce spots of light in the correponding Fourier plane. In fact we can extend this result to more complicated gratings containing a sum of different grating frequencies. Each grating will produce two additional peaks according to the $x = \pm\Gamma(\lambda f)$.

There are several disadvantages to using a lens and and grating combination to produce a desired light spot pattern in a given plane. The first is that large lenses are expensive to manufacture and suffer from aberrations, particularly when they have a large finite extent. A second practical consideration is the weight of a large lens required for solar concentrators. A similar type of problem was considered by Fresnel himself when he was tasked with developing a projection lens for light houses, so that the light from a small fire could be transmitted as far out to sea as possible. His solution was to develop a Fresnel lens. In the thin lens approximation a Fresnel lens and a standard converging lens are mathematically equivalent. Both produce a quadratic phase distribution in the plane immediately behind the lens. A Fresnel lens however looks quite different and can

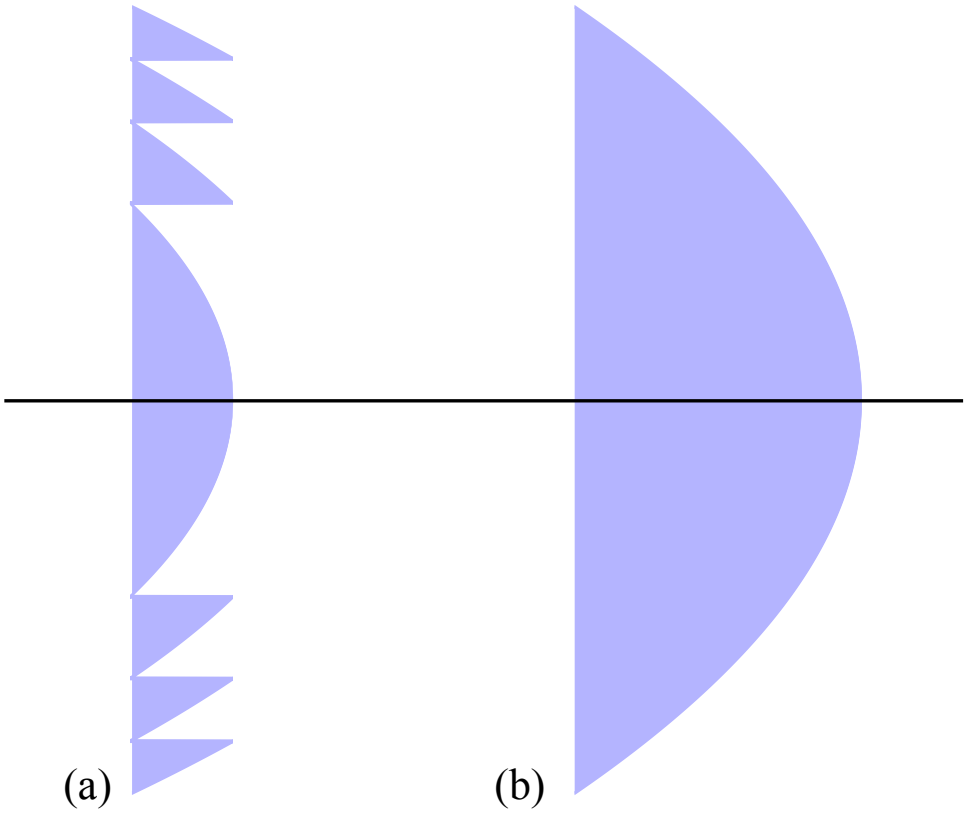

Figure 2.6 – Optical elements that produce identical output phase distributions, modeling a converging lens: (a) Fresnel lens, and (b) its equivalent traditional lens form. The Fresnel lens produces the same focusing effect as (b) within the 'thin element approximation' .

be seen in the figure below. What is it about this structure that allows it to mimic the behavior of normal lens? It follows from the assumptions of the 'thin element approximation' where a ray tracing approach is taken to define the transmittance function of optical element. In this case both the Fresnel lens and the standard converging lens are phase only structures and each introduce the same optical path length for rays incident on the respective structures.

A second comment is related to the sinusoidal grating. This grating acts to reduce the power transmitted by the input function $U(X)$. Ideally we would like to develop a thin phase function that transfers all the power incident on the input aperture $p_L(X)$ to the focal plane.

The problem of producing a desired intensity in the Fourier plane of such an optical system can be approached in a completely different manner assuming that the user is interested in the intensity distribution only. In this case we wish to maximize the amount of light power that propagates through the system and hence we wish to use a transmittance function that modifies only the phase of an incident plane wave. As we shall later see when we examine the phase retrieval problem, it is possible to produce the same intensity distribution in the Fourier plane with many different phase structures. The problem of choosing an appropriate phase structure for a desired intensity distribution can be solved theoretically using an iterative Gerschberg-Saxton algorithm.

2.3 The ABCD transform

In this section we wish to introduce an important general diffraction integral. This more general diffraction integral is sometimes referred to as a Linear Canonical Transform (LCT) or an ABCD transform. In Ref. [17], it is shown how diffraction theory can be related to ray matrices, providing a convenient method of describing the propagation of a field through several optical elements. The field at the output of such a system will in general be in a mixed space-spatial frequency domain, and can be interpreted mathematically as an LCT [17]. This is in contrast to the Systems A and B that were discussed in the previous sections, which considered the spatial and spatial frequency extent of the signal only. There are other optical systems such as a fractional Fourier transform system that also operate in a mixed space-spatial frequency domain.

We begin again with an input field $U(X)$ and wish to determine the distribution $u(x)$ in the output plane, see Fig. 2.7. Here several different optical elements and sections of free-space propagation act on the input signal, which can be described with the matrix parameters $ABCD_{\mathrm{A}}$, (where the subscript A is used to indicate that the field represents an analytical or continuous mathematical function). We now define the LCT or ABCD transform as follows:

$$u(x) = \begin{cases} LCT_{ABCD}\left\{U(X)\right\}(x), \\ \left(\sqrt{j\lambda B}\right)^{-1} \int U(X) \exp\left[\frac{j\pi}{\lambda B}\left(Dx^2 - 2xX + AX^2\right)\right] dX, & \text{if } B \neq 0 \\ \left(\sqrt{j\lambda D^{-1}}\right)^{-1} U(Dx) \exp\left(\frac{j\pi CDx^2}{\lambda}\right) & \end{cases} \tag{2.20}$$

We note that since $|AD - BC| = 1$, we have 3 independent variables and can thus typically eliminate C. This transform reduces to other more well known transforms by appropriately choosing the values for ABCD. For example the following matrices

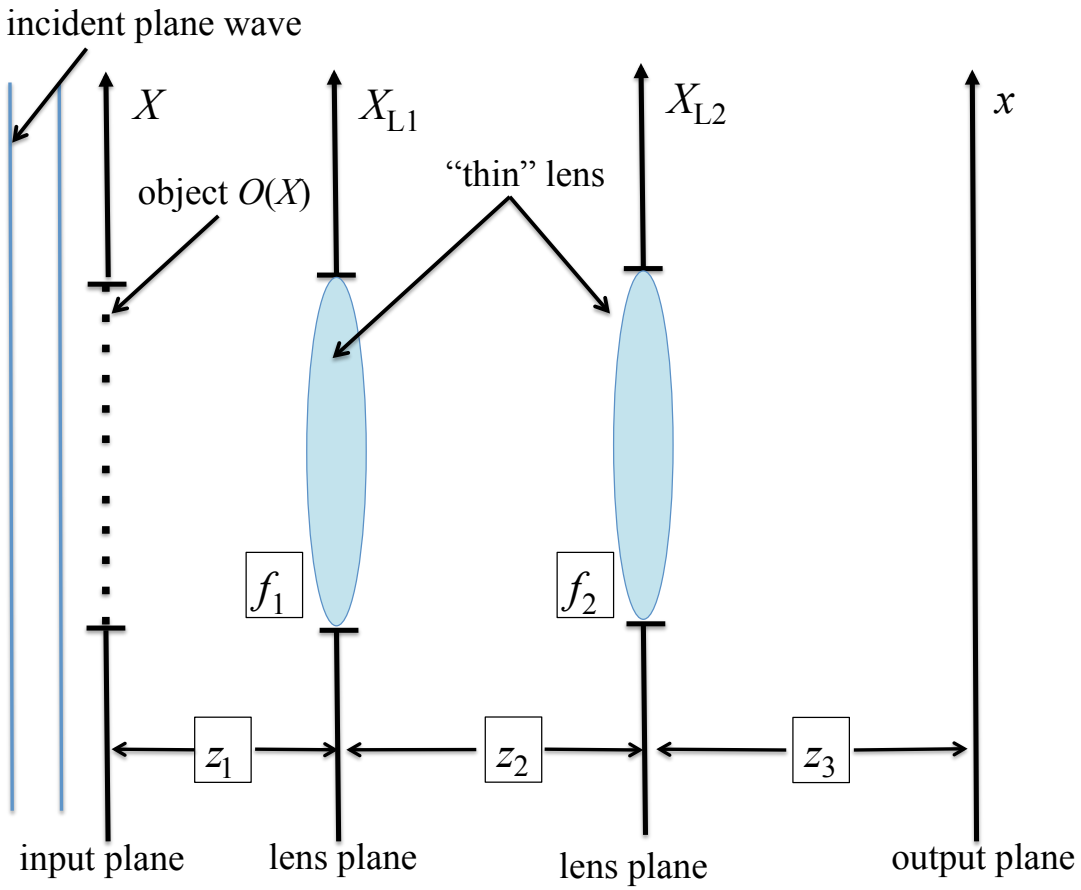

Figure 2.7 – An optical system consisting of several optical lenses and sections of free space. The relationship between the input and output planes can be determined using an ABCD transform.

describe the scaled (by a factor q) Fourier Transform (FT),

$$\text{FT} = \begin{pmatrix} 0 & q \\ -\frac{1}{q} & 0 \end{pmatrix}, \tag{2.21}$$

Fresnel (FST) propagation (a distance z),

$$\text{FST} = \begin{pmatrix} 1 & z \\ 0 & 1 \end{pmatrix}, \tag{2.22}$$

the effect of a thin converging lens (focal length, f) or Chirp Modulation Transform (CMT),

$$\text{CMT} = \begin{pmatrix} 1 & 0 \\ -\frac{1}{f} & 1 \end{pmatrix}, \tag{2.23}$$

an imaging operation (magnified by M),

$$\text{M} = \begin{pmatrix} M & 0 \\ 0 & \frac{1}{M} \end{pmatrix}. \tag{2.24}$$

and a dimension-less fractional Fourier transform (FRT) operation of fractional angle θ,

$$\text{FRT} = \begin{pmatrix} \cos(\theta) & q\sin(\theta) \\ -\sin(\theta)/q & \cos(\theta) \end{pmatrix}, \tag{2.25}$$

where q is the (scaled) focal length. A significant benefit of the ABCD transform is that it allows one to concatenate several different optical systems together to form optical systems with different properties. In this example we write down the different matrices that make up the optical system depicted in Fig. 2.7. We see that it is possible to change the $ABCD$ parameters of the optical system by varying the physical parameters, z_1, z_2, and z_3, as well as the focal lengths of the two lenses, f_1 and f_2.

$$\begin{aligned} \begin{pmatrix} A & B \\ C & D \end{pmatrix} &= \begin{pmatrix} 1 & z_3 \\ 0 & 1 \end{pmatrix}\begin{pmatrix} 1 & 0 \\ -\frac{1}{f_2} & 1 \end{pmatrix}\begin{pmatrix} 1 & z_2 \\ 0 & 1 \end{pmatrix}\begin{pmatrix} 1 & 0 \\ -\frac{1}{f_1} & 1 \end{pmatrix}\begin{pmatrix} 1 & z_1 \\ 0 & 1 \end{pmatrix}, \\ &= \begin{pmatrix} \frac{f_1(f_2-z_3)+z_2z_3-f_2(z_2+z_3)}{f_1f_2} & \frac{-z_1[-z_2z_3+f_2(z_2+z_3)]+f_1[f_2(z_1+z_2+z_3)-z_3(z_1+z_2)]}{f_1f_2} \\ -\frac{f_1+f_2-z_2}{f_1f_2} & \frac{f_1(f_2-z_1-z_2)+z_1(z_2-f_2)}{f_1f_2} \end{pmatrix} \end{aligned} \tag{2.26}$$

We shall later use this ABCD transform to discuss holographic imaging systems and how the performance of such an optical system can be optimized for specific imaging applications. We note that these ABCD matrices are used in geometrical optics to trace the path of an optical ray passing through the system. Here we can extend the use of these ray matrices to wave optics and specifically include diffraction effects and the wave nature of light. There is however a significant theoretical short-coming with this type of approach. It is implicitly assumed that all optical elements are infinite in extent. While this cannot truly represent a real physical system, it nevertheless remains a very useful approximation that can be used to control speckle size and orientation as well to design speckle metrology systems that can measure both in-plane and out-of-plane

tilting with controllable accuracy and range. We can however extend the analysis to include Gaussian apertures which approximate very well the effect of hard apertures. This can be achieved using the LCT formulation with the help of complex numbers in the ABCD parameters. Hence a soft-Gaussian aperture, defined as,

$$p_G(x) = \exp\left(\frac{-x^2}{\sigma^2}\right), \tag{2.27}$$

is represented using the following ABCD matrix

$$\begin{pmatrix} 1 & 0 \\ \frac{j\lambda}{\pi\sigma^2} & 1 \end{pmatrix}. \tag{2.28}$$

2.4 The 4-f imaging system

We now turn our attention to an important type of imaging system, the so-called 4-f imaging system, which consists of concatenating two OFT system's together, as shown in Fig. 2.8. We can describe this type of optical system as follows:

$$\begin{pmatrix} -\frac{f_2}{f_1} & 0 \\ 0 & -\frac{f_1}{f_2} \end{pmatrix} = \begin{pmatrix} 0 & f_2 \\ -\frac{1}{f_2} & 0 \end{pmatrix} \begin{pmatrix} 0 & f_1 \\ -\frac{1}{f_1} & 0 \end{pmatrix}, \tag{2.29}$$

which from Eq. (2.24) we recognize as an imaging system that forms an inverted image that is magnified by a factor of $-f_2/f_1$. Here we note a feature of this optical system, it has an aperture located in the back Fourier plane of OFT system 1 or OFT1. This aperture is known as the limiting aperture of the optical system. In the analysis of optical imaging systems it is traditionally assumed that the limiting aperture is located in a Fourier plane and that all other optical elements have an infinite extent. This useful fiction allows us to attribute any diffraction effects to an aperture in a single plane, and greatly simplifies the analysis of imaging systems in general. For general imaging systems usually a geometrical optics analysis is first performed so that the system's magnification and exit pupil can be determined. Let us consider a unit magnification system, where $f_1 = f_2$, and examine what happens to the field, $U(x_{\text{obj}})$ in the object plane (input plane) of the 4-f system depicted in Fig. 2.8. Any physically realisable optical signal can be expressed in terms of its Fourier transform, which represent the different spatial frequencies present in the signal. Each one of these spatial frequencies components maps in the Fourier domain to a set of Dirac delta functions, each weighted with a different complex number. The first operation that occurs in the 4-f system is an optical Fourier transform, implemented by OFT1, see Fig. 2.9. In Fig. 2.9, we see

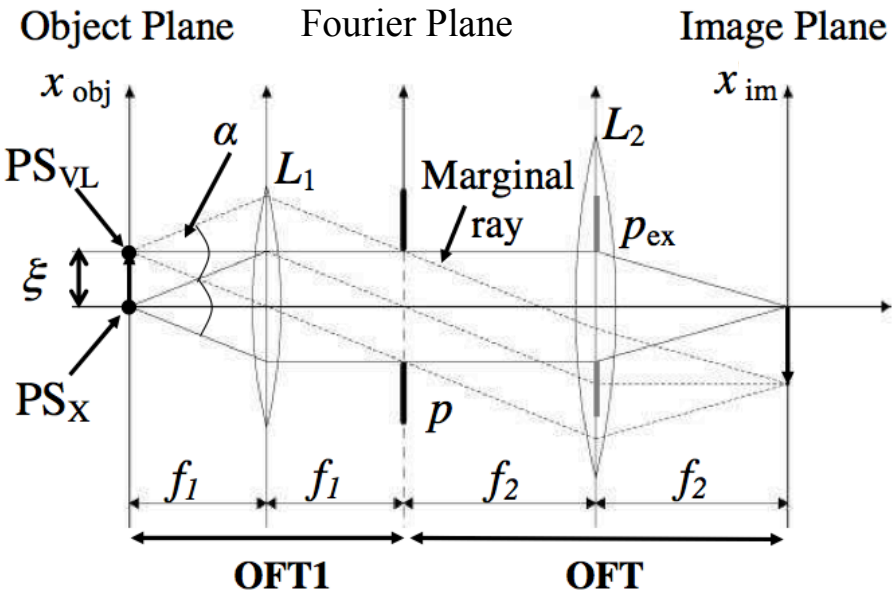

Figure 2.8 – Schematic of a 4-f imaging system

that a given spatial frequency maps to a definite Dirac delta function in the Fourier plane. This Fourier distribution is filtered by a limiting aperture that allows only those spatial frequencies that lie within the aperture opening to contribute to the final image distribution, $u(x_{\mathrm{im}})$. Let us consider the signal processing operations that occur:

- The object signal, $U(x_{\mathrm{obj}})$, is Fourier transformed, to yield, $\tilde{U}(x_{\mathrm{FP}})$.
- This later distribution is filtered by an aperture function which we define as $H(x_{\mathrm{FP}})$,
- Finally, the resulting filtered distribution, $H(x_{\mathrm{FP}})\tilde{U}(x_{\mathrm{FP}})$ is subject to a second OFT operation to yield the image distribution $U_{\mathrm{im}}(x_{\mathrm{im}})$.

Making use of the convolution property of the Fourier transform it is possible to relate the filtered image plane distribution to the unfiltered object plane distribution with the following relationship

$$U_{\mathrm{im}}(x_{\mathrm{im}}) = h\left(x_{\mathrm{obj}}\right) \star U(x_{\mathrm{obj}}), \tag{2.30}$$

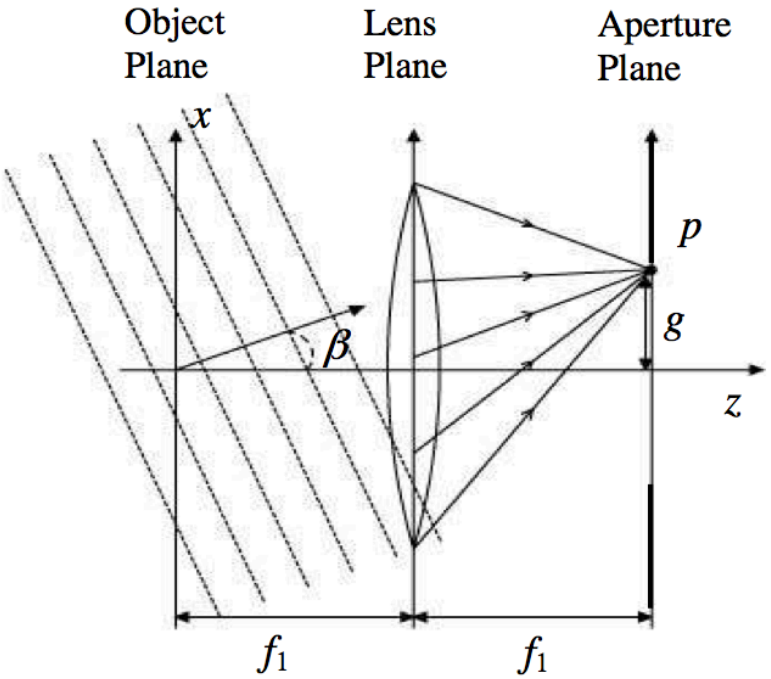

Figure 2.9 – Schematic of the first OFT module of the 4-f imaging system depicted in Fig. 2.8.

where $h\left(x_{\mathrm{obj}}\right)$ is known as the point spread function of the optical system and is related to the actual Fourier plane aperture as

$$H\left(x_{\mathrm{FP}}\right) = FT\left\{h\left(x_{\mathrm{obj}}\right)\right\}\left(\frac{x_{\mathrm{FP}}}{\lambda f_1}\right). \tag{2.31}$$

In the next chapter we shall examine the 4-f imaging system in more detail extending the analysis so that both coherent and incoherent light sources can be considered.

Chapter 3

Coherent and incoherent imaging systems.

The analysis of imaging systems can be approached in many different ways. For example the system magnification, input and exit pupils as well as vignetting conditions can be figured out using ray tracing techniques. The diffraction analysis is then usually simplified, see for example [7]. Although there may be many different apertures and stops in the imaging system, all these effects are lumped together and a projection of the systems limiting aperture, i.e. the system's entrance or exit pupil is used to account for the effects of diffraction. The entrance and exit pupils of several optical systems are examined in the appendices. To repeat then in a diffraction limited system (where optical elements do not suffer from aberrations) the effects of diffraction are associated with a single limiting aperture located somewhere in the optical system.

A ray tracing analysis of such a system will map a point in the object plane to a point in the image plane. However we expect from our analysis in Section 2.4, that the effects of diffraction will act to reduce this perfect point to point mapping by smearing the power associated with a particular point source in the object plane over a small but significant region in the image plane.

Here we are going to look at a special type of a system called a 4-f imaging system, which has several appealing properties that make it useful for analysis. And it is possible to reduce general optical imaging systems - with a ray tracing analysis - so that they can be considered as an effective 4-f imaging system. A schematic of the system is presented in Fig. 3.1. We can relate the object field to the image distribution with the following general superposition formula

$$U_{\mathrm{im}}(x_{\mathrm{im}}) \quad = \quad \int_{-\infty}^{\infty} h\left(x_{\mathrm{im}};\zeta\right) U_G\left(\zeta\right) d\zeta, \tag{3.1}$$

where $h\left(x_{\mathrm{im}};\zeta\right)$ is known as the Point Spread Function (PSF) of the imaging system. U_G is the geometrical image and is defined as

$$U_G(\zeta) \;=\; \sqrt{\frac{1}{M}}U_{obj}\left(\frac{\zeta}{M}\right), \tag{3.2}$$

where M is the system magnification. Usually it is assumed that the system is a linear

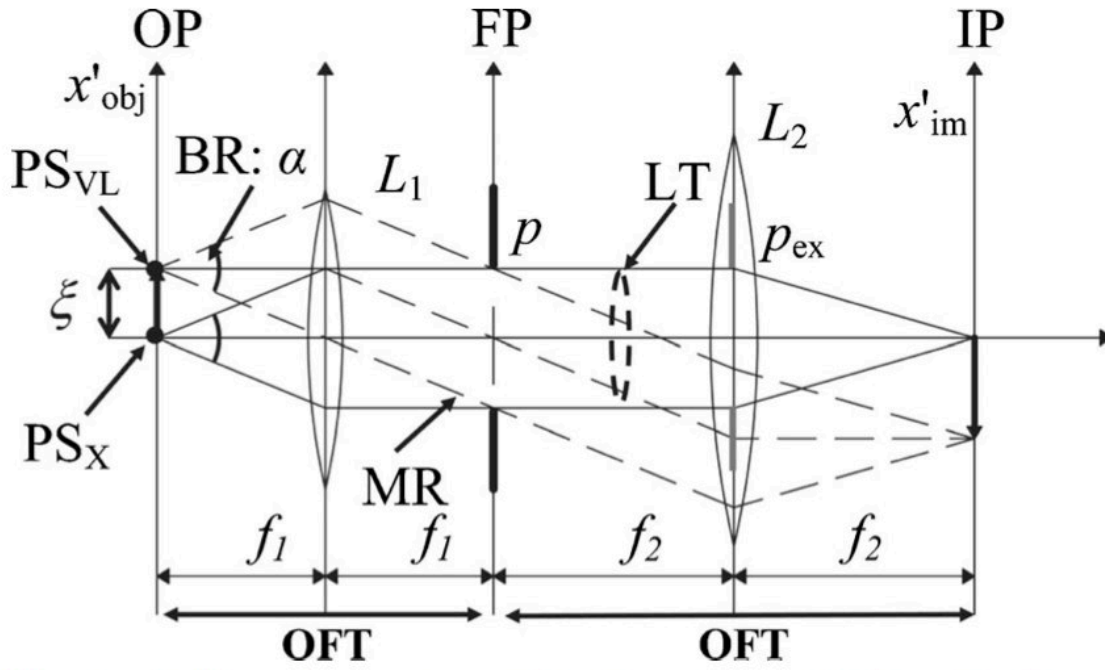

Figure 3.1 – Schematic illustrating a 4-f imaging system. OP, object plane; FP, Fourier (aperture) plane; IP, image plane; MR, marginal ray; LT, light tube; BR: α, bundle of rays (defined by cone angle α).

shift invariant system. If that assumption is made then Eq. (3.1) can be expressed as a convolution operation

$$U_{\mathrm{im}}(x'_{\mathrm{im}}) \;=\; \int_{-\infty}^{\infty} h\left(x'_{\mathrm{im}}-\zeta\right)U_G\left(\zeta\right)d\zeta, \tag{3.3}$$

and where the PSF is given by [7]

$$h\left(x'_{\mathrm{im}}\right) \;=\; \frac{A}{\sqrt{\lambda d_{ex}}}\int_{-\infty}^{\infty} p^{ex}\left(x\right)\exp\left(\frac{-j2\pi x x'_{\mathrm{im}}}{\lambda d_{ex}}\right)dx, \tag{3.4}$$

where d_{ex} is the distance from the exit pupil to the image plane, A is a constant and λ is the wavelength of the light. p^{ex} is the exit pupil and for the 1-D analysis presented here is defined as

$$p_a(x) = \begin{cases} 1, & \text{if } |x| < a \\ 0, & \text{otherwise,} \end{cases} \tag{3.5}$$

where a is the aperture radius and where for the 4-f imaging system depicted in Fig. 3.1, $d_{ex} = f_2$.

And so to summarize what we have looked at so far, we note several things:

- System magnification, exit, entrance and limiting apertures are determined using geometrical optics,
- Although an imaging system may consist of several lens and apertures, diffraction effects are usually associated only with that aperture that most severely restricts the passage of light through the system. All other apertures in the system are assumed to be infinite in extent,
- The geometrical image is first calculated and then the effects of diffraction arise from a convolution of this image with the PSF of the system.

3.1 Point spread function analysis

It now remains to derive the PSF which we defined in Eq. (3.4). Consider again Fig. 3.1, where we assume a unit magnification system, hence $f_1 = f_2 = f$. There are several ways to approach this problem, i.e. by tracking the propagation of a point source [defined as $PS_1 = \delta(x - \xi)$.] through the system. However here we will use the equations we have presented thus far to determine the PSF. Looking again at Eq. (3.4), we see that both d_{ex} and the exit pupil extent a_{ex} need to be determined. This can be achieved using ray tracing techniques, see Appendix and we find that $d_{ex} = f$ and $a_{ex} = a$. Inserting these results into Eq. (3.4) and integrating we arrive at the following expression for the PSF

$$\begin{aligned} h\left(x'_{\text{im}}\right) &= \frac{A}{\sqrt{\lambda f}} \int_{-a}^{a} \exp\left(\frac{-j2\pi x x'_{\text{im}}}{\lambda f}\right) dx, \\ &= \frac{2aA}{\sqrt{\lambda f}} \text{sinc}\left(\frac{2\pi a x_{\text{im}}}{\lambda f}\right), \end{aligned} \tag{3.6}$$

where we define a sinc as

$$\mathrm{sinc}(z) = \frac{\sin(z)}{z}. \tag{3.7}$$

In Fig. 3.2 we present a plot of the intensity of such a distribution for the following values: $\lambda = 500$ nm, $a = 2$ mm, $f = 10$ cm and $A = 1$.

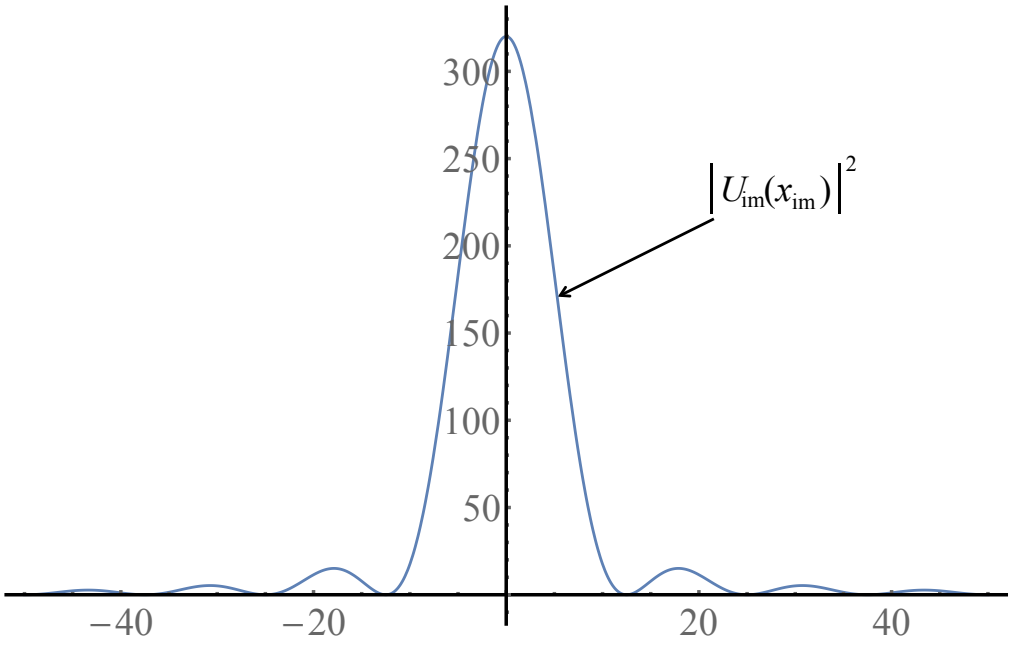

Figure 3.2 – A typical sinc function distribution.

3.2 Rayleigh's approach to resolution

Suppose we now wish to examine the image distribution when the input field is given by

$$\delta(x-d)+\delta(x+d)\exp(j\phi), \tag{3.8}$$

where each δ function in Eq. (3.8) represents a contribution from a point source, while $2d$ is the physical distance between the point sources. We can find the image distribution by convolving Eq. (3.8) with the PSF, i.e. Eq. (3.6), and in Fig. 3.3 we present a plot of such a situation, with the same values as before but now setting $d = 4RD/2 = \frac{\lambda f}{4a}$, where $RD = \frac{\lambda f}{2a}$. RD is what we refer to as the Rayleigh distance. We can clearly

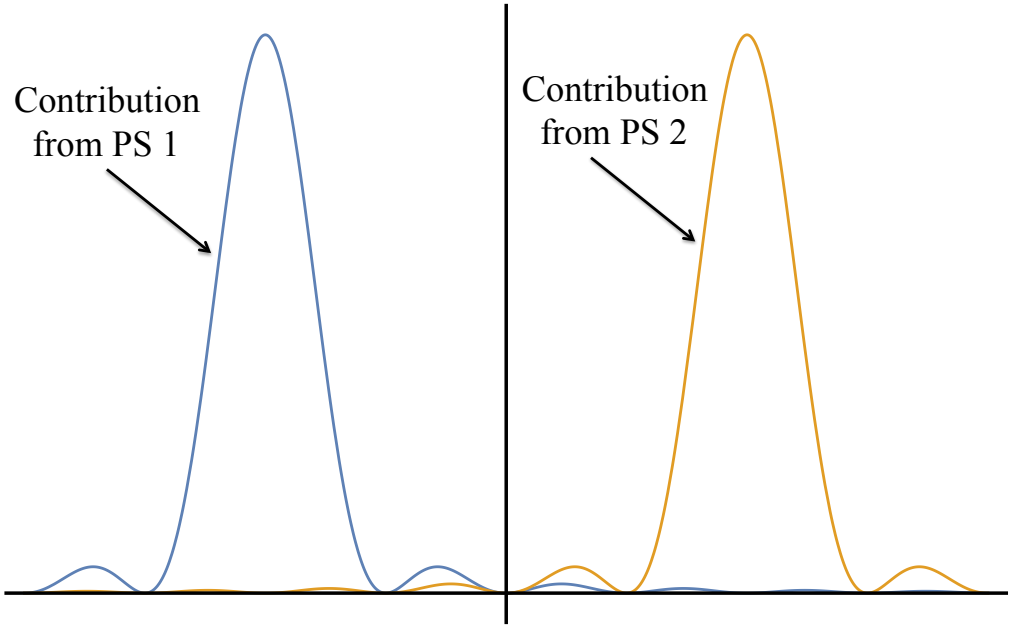

Figure 3.3 – Two well separated point spread functions.

see two sinc functions that are separated from each other. From this picture we can conclude that the distribution arises from two point souces located in the object plane. A question does arises however, namely what is the smallest value of d where we can still determine that there are in fact two separate sinc functions? This was a question that Lord Rayleigh tried to address. He was mostly concerned with incoherent light and suggested that this distance d be defined such that a small dip between the peaks be discernible in the image plane. He identified this exact point as being the case when

the maximum of one sinc function lies over the minimum of the neighbouring function as depicted by the thick grey line in Fig. 3.4. In Fig. 3.4, we again see the individual

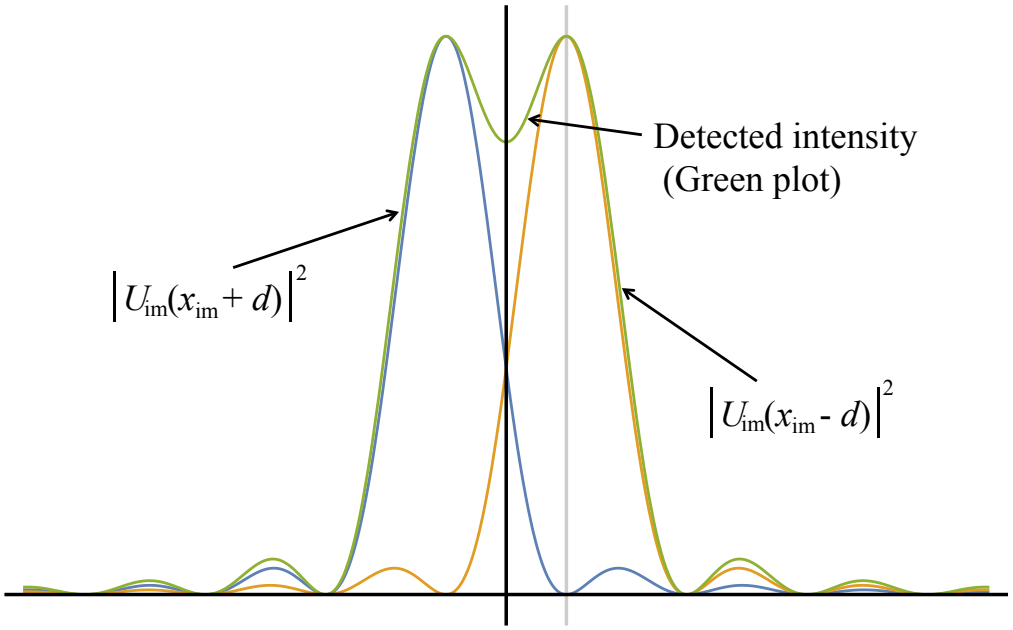

Figure 3.4 – Rayleigh resolved point spread functions.

contributions from each point source plotted separately, these are the blue and orange distributions, while the actual measured intensity will be the contribution from both point sources (which for the incoherent case) and is shown by the green distribution. We can see that two peaks are still clearly discernible and the two point sources are said to be Rayleigh resolved.

Before we move onto incoherent light sources though let us consider one more example of coherent imaging. In Fig. 3.5 we present a plot of the image plane distributions that arise from Eq. (3.8) for three different values of phase difference ϕ. Examining Fig. 3.5 we could identify three separate regimes in the three separate distributions that are plotted. Here for example the blue plot would correspond to case where the point sources are not Rayleigh resolved; the orange plot would be exactly Rayleigh resolved (compare with Fig. 3.4, while the green plot indicates that the point sources are well separated in a Rayleigh sense.

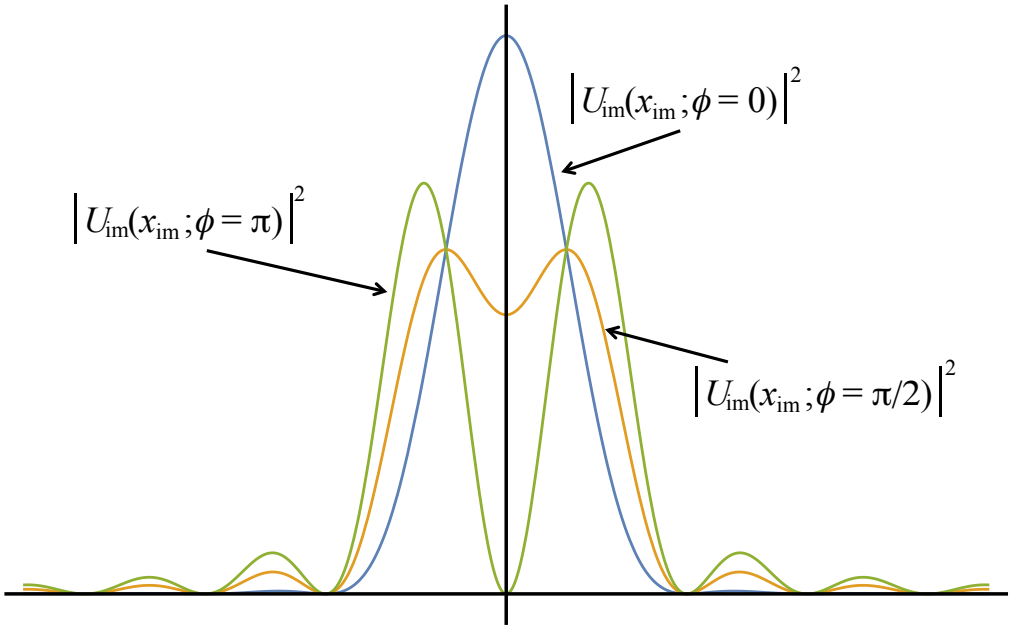

Figure 3.5 – Here we have three different distributions when $2d = RD$. When we change the relative phase, ϕ. Here when $\phi = 0$, we cannot resolve the two sinc functions, when $\phi = \pi/2$.

We conclude this section by noting that the Rayleigh resolution limit does not tell the full story for coherent imaging systems. Simply by varying the relative phases between a simple input function, Eq. (3.8), we change the apparent resolution of our optical system. One can imagine that for more complex input functions where the relative phases from different contributing point sources varies will also modify the intensity in the image plane. This effect is also present in coherent holographic imaging systems, see Ref. [13, 14]. In the next section we will try to examine what happens if we allow the phase of different contributing point sources to vary as a function of time and how this effects the final intensity distribution.

3.3 Spatial coherence

In the last section we saw that the intensity distribution in the image plane depends not only on the amplitude of the object field but also on the relative phases of the contributing point sources. In particular for the case of a two point source input function we saw in Fig. 3.5 that by changing the relative phase between two point sources

separated by a distance RD from 0 to π radically changed the intensity distribution. Suppose however that the relative phase between the two point sources were to change over time, what would an intensity detector measure? If the frame rate of the CCD array were sufficiently quick it would be possible to track the changes in the intensity distribution as they happen, as for example, in this holographic imaging system [32]. In reality however these phase changes are phenomenally rapid and well beyond the detection time of a CCD array. Hence we must develop a theoretical means of describing what the CCD would measure if a series of different intensity distributions are averaged over time [7]. In what follows we assume that the light source is quasi-monochromatic and ignore temporal coherence effects [7]. This is what we express mathematically in Eq. (3.9)

$$I = \langle U_{\text{im}}\left(x_{\text{im}}, t\right) U^{*}_{\text{im}}\left(x_{\text{im}}, t\right)\rangle_{t}, \tag{3.9}$$

where we have specifically included a time dependance t in our expression for the complex amplitude in $U_{\text{im}}\left(x_{\text{im}}, t\right)$. The '*' superscript indicates a complex conjugate operation and the angled brackets indicate that we are measuring a time average of the intensity. Substituting Eq. (3.3) into Eq. (3.9) and interchanging the order of the time averaging and the integration we arrive at the following result:

$$I = \int_{-\infty}^{\infty}\int_{-\infty}^{\infty} h\left(x_{\text{im}} - \zeta\right) h^{*}\left(x_{\text{im}} - \overline{\zeta}\right) J_{g}\left(\zeta, \overline{\zeta}\right) d\zeta d\overline{\zeta}, \tag{3.10}$$

where J_g is known as the mutual intensity function and is a measure of the spatial coherence of the light at the two object points.

$$J_{g}\left(\zeta, \overline{\zeta}\right) = \langle U_{G}\left(\zeta\right) U^{*}_{G}\left(\overline{\zeta}\right)\rangle_{t}, \tag{3.11}$$

This is the function we use to define what is meant by spatial coherence.

Spatially coherent light

For the case of spatially coherent light, all of the contributing point sources in the object plane vary in unison over time which we may write in the following manner

$$U_{g}\left(\zeta, t\right) = U_{g}\left(\zeta\right) \frac{U_{g}\left(0, t\right)}{\langle |U_{g}\left(\zeta, t\right)|^{2}\rangle^{\frac{1}{2}}}, \tag{3.12}$$

Here we have set the point source at the origin to be the reference phase. From Eq. (3.10) and Eq. (3.12) we see that as one moves along the object field the phase at each point will vary by some complex constant, however these values are all referenced to

the phase at the origin and hence

$$J_g\left(\zeta,\overline{\zeta}\right) = U_g\left(\zeta\right)U_g^*\left(\overline{\zeta}\right), \tag{3.13}$$

which when substituted back into Eq. (3.10) gives the following result

$$I = \left|\int_{-\infty}^{\infty} h\left(x'_{\text{im}}-\zeta\right)U_g\left(\zeta\right)d\zeta\right|^2 \tag{3.14}$$

Hence for spatially coherent light, the intensity distribution is found to be described by an amplitude convolution operation.

Spatially incoherent light

In this case we assume that the time varying phase at each point in the object plane is statistically unrelated to its neighbours. In this instance the mutual intensity function is written as

$$\begin{aligned} J_g\left(\zeta,\overline{\zeta}\right) &= \langle U_G\left(\zeta\right)U_G^*\left(\overline{\zeta}\right), \\ &= \kappa I_g(\zeta)\delta(\zeta-\overline{\zeta}), \end{aligned} \tag{3.15}$$

which when substituted into Eq. (3.10) gives the following result:

$$I = \kappa\int_{-\infty}^{\infty}\left|h\left(x'_{\text{im}}-\zeta\right)\right|^2 I_g\left(\zeta\right)d\zeta. \tag{3.16}$$

From the last result we see that the intensity distribution for spatially incoherent light is linear in intensity rather than in amplitude as in the coherent case.

Spatial frequency response

From Eq.'s (3.14) and (3.16), we expect that the spatial frequency response of both types of systems will be different, despite the fact that the same optical components are used in each system. The different system performance arises solely from the different illumination conditions or light sources. In order to get an idea of the spatial frequency response of a coherent system we need to look at the Fourier transform of the PSF, i.e. the amplitude transfer function

$$\begin{aligned} H(f_x) &= \int_{-\infty}^{\infty} h(x)\exp\left(-j2\pi f_x x\right)dx \\ &= p_{f_{max}}(f_x), \end{aligned} \tag{3.17}$$

where $f_{max} = a/(\lambda f)$. Hence the passband for the 4-f imaging system is simply a rectangular filter that will pass all frequencies up to and including f_{max}.

We now look at the spatial frequency response of the incoherent imaging system. Again we note that in the incoherent case we convolve the intensity predicted by geometrical optics with the magnitude squared of the PSF for the system. We can write the incoherent PSF, $|h(x)|^2$ as $h(x)h^*(x)$, and hence (employing the Fourier convolution theorem) we find the spatial frequency response is given by

$$\begin{aligned} OTF(f_x) &= \frac{\int_{-\infty}^{\infty} |h(x)|^2 \exp\left(-j2\pi f_x x\right) dx}{\int_{-\infty}^{\infty} |h(x)|^2 dx} \\ &= \frac{H(f_x) \star H^*(f_x)}{\int_{-\infty}^{\infty} |h(x)|^2 dx}, \end{aligned} \tag{3.18}$$

where $\star$ indicates the convolution operation. The denominator in Eq. (3.18) is a normalizing factor such that the maximum value of the OTF is unity. Hence for an incoherent system the spatial frequency passband is a auto-convolution of the coherent spatial frequency response. A comparative figure of the two spatial frequency responses is presented in Fig. 3.6. The frequency response of the incoherent system is higher than that of the coherent system, however higher spatial frequencies are attenuated more strongly than lower frequencies. The abrupt nature or sharp edge of the coherent response tends to produce 'ringing' in the images as can be seen in Fig. 3.7, where we show how a coherent and an incoherent optical system will image a sharp edge. The oscillatory response of the coherent system produces strong ringing effects, in contrast to the incoherent imaging.

3.4 Laser based projection systems.

In the previous sections we have examined the 4-f imaging system for both coherent and incoherent light sources. In this section we turn our attention to an important commercial imaging application. There is significant consumer demand for bright uniform projection systems. A major issue with such systems is an appropriate light source. While a xenon arc lamp sources produce high quality projected images and are a bright incoherent source, they are also costly, inefficient and have short life spans. Using coherent laser light would be an ideal alternative however the resulting projected images suffer from a high contrast speckle noise that is unacceptable. This speckle contrast is a feature of coherent imaging systems and some relevant theory has been discussed here [1, 22–27].

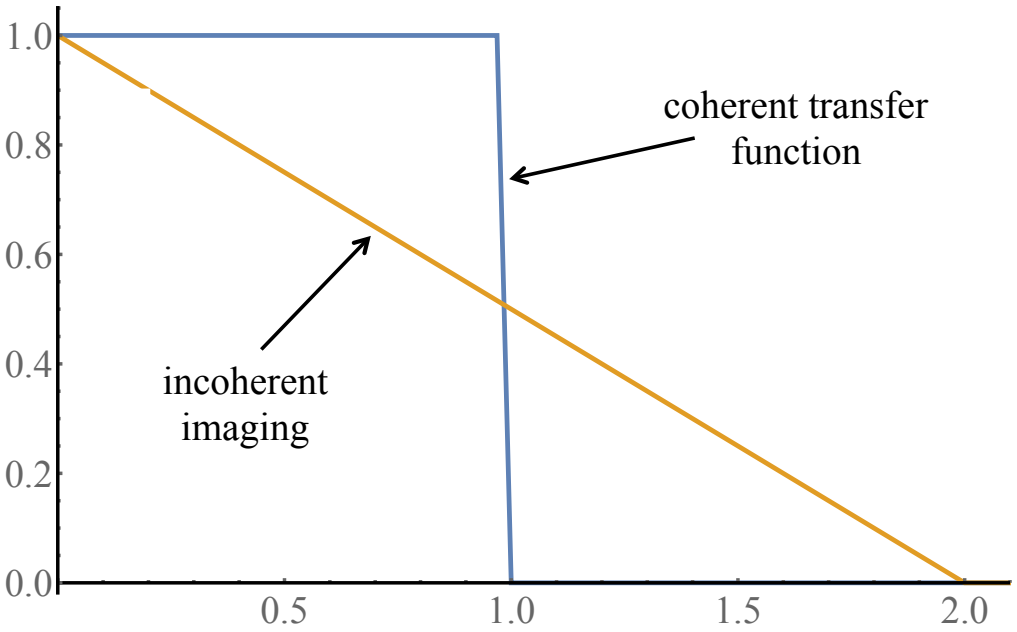

Figure 3.6 – Comparison of the normalized spatial frequency response of coherent and incoherent systems. The spatial frequency scale is normalized to f_{max}.

Background

There are many different techniques for reducing speckle contrast such as varying the wavelength, changing the polarization, and placing moving diffusers in the optical system. All of these approaches rely on the following principle: A series of projected coherent images of the same desired scene are produced; each with a statistically independent speckle noise, which when added together on an intensity basis, averages out the speckle noise. If a sequence of these, individually noisy images, are sequentially projected within the integration time of the human eye, then the viewer sees a significant reduction in speckle noise. This phenomenon has been analyzed here [25, 41], deriving a formula for the expected reduction speckle noise, see Eq. (3.19), for over designed projector imaging system. Theoretical treatments of this problem tend to be detailed and complex. Here however we wish to we address the same problem and to provide a more intuitive physical model that captures the essence of the more complex treatment. It is hoped that this relatively simple treatment will provide another means of thinking about this important imaging problem.

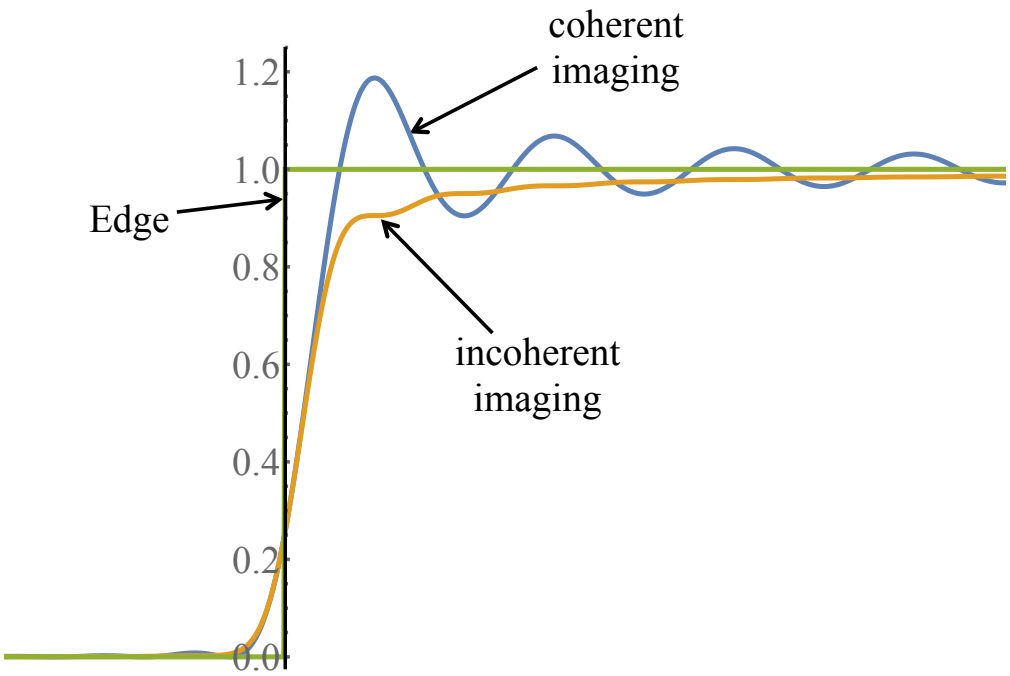

Figure 3.7 – Comparison of coherent and incoherent systems, imaging a straight edge.

In Fig. 3.8, we sketch the nature of the optical system we are analyzing. It consists of two back-to-back imaging systems, each modeled as a linear shift invariant system where all diffraction effects arise due to a limiting aperture situated in the Fourier plane. This type of model is supposed to describe what happens in a regular cinema. There high quality projection optics are used to image a scene from a film onto the cinema projection screen. Then a viewer sitting in the audience re-images this scene onto the back of their retina. Hence we have two back-to-back imaging systems. Each imaging system has a PSF associated with it, which we refer to as PSF_{EYE} and PSF_{PO}. For simplicity, we model the PSF_{EYE} as a rectangular function, see Fig. 3.9. The imaging performance of the projector optics is assumed to be significantly better than our eye. Here we consider a single wavelength (color) for simplicity and choose to use a Digital Micro mirror Device (DMD) as a spatial light modulator located in the input plane of the projector imaging system. The scene, to be observed, is loaded electronically onto the DMD and projected onto the viewing screen. The eye then re-images this picture onto the retina, however the secondary imaging operation introduces noise and the final image of the scene that is incident on the back of the eye will now be corrupted with speckle.

We assume that the DMD operates in amplitude mode and a diffuser, placed just behind it, introduces a random phase value at each DMD pixel. These random phase values can be varied rapidly, by moving the diffuser relative to the DMD. For each new position of the diffuser, the scene loaded onto the DMD is imaged onto the eye's retina however with a new and statistically independent speckle noise. These successive noisy images are integrated on an intensity basis by the eye and in this manner the perceived speckle noise decreases significantly according to the following formula [41]:

$$C = \sqrt{\frac{M + K - 1}{MK}} \tag{3.19}$$

where K is defined in Fig. 3.9 and M refers to the number of times the diffuser was moved to a new position within the integrating time of the eye. When M is very large then Eq. (3.19) reduces to the following

$$C = \sqrt{\frac{1}{K}} \tag{3.20}$$

Analysis

Here we arrive at a similar theoretical result using a different more intuitive approach. We make the following assumptions:

1. The DMD operates as an amplitude only device whose values vary from zero to unity in a continuous fashion. In practice this may be achieved using a duty-cycle approach.

2. For a given position of the diffuser a constant but random phase value modulates each pixel of the DMD.

3. The imaging system that is the projector optics, passes all the light and perfectly images the DMD scene onto the Viewing Screen (VS). The VS is assumed to be optically rough and to consist of many small "correlation cells". These "correlation cells" are spatial regions where the phase is constant. Each correlation cell has a uniform random phase associated with it.

4. The eye aperture spatial filters light in a Fourier plane, see Fig. 3.8. Another simplification we make is to assume that the PSF_{EYE} is described with a rectangular function such as Eq. (3.5) rather than the usual sinc function, see Eq. (3.6). Finally, we note again that $PSF_{\mathrm{EYE}} > PSF_{\mathrm{PO}}$, see Fig. 3.9.

Having made these assumptions, the complex amplitude at an image point, P, in the retina will consist of contributions from K different areas over the viewing or projection

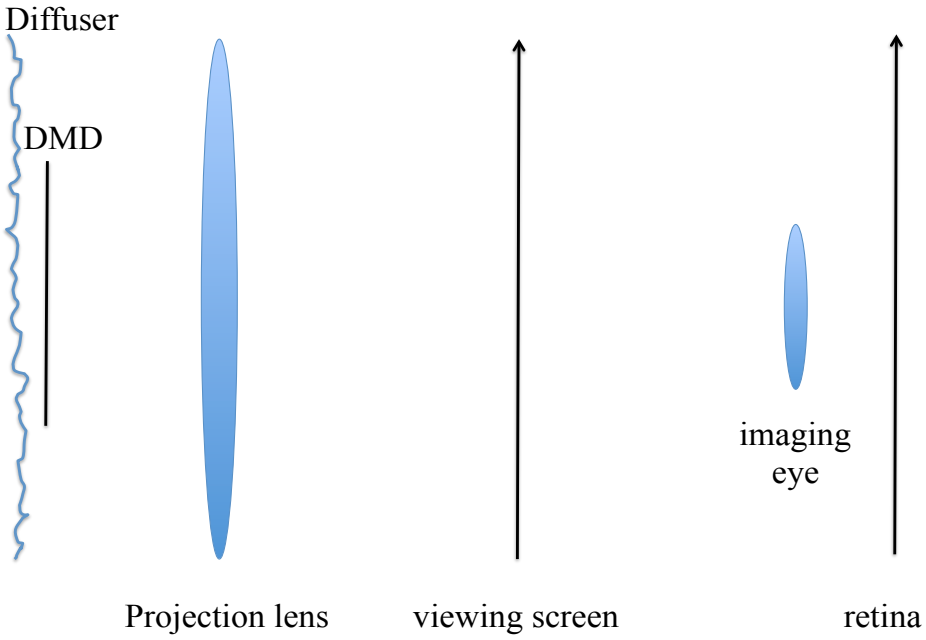

Figure 3.8 – Schematic of the optical system we are considering, it consists of two imaging systems: the first is the projection optics while the second models the imaging behaviour of the eye as a 4-f imaging system.

screen. To further simplify the analysis we also assume that each one of these areas corresponds to the projected area of a DMD pixel. Hence that the PSF_{PO} has been chosen so that it matches the size of each DMD pixel. This assumption is not always the case, often for example the PSF_{PO} is smaller than that of a DMD pixel. This however does not effect the analysis presented here, as it only acts to increase the effective number for K in Fig. 3.9. Hence we write:

$$U_m(P) = \sum_{k=1}^{K} Pixel_k, \tag{3.21}$$

for a particular diffuser position, denoted m. It follows from Assumptions (1)-(3) above, that each projected DMD pixel, i.e. $Pixel_k$, will have the correct amplitude (that corresponding to the desired scene A_{DR}) and a random phase, $\exp(j\phi_{km})$, value due to the diffuser. Thus

$$Pixel_k = A_{\mathrm{DR}} \exp(j\phi_{km}) \sum_{r=1}^{R} \exp(j\theta_{kr}), \tag{3.22}$$

where θ_{kr} is the 'r' phase correlation cell due to the rough surface of the viewing screen. There are R such cells per $Pixel_k$. Assuming that R is large and that θ_{kr} is uniformly distributed between 0 and 2π we can rewrite Eq. (3.22) as

$$Pixel_k = A_{\mathrm{DR}} \exp\left(j\phi_{km}\right) \Theta_k. \tag{3.23}$$

The random variable Θ_k is assumed to follow a normal distribution. For simplicity

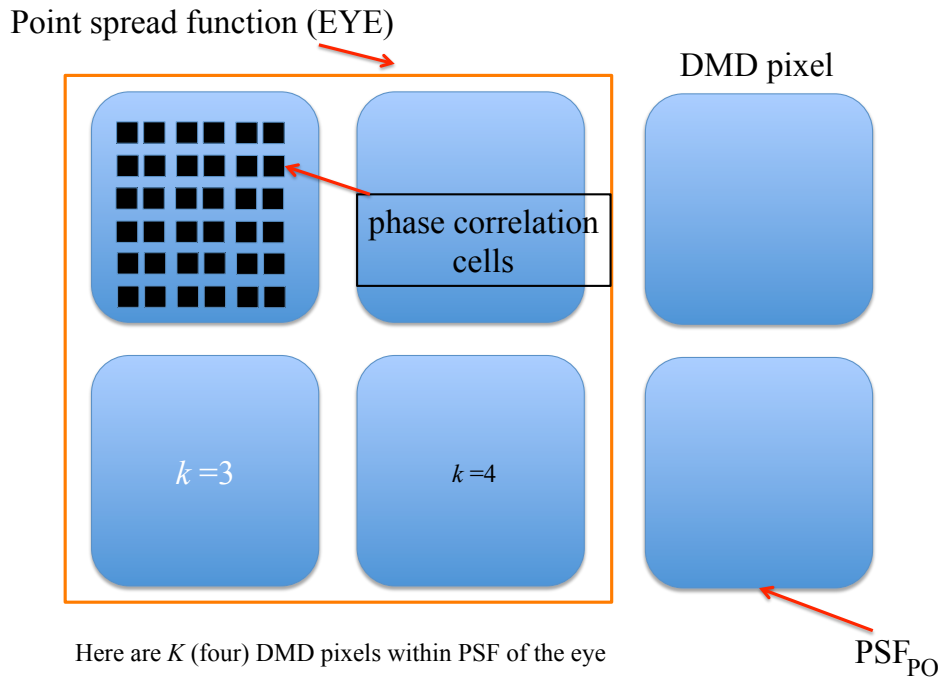

Figure 3.9 – Depiction of image projected onto VS. DMD pixel refers to a projected image of an individual pixel on the DMD. Black squares refer to "correlation cells" which are iso-planatic regions of constant phase on the surface of viewing screen.

we set A_{DR} to a constant over each k contributing pixel area; then the intensity at a location P on the retina is given by

$$U_m(P)U_m^*(P) = S_1 + S_2 \tag{3.24}$$

where as usual the '*' operator takes the conjugate of the complex function and where

$$S_1 = A_{\mathrm{DR}}\left(Y_1 + Y_2 + ... + Y_k\right) \tag{3.25}$$

and

$$S_1 = A_{\mathrm{DR}} \left(2\sqrt{Y_1 Y_2} \cos\left[Q_{12m}\right) + 2\sqrt{Y_1 Y_k} \cos\left(Q_{1km}\right) + 2\sqrt{Y_2 Y_k} \cos\left(Q_{2km}\right) + ... \right] \quad (3.26)$$

where $Y_k = \Theta_k \Theta_k^*$ is a random variable and where $Q_{1km} = \phi_{1m} - \phi_{km} - (\mathrm{Arg}\left\{\Theta_k\right\} - \mathrm{Arg}\left\{\Theta_1\right\}$. Eq. (3.21) to Eq. (3.26) are used to determine the intensity at P on the retina for a particular location of the diffuser. We are interested in the time-averaged intensity over a large number M of diffuser positions. For each diffuser position we get a new and random realization of the S_2 contribution above in Eq. (3.24), which will time-average to zero. This significantly reduces the speckle contrast.

The remaining S_1 term depends on the statistics of the surface roughness of the viewing screen. Similar to other analysis [25, 41] there is a term that does become smaller due to temporal averaging and will act as an asymptotic limit to the reduction in speckle contrast.

Chapter 4

Digital holographic imaging.

4.1 Introduction

In previous chapters we have discussed the propagation of an optical wavefield using the Fresnel transform. We then examined how we could extend this treatment of optical wave propagation so that optical elements such as lenses and soft Gaussian apertures could also be considered within a wave optics paradigm. We examined a special optical system for intensity imaging known as a 4-f imaging system in terms of its point spread function for both coherent and incoherent light sources. And we addressed how a variety of optical systems could be simulated numerically. In this chapter we bring these different elements together and examine a new approach to optical imaging, namely holography. Holography has been around since the late forties being introduced by that famous scientist Gabor, as means of improving the imaging performance of electron microscopes. He also indicated that this approach could be implemented electronically, which has today become a very significant research topic spanning microscopic imaging [8, 10, 13, 14, 16, 17, 20], speckle based metrology [1, 3] among other topics.

We observe that optical sensors are sensitive to the intensity of the optical wavefield that is incident upon them. A CCD array can be used in an imaging configuration if a lens is to map an object plane to the plane where the CCD array is situated. In this circumstance, we can 'see' a scene on a television display. Suppose however if we could somehow recover not only the intensity of the optical wavefield but also its phase. This was the contribution of Gabor who devised a mechanism - which he termed holography - whereby we could indirectly estimate the phase of the wavefield by interference. Once we can recover the phase as well as the intensity we can use propagation algorithms to

reconstruct an image numerically and without a lens.

Hence digital holography is an optical imaging technique which is based firstly on interference [10] and then secondly, the processing of the resulting digital interferogram. The input wave that we are interested in recovering is allowed to propagate to a plane where a digital sensor is located. Suitable sensors are based on either CMOS or CCD technology (we will use CCD exclusively in this text) and consist of an array of uniform pixels of finite extent. At the CCD plane the scattered object wave overlaps and interferes with a known reference wave, which usually is either a plane or spherical wave, and the resulting intensity distribution is recorded. In Fig. 4.1 we present an optical system that can be used for such a purpose, it includes two beam-splitters one of which is a polarized beam splitter and two $\lambda/2$ waveplates. Coherent mono-chromatic light emerges from the laser and is divided into two parts by by the first beam-splitter. One part is deflected along a particular path known as the reference arm, whereupon it is reflected from a piezo-mounted mirror to be formed into either a spherical or plane wave. The other optical path is known as the object arm where the beam is expanded and then illuminates (as a plane wave) the sample in the object plane. As usual the field immediately after the sample is defined as $U(X)$. The second beam splitter then re-combines the light from with reference arm with the light that has been scattered from the sample, whereupon the resulting intensity distribution is recorded by the CCD array. The waveplates serve a practical purpose allowing the experimenter to control a relative strength of the light in the reference and object arms. The intensity distribution incident on the sensor array can be expressed as

$$H\left(x\right) = I_z\left(x\right) + I_r\left(x\right) + c\left(x\right) + c^*\left(x\right), \tag{4.1}$$

where $I_z\left(x\right)$ and $I_r\left(x\right)$, are the intensities of the object and reference fields respectively, and where $c(x) = u_z\left(x\right) u_r^*\left(x\right)$. This term $c(x)$ is all important. It contains the complex amplitude of the scattered field $u_z(x)$ that we wish to recover. We shall now examine how this might be done. We note that the 3rd and 4th terms in Eq. (4.1), are known as the real and twin image terms respectively.

It is very important to notice another significant benefit of a holographic imaging system. Unlike traditional lens based imaging systems we actually recover not just the intensity distribution but also the phase! This phase information is extremely important in many different metrology situations, allows one to make direct measurements of the refractive indices of materials and is particularly useful in biology. It is of historic interest to remember that while optical engineers were struggling to produce optical

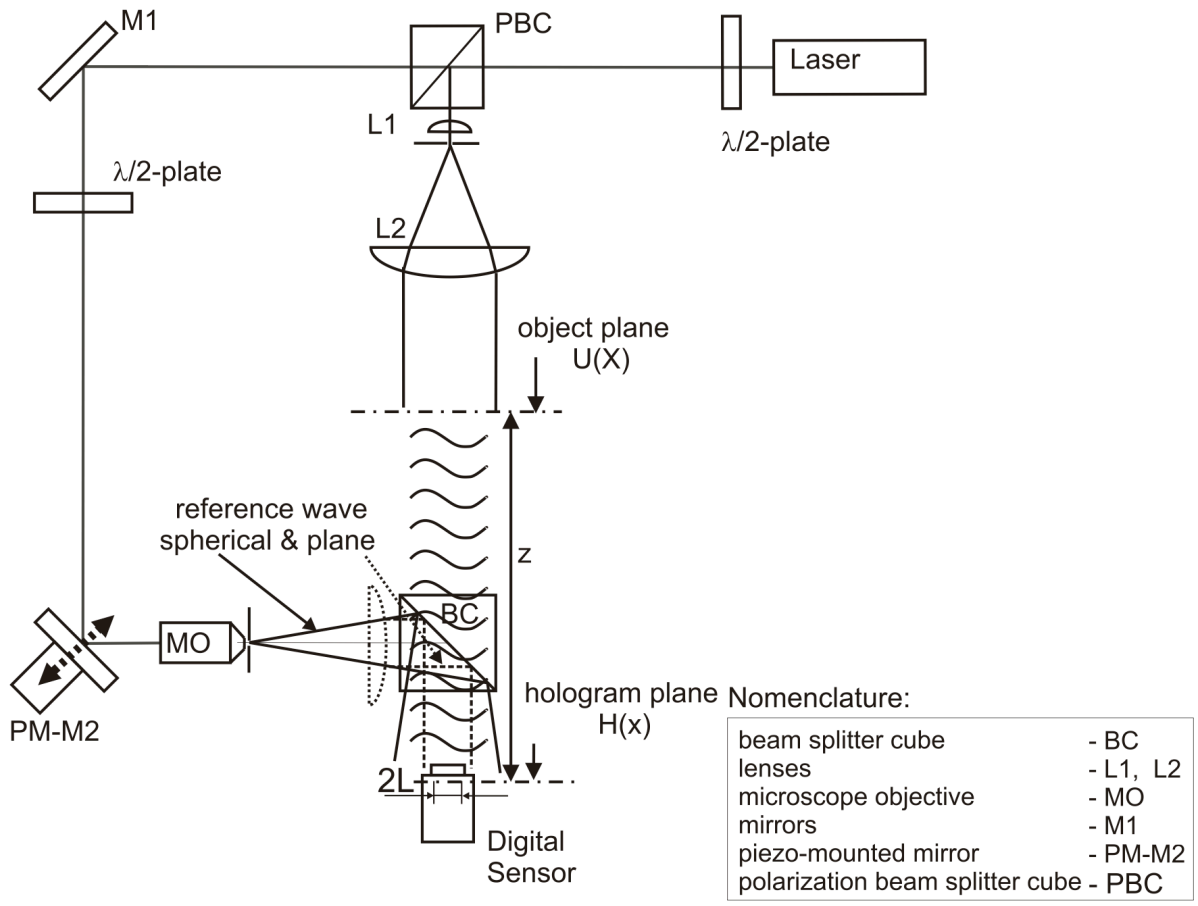

Figure 4.1 – Schematic depicting the holographic systems we discuss in the manuscript. The reference wave can be changed from a spherical to a plane wave by inserting a lens at the appropriate location in the reference arm, taken from Ref. [10].

microscopes with better and more accurate imaging performances, biologists were continually defocusing their microscopes so that they could 'see' structure in the purely phase objects - i.e. cells they were interested in. A pure phase object is not visibly when we observe only the intensity of the light in an imaging plane. To 'see' the cell structure means that the phase distribution must cause the light to diffract slightly so that it forms intensity variations. Hence the reason for de-focusing the microscope.

If this system is to achieve a good imaging performance, then $c(x)$, must be separated from the other terms, which otherwise act to degrade the quality of the reconstructed image. There are two types of reference waves that we shall consider in this chapter a spherical wave and a plane wave. When a spherical wave is used the system is referred to as an inline Fourier system for reasons we shall later understand. In this case the

reference field is given by

$$u_r(x) = \exp\left(\frac{j\pi x^2}{\lambda z_r}\right), \tag{4.2}$$

where z_r is the distance from the spherical wave point source to the sensor plane. When we examine a Fresnel system, we replace the spherical reference source, with a normally incident plane wave, i.e., we set $u_r(x) = 1$. Eq. (4.1) can also be rewritten as

$$H(x) = I_z(x) + I_r(x) + \Gamma(x), \tag{4.3}$$

where we refer to the third term, as the interference term, which is defined as, $\Gamma(x) = 2|u_z(x)||u_r^*(x)|\cos(\phi_z - \phi_r)$. The expression ϕ_z and ϕ_r refer to the phase distributions of the object and reference waves respectively, and vary as function of position, x.

We note that the scattered object field, $u_z(x)$ from this interference equation is related to the object field $U(X)$ through a Fresnel transform as follows:

$$\begin{aligned} u_z(x) &= \mathrm{FST}_z\{U(X)\}(x) \\ &= \frac{\exp(j2\pi z/\lambda)}{\sqrt{j\lambda z}} \int_{-\infty}^{\infty} U(X) \exp\left[\frac{j\pi}{\lambda z}(x-X)^2\right] dX, \end{aligned} \tag{4.4}$$

For notational convenience, we drop the leading constant complex term, $\exp(j2\pi z/\lambda)/\sqrt{j\lambda z}$, for the rest of the chapter. For our purposes it will be helpful to note that the Fresnel transform can also be expressed as,

$$u_z(x) = U(x) \otimes \exp\left(\frac{j\pi x^2}{\lambda z}\right), \tag{4.5}$$

and where we present the definition of the convolution operator as,

$$f(x) \otimes g(x) \equiv \int_{-\infty}^{\infty} f(X) g(x-X) dX. \tag{4.6}$$

We will again make use of the Fourier transform operator which we present here again for the readers convenience,

$$\begin{aligned} \tilde{v}(\omega) &= \psi\{v(x)\}(\omega) \\ &= \int_{-\infty}^{\infty} v(x) \exp(-j2\pi\omega x)\, dx, \end{aligned} \tag{4.7}$$

and the inverse operation as,

$$\begin{aligned} v(x) &= \psi^{-1}\left\{\tilde{v}(\omega)\right\}(x) \\ &= \int_{-\infty}^{\infty} v(\omega)\exp\left(+j2\pi\omega x\right)d\omega. \end{aligned} \tag{4.8}$$

We also note the following property of the Fourier transform,

$$\psi\left\{f(x)\otimes g(x)\right\}(\omega) = \psi\left\{f(x)\right\}(\omega)\cdot\psi\left\{g(x)\right\}(\omega). \tag{4.9}$$

The continuous intensity distribution, given by Eq. (4.1) or Eq. (4.3), is recorded by a CCD sensor and a 2-D array of positive numbers is returned to the user, see Fig. 4.1. This process of digitizing the continuous intensity distribution acts to limit the amount of information we can recover about the $c(x)$ signal in 3 separate ways:

1. The finite extent of the sensor array means that only the portion of $c(x)$ that lies within the sensor's extent is recorded,
2. The finite size of the pixels average the light intensity incident upon them,
3. The resulting distribution is multiplied by a Dirac delta comb that defines the distance between the centers of adjacent pixels [13].

Since the model we use to describe the operation of the CCD sensor is linear, see Eq. (4.1), we may consider the effect of these filtering and sampling operations on each term in Eq. (4.1) or Eq. (4.3), separately. We now address the problem of how to separate $c(x)$ from the other terms in Eq. (4.1), which can be achieved with a number of techniques. Here however we use Phase Shifting Interferometry (PSI). We refer the reader again to the piezo-mounted mirror in Fig. 4.1, which is a precision motor stage that can move the mirror through extremely precise distance on the order of $\lambda/10$. It is possible to recover separate $c(x)$ by captured a number of holograms where the phase in the reference arm is shifted by precise and known amounts in between captures. Here is the procedure then for isolating $c(x)$.

- We record a hologram, denoted H_1, then the mirror is shifted through a phase angle of $\pi/2$.
- A second hologram, H_2 is then recorded where $\Gamma(x) = 2|u_z(x)||u_r^*(x)|\cos\left(\phi_z - \phi_r + \pi/2\right)$
- We continue a record two further holograms, H_3 and H_4, that are phase shifted by a further $\pi/2$ before each new capture.

The $c(x)$ term is now given by

$$c(x) \quad = \quad \frac{1}{4}\left[(H_3 - H_1) + j\,(H_4 - H_2)\right], \tag{4.10}$$

and in this manner we recover a discrete array, $\overline{\mathrm{C}}$, of discrete complex values that are related to $c(x)$ through the two filtering, [(1) and (2)], and sampling, (3), operations mentioned above. These discrete complex values can then be used to numerically calculate an approximation to the actual field, $U(X)$, in the input plane. We refer to this reconstructed field, which is a continuos complex function, as $R_N(X)$. The subscript 'N' indicates that this function has been numerically calculated from a finite set of complex values. In the case of Fresnel holography this numerical reconstruction operation is in fact an inverse Fresnel transform, which can be implemented using many different numerical approaches [11]. In principal then, we can calculate the value of $R_N(X)$, for any spatial location, X. In practice however efficient numerical algorithms, based on the Fast Fourier Transform (FFT), are used to implement these calculations. The nature of the FFT algorithm, imposes conditions, on the choice of X as was discussed Chapter 1.

We will now proceed in the following manner: We shall introduce a model that describes the operation of the digital sensor and we compare the relative performance of Fourier and Fresnel holographic imaging systems. We then examine the problem of recording Fourier and Fresnel holograms of a speckle field. We examine the characteristics of the interference term, $\Gamma(x)$, produced when $u_z(x)$ interferes with a plane and spherical reference wave, finding that statistical distribution of $\Gamma(x)$, can be varied by changing the sphericity of the reference wave. Finally we discuss some experimental results comparing the performance of a Fourier and a Fresnel system. For the Fresnel holographic system we demonstrate that as the width of the pixel increases, higher spatial frequencies become increasingly attenuated. In contrast in the Fourier system, we observe that the pixel size does not change the ability of the system to recover higher spatial frequencies.

4.2 Theoretical analysis of a holographic system.

We begin our analysis with a description of the sampling and filtering operations, that occur to the intensity distribution at the sensor plane and then proceed to relate the input wavefield, $U(X)$, to the reconstructed wavefield, $R_N(X)$, for the Fresnel and Fourier systems, respectively. The sensor array is modelled as

$$\overline{\mathrm{W}} = \beta\left[H\left(x\right) \otimes p_\gamma(x)\right] p_L(x)\delta_T(x), \tag{4.11}$$

where $\overline{\mathrm{W}}$ is an array of positive numbers that is returned by the sensor array and where β is an unimportant real scaling constant that accounts for features such as gain and exposure time [13, 17]. It is neglected from here on. The finite size of a sensor pixel is described with the following expression

$$p_\gamma(x) = \begin{cases} 1, & \text{when } |x| < \gamma \\ 0, & \text{otherwise,} \end{cases} \tag{4.12}$$

and in an identical manner we define the finite extent of the sensor array to be $2L$, using the function, $p_L(x)$. We now re-write the Dirac delta comb function, $\delta_T(x)$ is the following form

$$\delta_T = \sum_{n=-\infty}^{\infty} \delta(x - nT), \tag{4.13}$$

where, $\delta(x)$, is the Dirac delta function, the variable T is the sampling interval and n is an integer. We note that Eq. (4.13) can also be rewritten in the following form

$$\delta_T = \left(\frac{1}{T}\right) \sum_{n=-\infty}^{\infty} \exp\left(\frac{j2\pi nx}{T}\right), \tag{4.14}$$

Again for notational convenience we drop the leading, $1/T$ term, from here on. From Eq. (4.11), we see that the intensity distribution incident on the CCD, is first convolved with the pixel function, $p_\gamma(x)$, which acts to low pass filter $H(x)$. Secondly the extent of the resulting integrated intensity is limited by the sensor aperture, $p_L(x)$. Finally the Dirac delta comb acts to define the distance between the centers of adjacent pixels, and produces a set of replicas in the reconstruction domain that are separated from each other by a distance equal to $\lambda z/T$ [13, 17].

As the operations described in Eq. (4.11) are linear, we now examine how the filtering, [(1) and (2)] and the sampling operations, (3), affect each term in $H(x)$ individually. Hence, when we are interested in examining $c(x)$, we find that

$$\overline{\mathrm{C}} = \left[c\left(x\right) \otimes p_\gamma(x)\right] p_L(x)\delta_T(x), \tag{4.15}$$

where $\overline{\mathrm{C}}$ is an array of complex numbers that we can use to numerically reconstruct the input wavefield.

Let us concentrate on the filtering role of the CCD pixel and refer the reader to Ref. [13] and Ref. [17] for a more comprehensive analysis. So then to simplify the

analysis, we allow the extent of the CCD sensor go to infinity, and neglect the $p_L(x)$ function. Thus the simplified model is used in the following sub-sections is given by

$$\overline{\mathrm{C}} = \left[c\left(x\right) \otimes p_\gamma(x)\right] \delta_T(x). \tag{4.16}$$

Fresnel case.

For the Fresnel system, then $u_r(x) = 1$, and so $c(x)$ becomes $u_z(x)$ and then the reconstructed field can be calculated using the following expression:

$$\begin{aligned} R_{N\chi}(X) &= \mathrm{FST}_z \left\{ u_z\left(x\right) \otimes p_\gamma(x) \sum_{n=-\infty}^{\infty} \exp\left(\frac{j2\pi nx}{T}\right) \right\} (X) \\ &= \sum_{n=-\infty}^{\infty} \left[\mathrm{FST}_z \left\{ u_z\left(x\right) \otimes p_\gamma(x) \exp\left(\frac{j2\pi nx}{T}\right) \right\} (X) \right], \end{aligned} \tag{4.17}$$

where we perform an inverse Fresnel transform numerically, on the data set $\overline{\mathrm{C}}$. Setting $n = 0$ in Eq. (4.17), and making use of Eq. (4.5), the Right Hand Side (RHS), can be rewritten as

$$\begin{aligned} & u_z(x) \otimes p_\gamma(x) \otimes \exp\left(\frac{-j\pi x^2}{\lambda z}\right) \\ & U(X) \otimes p_\gamma(X). \end{aligned} \tag{4.18}$$

Now we make use of the modulation property of the Fresnel transform, [11]. If

$$f_z(y) = \mathrm{FST}_z \left\{ f(y') \right\} (y), \tag{4.19}$$

then

$$\mathrm{FST}_z \left\{ f(y') \exp\left(j2\pi\sigma y'\right) \right\} (y) = f_z\left(y - \lambda z\sigma\right) \exp\left(j2\pi\sigma y\right) \exp\left(-j\pi\lambda z\sigma^2\right). \tag{4.20}$$

Combining Eq. (4.17) and Eq. (4.21), (note: $\sigma \rightarrow n/T$), we arrive at the final result

$$R_{N\chi}(X) = \sum_{n=-\infty}^{\infty} \exp\left(\frac{-j\pi\lambda z n^2}{T^2}\right) \exp\left(\frac{j2\pi nX}{T}\right) U\left(X - \frac{n\lambda z}{T}\right) \otimes p_\gamma\left(X - \frac{n\lambda z}{T}\right). \tag{4.21}$$

From this result we see that the central order reconstructed input field, $(n = 0)$, is the input field convolved with the pixel function, which acts to reduce the higher spatial frequency content in the signal. Higher order replicas, i.e. when $n \neq 0$, have constant and linear phase factors associated with them.

Fourier case.

Here we present the complementary analysis for a Fourier system. We first take note of the following Fourier transform pair: $p_\gamma(x)$ and its counterpart

$$\tilde{p}(v) = 2\gamma \text{sinc}(2\pi\gamma\omega), \tag{4.22}$$

where we define $\text{sinc}(x) = \sin(x)/x$. In an inline Fourier holographic setup, $z_r = z$. By expanding the exponential term in Eq. (4.4) we see that

$$c(x) = \int_{-\infty}^{\infty} \left[U(X) \exp\left(\frac{j\pi X^2}{\lambda z}\right)\right] \exp\left(\frac{-j2\pi xX}{\lambda z}\right) dX. \tag{4.23}$$

By comparing, Eq. (4.23) and Eq. (4.7), it is clear that the term, $U(X)\exp\left(\frac{j\pi X^2}{\lambda z}\right)$ can be recovered, by performing an inverse and scaled Fourier transform on Eq. (4.24). Thus the reconstructed signal in the Fourier system is given by:

$$R_{N\psi}(X) \quad = \quad \psi^{-1}\left\{ c(x) \otimes p_\gamma(x) \sum_{n=-\infty}^{\infty} \exp\left(\frac{j2\pi nx}{T}\right)\right\}\left(\frac{X}{\lambda z}\right). \tag{4.24}$$

This is simpler to understand initially when, $n = 0$, and noting the relationship described in Eq. (4.9), the RHS of Eq. (4.25), can be rewritten as

$$\begin{aligned} &\psi^{-1}\left\{c(x) \otimes p_\gamma(x)\right\}\left(\frac{X}{\lambda z}\right), \\ &\left[U(X)\exp\left(\frac{j\pi X^2}{\lambda z}\right)\right]\left[2\gamma\text{sinc}\left(\frac{2\pi\gamma X}{\lambda z}\right)\right]. \end{aligned} \tag{4.25}$$

Using the result of Eq. (4.25), in combination with the scaling and shifting properties of the Fourier transform we arrive at the following result

$$R_{N\psi}(X) \quad = \quad \sum_{n=-\infty}^{\infty} \left\{ U\left(X - \frac{n\lambda z}{T}\right) \exp\left[\frac{j\pi\left(X - \frac{n\lambda z}{T}\right)^2}{\lambda z}\right]\right\}\left\{2\gamma\text{sinc}\left[\frac{2\pi\gamma\left(X - \frac{n\lambda z}{T}\right)}{\lambda z}\right]\right\}. \tag{4.26}$$

Comparing Eq. (4.26) and Eq. (4.21), we see that there are significant differences between the two reconstructed fields, particularly in relation to the role that the finite pixel size plays in determining the image detail that can be recovered. The results indicate that in a Fresnel system, the finite pixel size acts to attenuate higher spatial frequencies through a convolution operation. However in a Fourier system, the effect of

the finite pixel size is to multiply the reconstructed field with a sinc-type function, [10]. In the Fourier case the finite pixel size does not effect the recovery of spatial frequencies.

4.3 Numerical simulations.

We now turn our attention to that difficult problem of simulating the propagation of a speckle field [10] which has been discussed in more detail here [22–24] . We imagine that the object we are interested in is in fact an optically rough diffuser of a finite extent $2D$. The field immediately after the diffuser, then is limited by the finite extent of an aperture, $p_D(X)$ defined in a manner similar to how we defined the pixel function earlier in this chapter. This rough diffuser surface imparts a random phase profile to that plane wave that illuminates it producing a phase values that varies uniformly over the range $[0, 2\pi]$. This field is given by the following expression:

$$U(X) = p_D(X) \exp\left[j2\pi\alpha_{rnd}(X)\right]. \tag{4.27}$$

The function, $\alpha_{rnd}(X)$, is a random and delta correlated distribution, (see for example Ref. [24]), that generates numbers, distributed uniformly over the range 0 to 1, for each position of X. There is not an analytical solution for this diffraction problem and so we turn to numerical methods to calculate the distribution in the diffraction plane. Since a numerical solution is required, we must define the input field, $U(X)$, for a finite number of samples. Hence the sampled input field is given by

$$\overline{\mathrm{U}} = \left[U_1, U_2, ...U_{M_{in}}\right], \tag{4.28}$$

where M_{in} is the number of samples we take of the input field. We note that $U_m = U(X_m)$, where the spatial sampling vector is given by

$$\overline{\mathrm{X}} = \left[X_1, X_2, ...X_{M_{in}}\right], \tag{4.29}$$

where the extent of the input field is $2D$ and where the sampling interval is $\delta X = 2D/M_{in}$.

The field in the diffraction plane is then calculated with the following expression

$$u_{Nz}(x) = \frac{\delta X}{\sqrt{j\lambda z}} \sum_{m=1}^{M_{in}} U_m \exp\left[\frac{j\pi}{\lambda z}\left(x - X_m\right)^2\right]. \tag{4.30}$$

$u_{Nz}(x)$ is a continuous output field that is calculated from a finite set of M_{in} complex numbers and we highlight this feature using the subscripted 'N' in Eq. (4.30). The variable m, is an integer.

Although the output from Eq. (4.30) is a continuous function of x, for the purposes of generating Fig. 4.2, and for the processing of later results, we choose to examine the output of Eq. (4.30) for a specific set of x values,

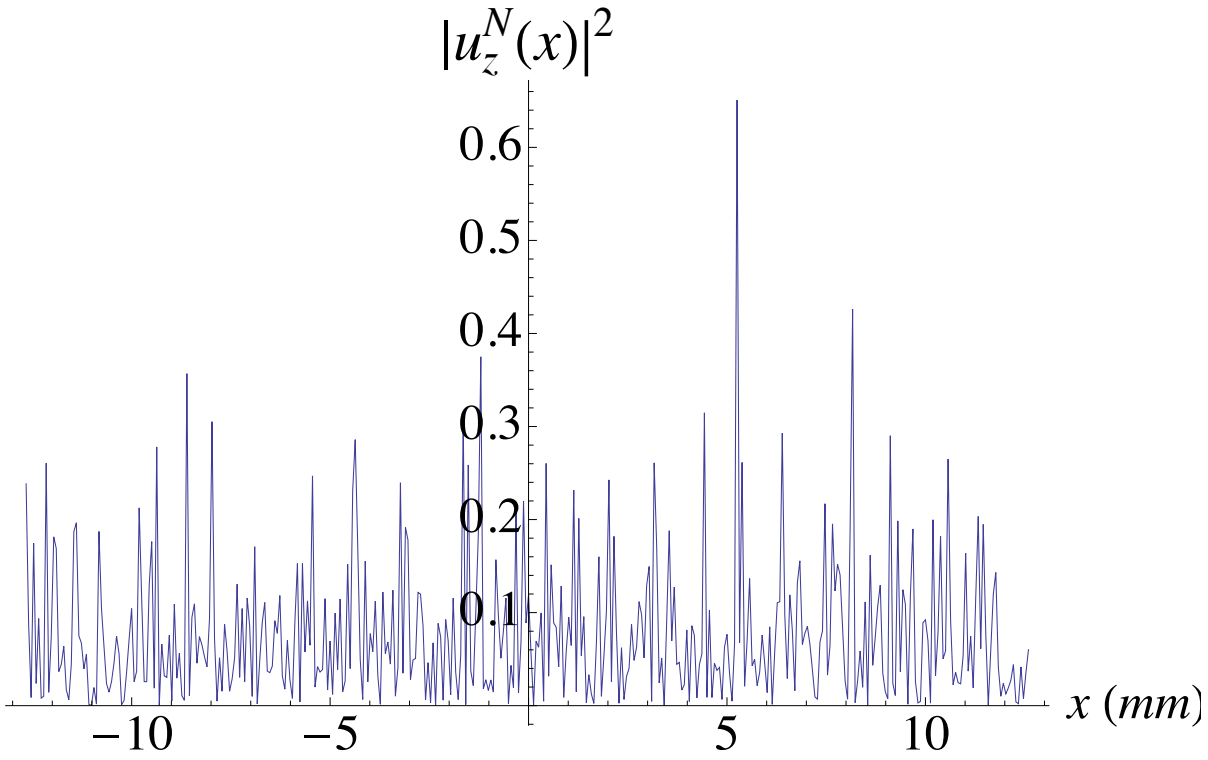

Figure 4.2 – Example calculation of $|u_z^N(x)|^2$, for the following parameters: $M_{out} = 400$, $z = 10$ cm, $\lambda = 633$ nm, and $D = 1$ mm, and where $M_{in} = 800$ uniformly spaced samples were taken over the input aperture extent of $2D = 2$ mm, taken from Ref. [10].

$$\overline{\mathrm{x}} = [x_1, x_2, ...x_{M_{out}}], \tag{4.31}$$

where M_{out} is the total number of samples we take from the output field. This spatial vector, $\overline{\mathrm{x}}$, identifies the spatial locations of the uniformly spaced sensor pixels, which

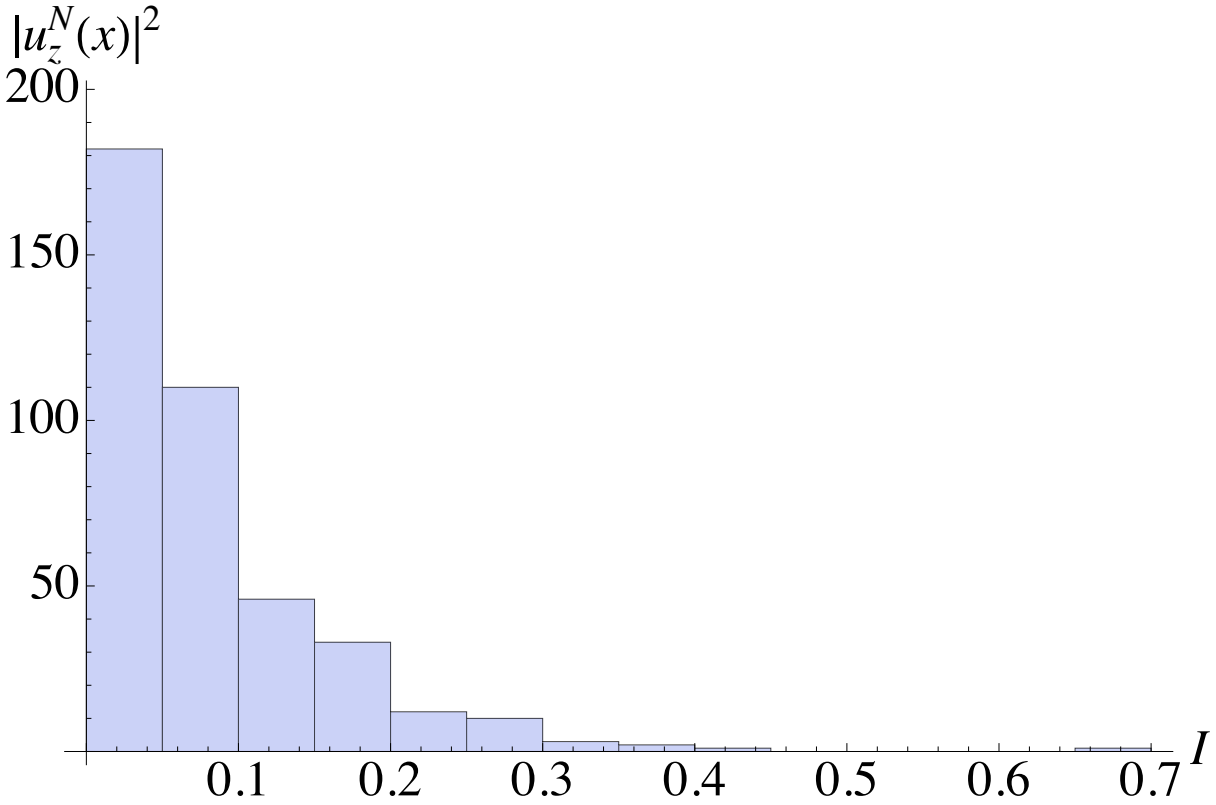

Figure 4.3 – Histogram plot showing the statistical distribution of the numerically simulated intensity distribution. No averaging by the pixels occurs here. The variable I is the intensity value and the total number of values contributing to the following histogram distributions is $M_{out} = 400$, taken from Ref. [10].

give a sampling interval of $T = 63.3$ μm, for the values listed in the caption of Fig. 4.2. The speckle size is given by the following formula [22–24],

$$S_{\text{lat}} = \frac{\lambda z}{2D}. \tag{4.32}$$

Setting $\lambda = 633$ nm, $D = 1$ mm and $z = 10$ cm, gives $S_{\text{lat}} = 31.\ 65$ μm. Choosing a sampling interval, $T = 63.3$ μm, means that the sensor is under-sampling the intensity distribution in a Nyquist sense and there are on average two speckles between the centers of adjacent sensor pixels.

We note that unlike calculating using fast numerical algorithms that are based on

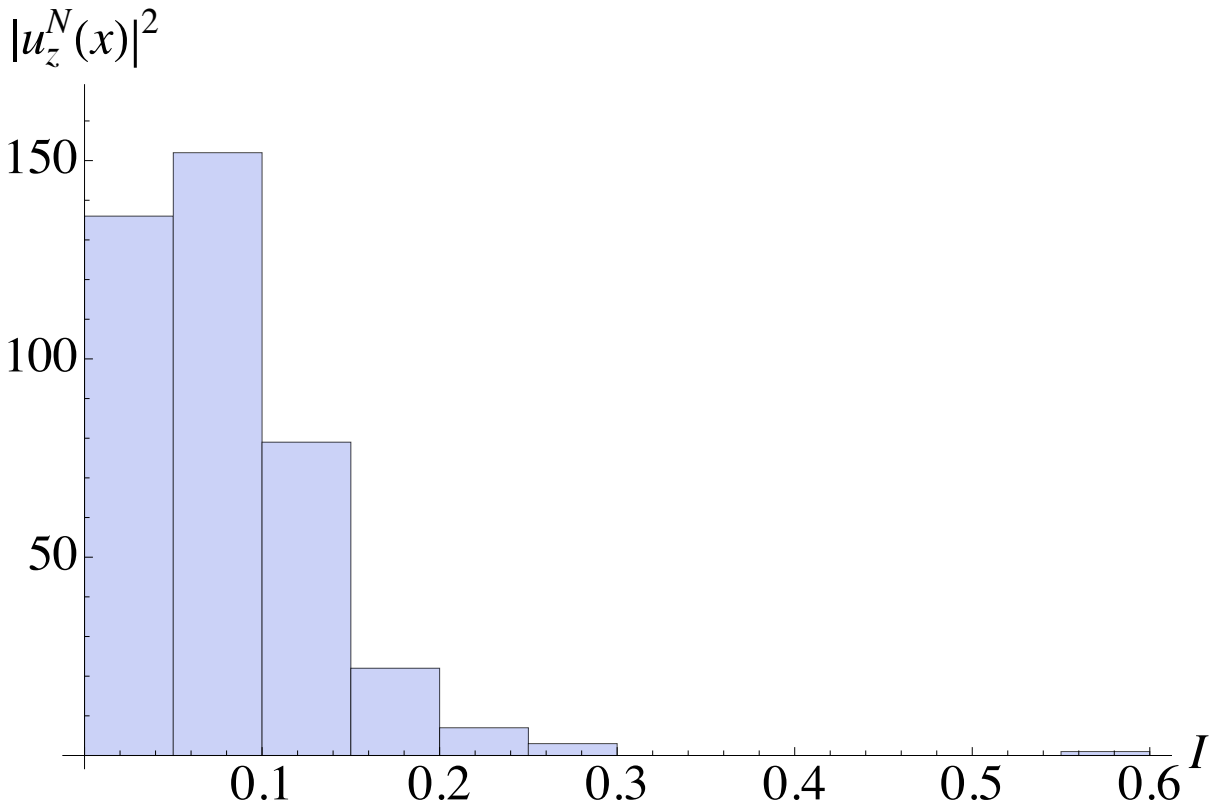

Figure 4.4 – Histogram plot showing the statistical distribution of the numerically simulated intensity distribution. Averaging by the pixels occurs here and the statistical distribution changes, again $M_{out} = 400$, taken from Ref. [10].

the FFT, we have complete freedom to choose any values we wish to look at simply by specifying the spatial location x, in Eq. (4.30). To achieve the same result with FFT algorithms often a combination of zero padding or inserting zeros between samples is required as was discussed in Chapter 1.

Statistics of the detected (integrated) speckle distribution.

As we have noted the sensor pixel plays an important filtering role in digital holography. If the sensor pixels are point detectors, we expect the intensity values of the speckle field, to follow a negative exponential distribution, [10]. The distribution shown in Fig. 4.3, consists of intensity values at the spatial locations given by $\overline{\mathrm{x}}$. It clearly follows a negative exponential distribution, supporting the numerical technique that we use to simulate speckle fields.

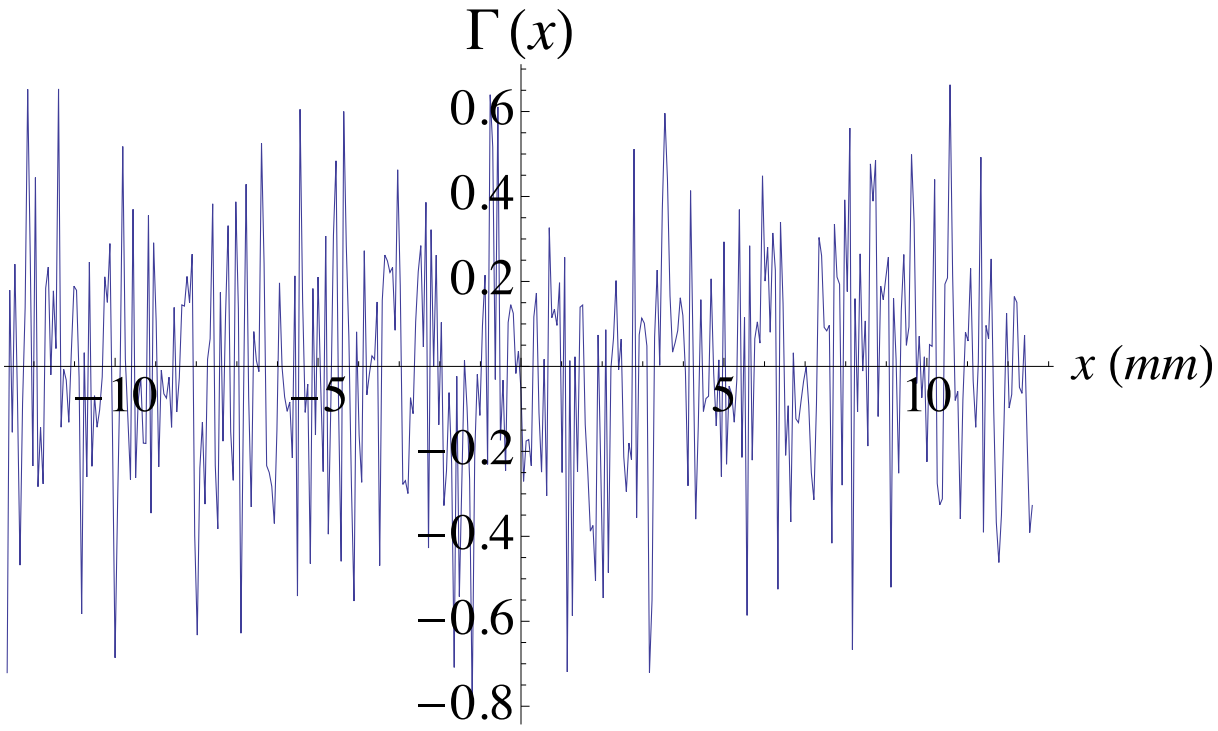

Figure 4.5 – Plot of the interference term, $\Gamma(x)$ for a lensless Fourier system where the focal length of the reference wave $z_r = z$, taken from Ref. [10].

The statistics of the detected (integrated) speckle field are different; since the averaging effect of the finite pixel size is now accounted for. Using the sampling vector, $\overline{\mathrm{x}}$, we define the locations of the centers of each sensor pixel. Now using a trapezoidal-based numerical integration technique, we average the light intensity about these sensor pixel center locations. Thus for sensor pixel 'm' we integrate the intensity over the range $x_m - \gamma \leq x \leq x_m + \gamma$.

The result is shown in Fig. 4.4, and we can see that the statistics no longer follow a negative exponential distribution. For example, we see that the most likely speckle intensity value is no longer zero rather the peak of the distribution. Rather it shifts to a positive non-zero value. It is possible to develop a theoretical model to describe this new statistical distribution. We again note that the numerical simulation technique we

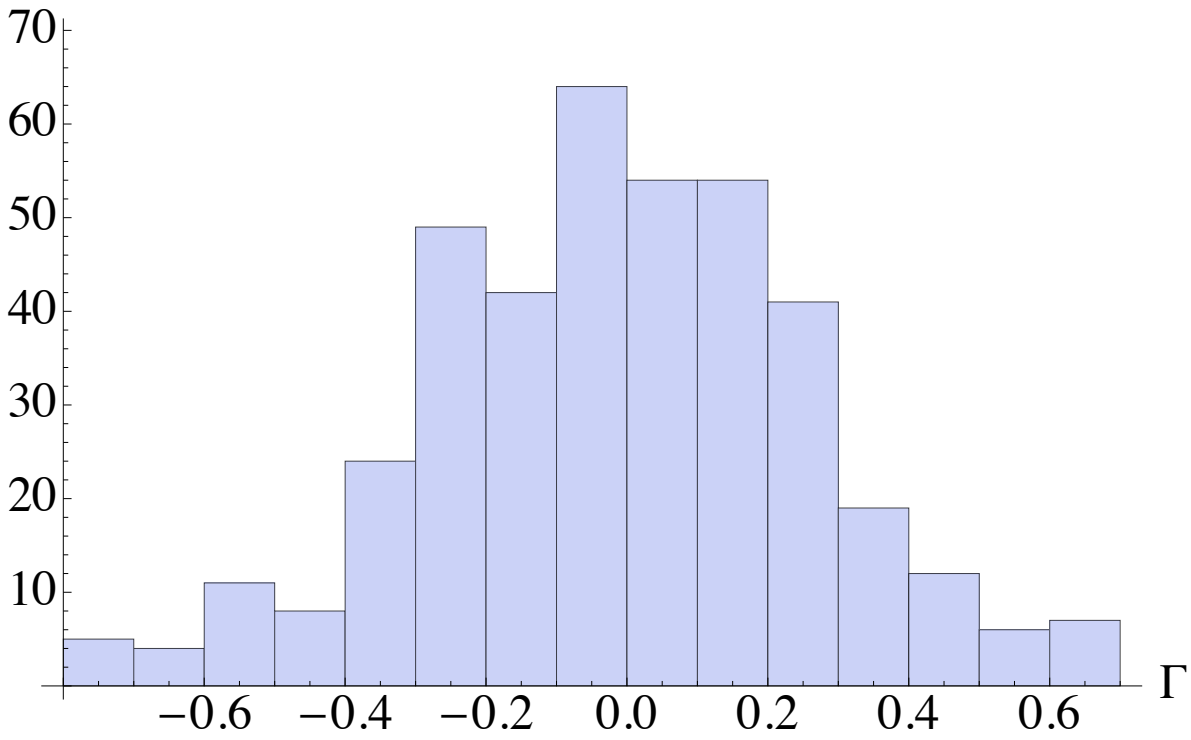

Figure 4.6 – Histogram plot showing the statistical distribution of $\Gamma(x)$ in a lensless Fourier system where the focal length of the reference wave $z_r = z$, and we note that $M_{out} = 400$, taken from Ref. [10].

use both, to generate the fully developed speckle field, and to model the averaging effect of the sensor pixels, agrees with analytical theoretical models that have been developed elsewhere [22–24].

Statistical distribution of the interference term.

Now we use this numerical simulation technique to examine the properties of the interference term, $\Gamma(x)$, for both inline Fourier and Fresnel holographic set-ups. To be consistent we keep the same values as in the previous section, seting $2\gamma = T$. To isolate $\Gamma(x)$, the intensity of the reference wave and the intensity of the speckle field should first be recorded, and numerically subtracted from $H(x)$, see Eq. (4.3). Setting, $z_r = z$ in Eq. (4.2) we have a Fourier system. In Fig. 4.5 the resulting distribution is plotted, which should in fact average to zero so that power is conserved at the sensor plane. When we

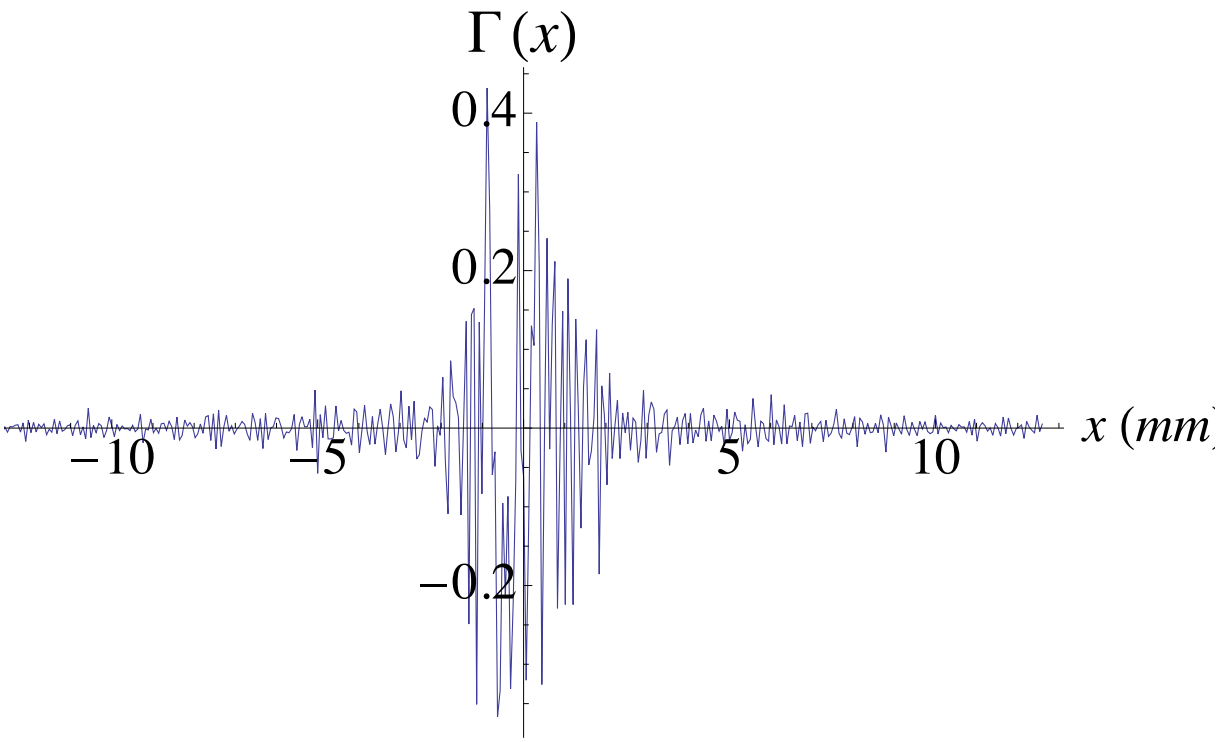

Figure 4.7 – Plot of interference term, $\Gamma(x)$, for a Fresnel system, taken from Ref. [10].

integrate over $\Gamma(x)$ over the range shown in Fig. 4.5 , we get a value of -0.319×10^{-3}. In Fig. 4.6 we present a histogram of the distribution and we see the values are distributed around zero with a certain spread, ± 0.7. We now examine the characteristics of $\Gamma(x)$, for the Fresnel system, presenting the a plot of the interference term in Fig. 4.7. There are significant differences between this distribution and the Fourier distribution depicted in Fig. 4.5 . In Fig. 4.7 , the maxima and minima of $\Gamma(x)$ appear to be lower than in Fig. 4.5 and more striking is that these maxima/minima points occur near the center of the sensor array, tapering off in value as one moves out to the left or right from the origin. These differences are reflected in the statistical distribution of the $\Gamma(x)$ as can be seen by inspecting Fig. 4.8 . Again the distribution appears centered about 0, however nearly all of the $\Gamma(x)$ values lie within the range $0.2 \leq \Gamma(x) \leq 0.2$.

From these numerical results we see that there is a significant statistical difference

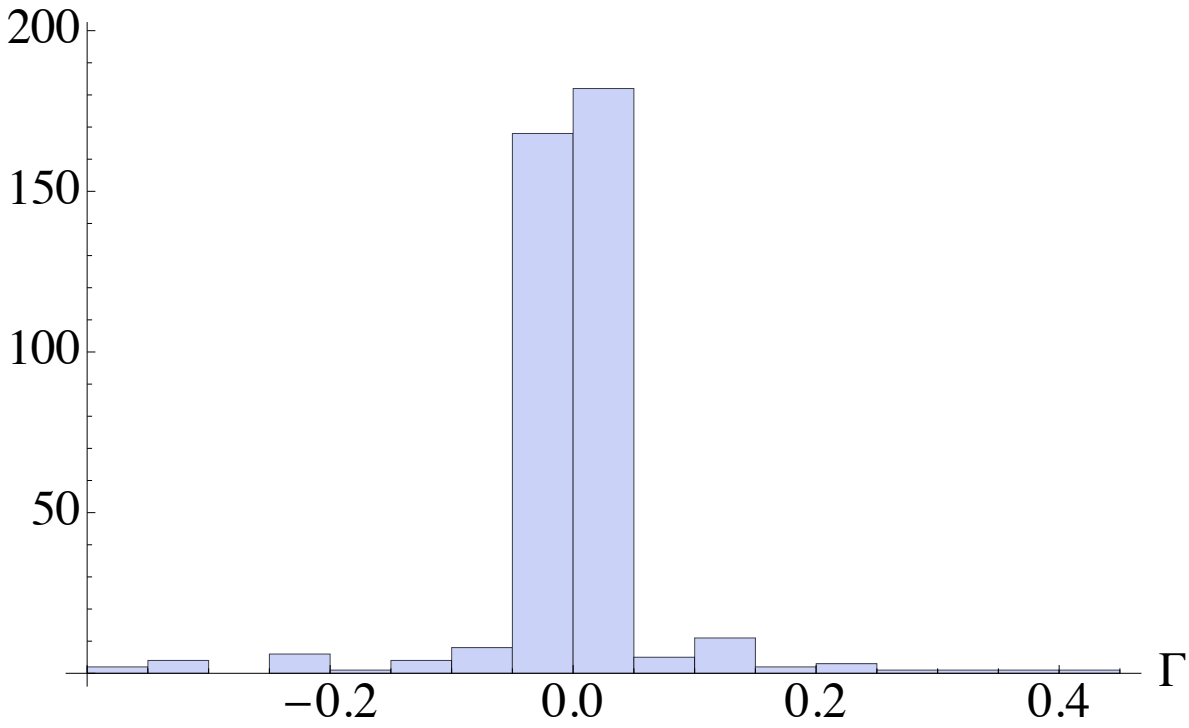

Figure 4.8 – Histogram plot showing the statistical distribution of $\Gamma(x)$ for a Fresnel system, $M_{out} = 400$, taken from Ref. [10].

between the interference term for a Fresnel and Fourier system, when the object wave field is a fully developed speckle field, that is under-sampled in a Nyquist sense by the sensor pixels. This difference is due to the intensity averaging by the sensor pixels of the light incident upon them. We note that when the numerical calculation is repeated for the Fresnel case when the sensor pixels act as point detectors, i.e. we do not perform any averaging, then the distribution looks statistically similar to the Fourier case. Thus we come to the conclusion that the averaging of the intensity by the sensor pixels plays a fundamentally important role; And this role changes, depending on the holographic system used to record the hologram. In particular these results seem to indicate that it is more difficult to achieve an interference effect for unresolved speckles when a plane wave is used as the reference. This may have significant implications for interferometric speckle based metrology systems.

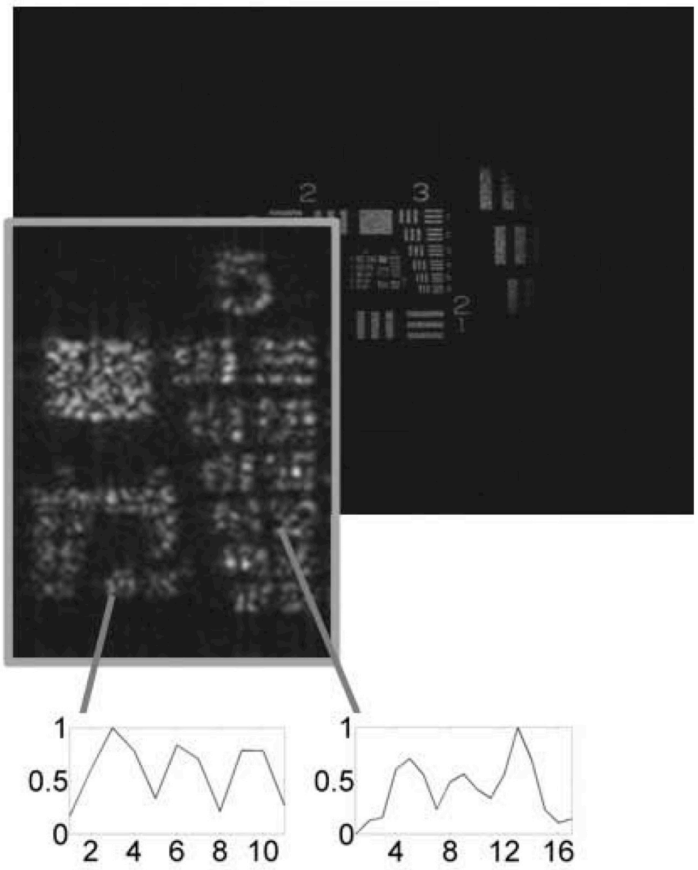

Figure 4.9 – Reconstruction of a USAF chart; no downsampling or averaging has been performed, and this result serves as a 'high-quality' reconstruction against which the downsampled and averaged Fourier and Fresnel reconstructions can be compared, taken from Ref. [10].

4.4 Some experimental results.

In this section we present some experimental results comparing the role of the pixel averaging operation for a Fourier and a Fresnel based holographic system. In our experiment a standard negative USAF (transmission) chart is illuminated from behind with a speckle field. A CrystaLaser, wavelength of 785 nm, served as the light source. Having been spatially filtered, the beam was collimated and divided into the reference and object waves by a beam-splitter, see Fig. 4.1. The plane wave segment propagating in the object arm is directed through a piece of ground glass, forming a speckle field behind which is used to illuminate the USAF chart. The field immediately after the USAF chart is the object wave, $U(X)$. This object field propagates to the sensor plane where it is mixed with a plane reference wave to form a hologram. The

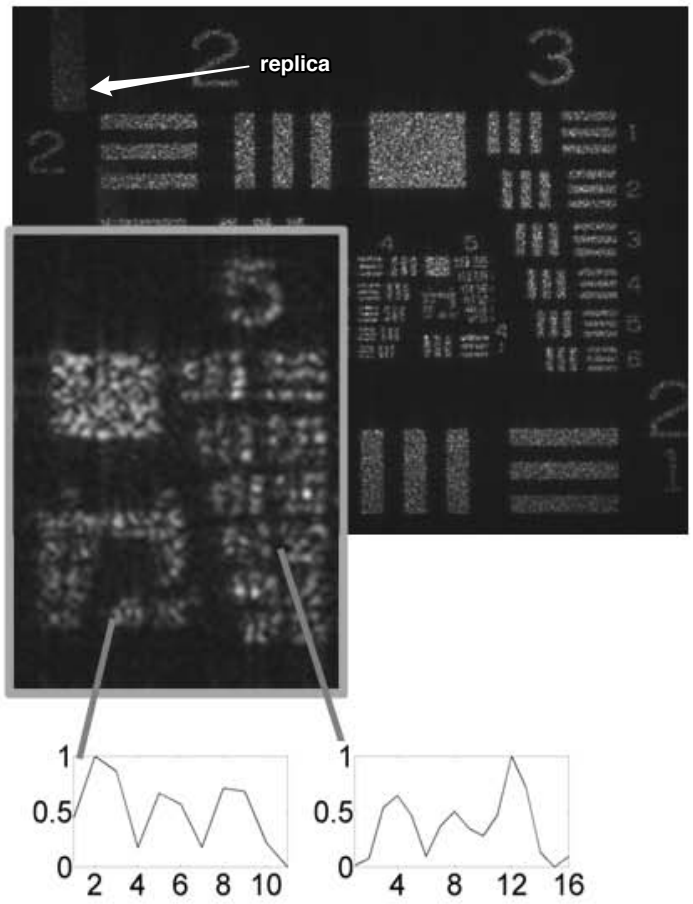

Figure 4.10 – Reconstruction of the downsampled and averaged Fourier hologram, taken from Ref. [10].

hologram was recorded by a CCD sensor, AVT Dolphin F-145B with 1392×1040 pixels and a pixel pitch of 6.45 μm. To isolate the $c(x)$ term, phase shifting interferometry was performed using a mirror mounted on a a piezo actuated motor (PiezoSystemJena PZ38CAP with controller NV40/1CLE). Four holograms were taken, where the reference phase between each successive capture, was stepped by $\pi/2$ over the range 0 to $3\pi/2$. Then using the phase shifting technique outlined earlier we can recover the $c(x)$ term. A reconstruction of this hologram with a zoomed in region is presented in Fig. 4.9. The reconstruction was performed using the direct method to implement an inverse Fresnel transform, which entails a single FFT operation and two chirp multiplications [**?**].

Here we wish to examine how changing the reference field, from a plane to a spherical, wave impacts on the quality of the reconstructed distribution. We expect that a larger pixel size will limit the ability of a Fresnel system to recover spatial frequencies, while it

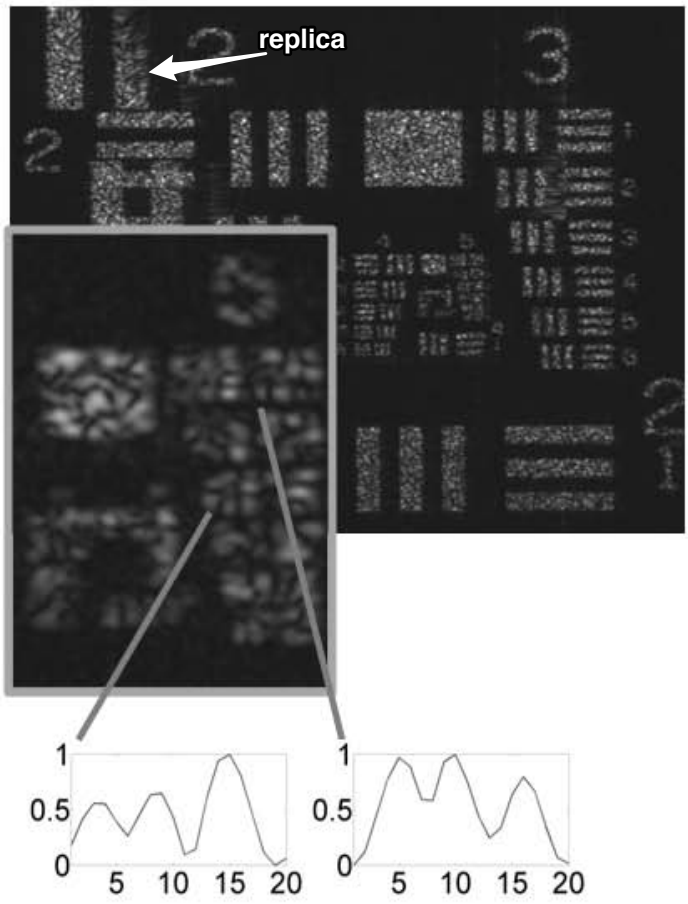

Figure 4.11 – Reconstruction of the downsampled and averaged Fresnel hologram. Note the difference in the brightness of the replica in this reconstruction and that in Fig. 4.10, taken from Ref. [10].

would not be limiting for a Fourier system. In order to directly compare these characteristics we artificially create a Fourier hologram from the Fresnel hologram, multiplying it by the conjugate of the spherical reference wavefield, see Eq. (4.2). This is performed numerically in a computer. We now have two holograms, one Fourier and one Fresnel, and can directly compare how the pixel function affects the reconstructed hologram.

To change the effective size of the pixels we add the values returned by neighboring pixels together, so as to create a larger pixel size. We note that this reduces the effective sampling interval between pixels, but not the overall extent of the sensor array (there will be a smaller number of larger pixels). This particular point has been discussed in Ref [13]. In Fig. 4.10, we present the result for the Fourier hologram. The smallest resolvable test target element was determined by calculating an averaged cross-section for the investigated element. Care was taken so that the ratio of the maximum to

the minimum value (black strip) is less than 0.81 according to the Rayleigh resolution criterion for a rectangular aperture. Comparing the cross-section plots from Fig. 4.9 and Fig. 4.10, we see that they are identical, indicating that neither the downsampling, nor the averaging by the sensor pixels, has affected the reconstructed hologram in this spatial region. Examining Fig. 4.11, we see that the result for the Fresnel hologram indicating that the pixel averaging has a significant effect on the reconstruction. We also draw the reader's attention to the replicas that are visible in Fig. 4.10 and Fig. 4.11. We observe that there is a significant difference in the brightness of these replicas in the two different systems, where the replicas appear much brighter in the Fresnel case.

We have examined some important aspects of coherent digital imaging systems that work by measuring the intensity and phase of an optical wavefield. This necessitates the use of a known reference wave, several consecutive captures and then numerical processing and propagation of a wavefield using the Fresnel transform. The properties of these systems have been specifically examined in the following publications, [8, 9, 13, 14, 17, 18] and more recently here [37]. In the next chapter we will examine an alternative means of estimating the phase distribution of an optical field using an optimization process known as iterative phase retrieval. There are broadly speaking two categories of phase retrieval techniques, the so-called transport of intensity methods and iterative phase retrieval. A discussion of the transport of intensity approach is presented here [18].

Chapter 5

The iterative phase retrieval problem

5.1 Background

Phase Retrieval (PR) techniques are an alternative approach to recovering the complex amplitude of an optical wavefield. Unlike holography, which uses a known reference wave, phase retrieval attempts to achieve the same goal using a set of intensity measurements. Even within phase retrieval approaches there exist two distinct methods: (i) Transport of Intensity based PR and (ii) Iterative PR. Although several techniques exist, here we will examine the iterative PR exclusively. To recover the phase information with this approach several intensity distributions, diffracted from the object of interest, are recorded at different optical planes. A significant advantage of the PR is the relative simplicity of the optical setup, compared with an interferometric approach. With this approach, noise sources such as an imperfect reference wave can be avoided. PR techniques are an ill-posed inverse problem and hence initial conditions play an important and relatively poorly understood role.

To begin the PR algorithmic process an estimate of the wavefield's phase distribution is required. It is assumed that the errors in this initial guess are continuously improved through an iterative algorithm so that the final estimate approaches that of the actual wave field phase distribution. In practice, due to the ill-posed nature of the problem, this is not always the case. Additionally, the only means we have of estimating the accuracy of our final solution is the similarity of the actual measured distribution, to that, recovered from the PR process. Ideally if we have the correct phase information at a particular plane, we can use this to propagate the complex amplitude to other planes where we have recorded the actual intensity distribution. Differences between

the measured and recovered intensity distributions are attributed to an error in the phase estimate.

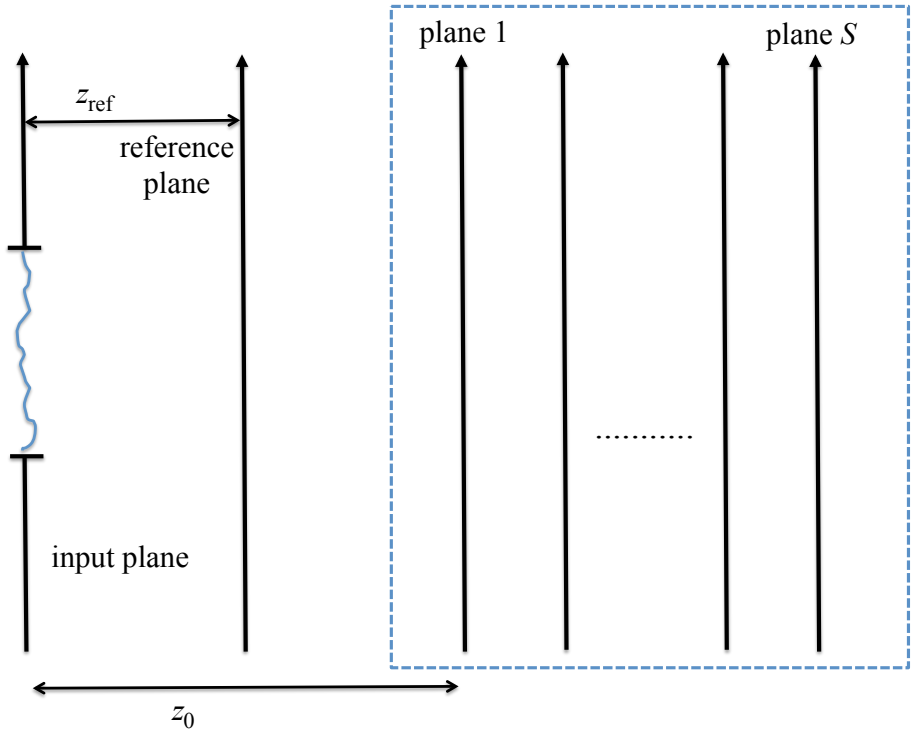

Figure 5.1 – Depiction of PR setup. An object is located in the input plane, whose amplitude and phase we wish to recover from a series of S intensity measurements made a S different planes. Only those planes that lie within the dotted box, i.e. Planes 1 to S, are used in the PR algorithm, while the intensity in the reference plane is used to check whether the PR algorithm has converged to the correct solution.

5.2 Experimental method

In Fig. 5.1 we depict a schematic of the experiment that was carried out. The object is illuminated with a HeNe laser beam, wavelength 633 nm, and a series of intensity distributions (pixel value M×N, 2048×2048) are captured with a CCD sensor (Kodak KAI-4022, pixel pitch $\Delta x = 7.4$ μm) in axially displaced planes. The capture planes are denoted 01 to S, in Fig. 5.1 and are axially displaced from each other by $\Delta z = 2$ mm. Here we use the Forward Backward (FB) algorithm, presented in Ref. [2]. The square root of the captured intensity in plane 01 and a chosen initial phase form the initial guess of the complex amplitude. This artificial distribution is propagated from plane to plane until the last plane, plane S, is reached and then step-by-step back propagated to

the first plane, plane 01. A complete run through the data set of captured intensities in forward and backward direction is one iteration step. In our PR experiment a ground glass diffuser serves as our object. The first intensity distribution is recorded at a distance of $z_0 = 185$ mm, from the diffuser plane. The size of the illumination spot, the propagation distance (here z_0) and the wavelength of the laser determine the lateral speckle size in plane 01. The speckle size of the measured intensity in plane 01 is $7.73\Delta x$. Here we define the lateral (horizontal) speckle size, by performing an autocorrelation of the intensity captures, and measuring the full width of this peak at one tenth of maximum (FWTM).

Care has been taken to ensure that the axially displaced intensities, see Fig. 5.1, are sufficiently different from each other so as to provide a stable numerical solution. The iterative PR approach requires that there is sufficient diversity between each of the measured intensity distributions in order for the algorithm to converge properly [2]. So, when choosing Δz the lateral and longitudinal speckle size have to take in account. The bigger the lateral speckle size is, the longer the speckles are and so a larger axial distance Δz is required to fulfil these diversity criteria.

As noted earlier we also record, an intensity distribution in the reference plane, see Fig. 5.1. This reference intensity is kept out the PR process and used only for evaluating the result of the PR. If we have correctly estimated the phase distribution we should also be able to accurately reconstruct this reference plane intensity. We now investigate how the initial conditions influence the result of a PR. We refer to the initial guess phase and the number of intensity captures as the initial conditions. The PR algorithm runs with a flat (constant) phase as initial guess and 2, 5, 10 and 20 intensity captures. The algorithm is terminated when the RMS error con- verges to a minimum. Sixty iterations are used for a PR with 5 intensities and thirty with 10 or 20 intensities. For a PR with two captures the algorithm is terminated after 280 iterations.

Since we use intensity captures of a speckle field, we can determine the lateral speckle size in the measured and iterated intensities and compare these values. The speckle size is used as a second metric to evaluate the accuracy of the retrieved distribution. The speckle size of the measured intensity is (7.73 Δx) in plane 01, and that of the iterated it is (6.53 Δx) for a PR with 20 planes, and (7.20 Δx) when 10 planes are used. The RMS error of the iterated and measured amplitude for a PR with 20 planes and 10 planes is 0.089 and 0.057, respectively. The results of the PR with 10 planes seem to be a bit better than these of a PR with 20 planes because the RMS error is lower, and the speckle size, is closer to that of the measured speckle size. When we use a FB

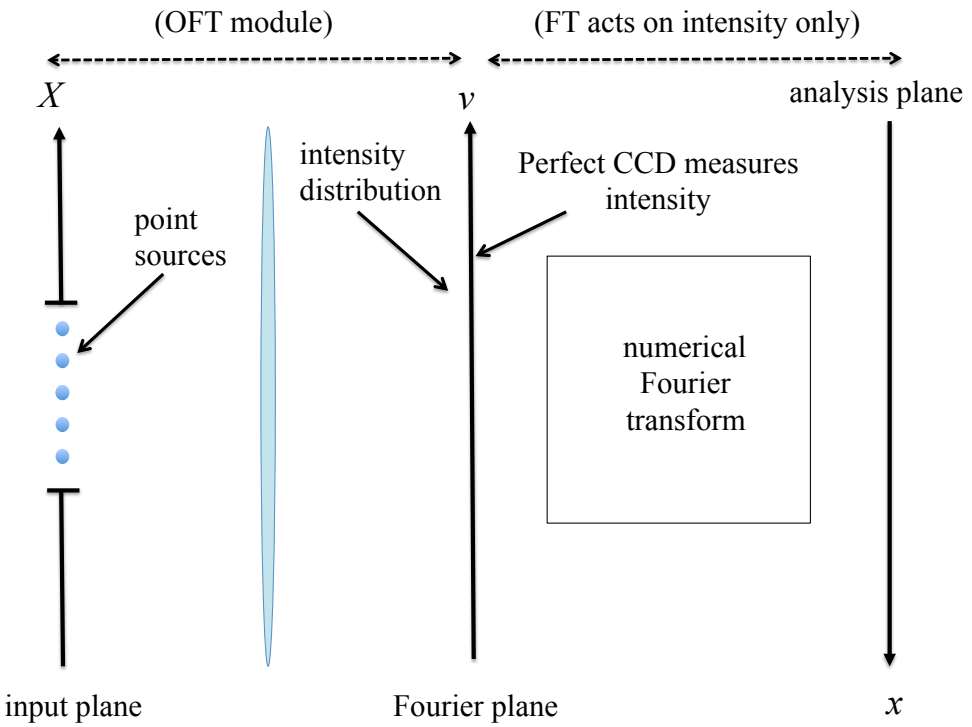

Figure 5.2 – Intensity profile of the captured and reconstructed distribution in the reference plane (1D depiction in x-direction), for retrieving the complex amplitude the FB algorithm is used with 2, 5 10, 20 intensity captures and as initial guess a plane phase (left plots) and a random phase pattern with a correlation width of (7.63 Δx) (right plots), Reprinted from Ref [30].

algorithm with only two planes, the speckle size in the iterated intensity is (7.71 Δz) and the RMS error is 0.042 after 280 iterations.

These results would appear to indicate that a PR process where less intensity captures are used and hence less information, can nevertheless provide better results. This impression is misleading however which becomes apparent once we compare the actual intensity distribution in the reference plane to that reconstructed from the PR algorithm. The complex amplitude distributions retrieved from the PR process are back propagated from plane 01 to the reference plane for $z_{REF} = 10$ mm, see Fig. 5.1. The back propagated distributions are referred as the "reconstructed" fields. To evaluate, whether a good retrieval has been achieved, the reconstructed and the captured reference images are compared.

Examining the RMS error and the speckle size of the iterated intensity in plane 01, the

best results are obtained employing the FB algorithm with only two intensity captures. Propagating the retrieved complex amplitude back to the reference plane evaluable results are not achieved. But the more intensity captures are used in the FB algorithm the better the quality of the reconstructions become, see Table. 1. To evaluate the reconstructed intensity and hence the retrieved distribution one can use the RMS error, the speckle size or the correlation coefficient. Here how- ever we plot cross sections of the captured and reconstructed intensity distributions. All images have a pixel number of 2048×2048. For the intensity profile a pixel row in the center of each image is read out, the start and end point in pixel coordinates is (925,1024) and (1124,1024), respectively. Fig. 5.2 depicts the profiles of the reconstructed and captured intensities for the PR experiment and different numbers of planes. It is obvious, the more planes are used in the FB algorithm the re- constructed intensity becomes more similar to the captured one.

The left graphs in Fig. 5.2 show the results when as initial guess a plane phase is used. Can we improve the results when another initial phase is used? If a 'good' initial guess is used, will be the role of the number of intensity captures reduced? Since in our PR experiment intensity captures of a speckle field are employed, we decided to use as initial guess a pattern with random phase values. For this phase pattern random numbers are generated, which are distributed uniformly. To get a finite correlation width the phase pattern is filtered in the Fourier domain and the correlation width is determined by the FWTM. Three different phase patterns are employed with a correlation width around the speckle size of the desired wave field in plane 01, a second with a smaller and a third with a bigger correlation width than the speckle size. The best results are achieved when a phase pattern is used with a correlation width around the speckle size. We determine this initial phase pattern as a 'good' guess and employ it in a PR experiment with different numbers of planes: 2, 5, 10 and 20. With this particular phase distribution and 20 captures are the best reconstructions achieved within all the presented PR experiments. Using less intensity captures the quality of the reconstructions gets worse.

5.3 A preliminary comment on the results

From these results we summarize the main conclusions:

- The more intensity measurements made the more likely it seems for a gradient descent optimization algorithm to converge to the physically correct solution
- Each measurement capture must contain new information that effects the path the gradient descent algorithm takes

- One has to have a good 'initial guess' at the starting phase distribution. It seems there are many extrema which can act to trap the gradient descent algorithm in a local maxima or minima and not allow convergence to a global error minimum.

These conclusions have been derived from experimental testing and vague intuition, however they seem to be representative of the current view of iterative PR techniques. In order to be more concrete and specific in the following section we re-examine the PR problem using an idealized 'Gedanken' experiment. The purpose is to examine the nature of the correct solution, to shed some light on local minima and understand why a good 'initial guess' is decisive in determining the success of the PR technique.

5.4 Analysis of an idealized thought experiment

We begin our analysis by examining the idealized optical system depicted in Fig. 5.3. A set of N distinct point sources, each with a known intensity value and hence known magnitude, a_n, where a_n is the magnitude of point source n. The phase value, ϕ_n associated with each point source however remains the unknown physical parameter that we wish to measure. So to reiterate the problem, as depicted in Fig. 5.3 is that we are given a set of N point sources with known amplitudes and unknown phase values. We further assume that these points sources are uniformly spaced a distance Δ from each other. We are also given a second set of intensity measurements, in this case we also record the intensity of the optical field in the Fourier transform plane. As we have noted in the previous section in practical PR measurements two major physical factors play a significant role in limiting the performance of such techniques: the finite extent of the CCD array used to make the intensity measurement and the finite size and number of the CCD pixels which average the light intensity incident upon them. We

Initial phase guess	Two planes	Five planes	Ten planes	Twenty planes	Actual Δx_s size
	RMS Δx_s	RMS Δx_s	RMS Δx_s	RMS Δx_s	
Plane	0.161 2.43	0.16 1.98	0.137 2.43	0.138 6.47	7.38
Random	0.161 2.28	0.16 1.95	0.136 6.93	0.138 6.49	7.38

Table 5.1 – RMS error and mean lateral speckle size $Deltax_s$ of the captured reconstructed amplitude AREF, REC in the reference plane for the Forward Backward algorithm with different numbers of planes and two different initial guess phase, i.e. plane or random. The variable Δx_s - speckle size of the captured intensity distribution, the speckle size is in pixel units

have examined such issues in previous chapters for holographic imaging systems, so here we will deliberately take a different approach. We will imagine that we can measure the intensity in the Fourier domain over an infinite extent and with a sampling step size that is arbitrarily high. We will also imagine that only a finite number of perfect point sources in the input plane (with known intensity but unknown phase) contribute to the Fourier plane intensity distribution. Hence in this analysis we exclude any physical imposed limiting factors on the ability of our system to make a measurement. This will allow us to significantly simplify the analysis and to concentrate an another and arguable more important effect: the existence of a very high number of alternative solutions to the PR problem. As we shall see it is possible that many different combinations of phase values can produce identical intensity distributions. Hence this PR problem is said to be ill-posed. We refer back to Fig. 5.3, where we have indicated that the contributing point sources are Fourier transformed by an imaginary optical Fourier transform system, where $\lambda f = 1$ and hence the Fourier distribution is unscaled. Here this distribution is incident on a material and its intensity distribution is recorded. Later we will perform a unscaled second optical Fourier transform on this intensity distribution and examine its Fourier transform. We note however that although we are performing two successive forward Fourier transforms, we do not arrive back at the input plane distribution since, we perform the second Fourier transform operation on the intensity of the of the Fourier distribution not on its complex amplitude, as in a 4-f imaging system. We thus begin by noting that the Fourier transform of a point source is given by

$$FT\left\{\delta\left(x+X_n\right)a_n\exp\left(j\phi_n\right)\right\}\left(v\right)=\exp\left(-j2\pi X_n v\right)a_n\exp\left(j\phi_n\right), \tag{5.1}$$

where X_n is the spatial location of point source 'n' while the parameters, a_n and ϕ_n, refer to its phase and amplitude respectively. Hence for a sum of N distinct point sources we can write

$$FT\left\{\sum_{n=1}^{N}\delta\left(x-X_n\right)a_n\exp\left(j\phi_n\right)\right\}\left(v\right)=\sum_{n=1}^{N}\exp\left(-j2\pi X_n v\right)a_n\exp\left(j\phi_n\right). \tag{5.2}$$

We are however interested in the intensity distribution of the field in the Fourier plane. We remember that the intensity of a complex number is given by that number times its complex conjugate. With this relationship in mind we now write the conjugate expression for Eq. (5.2)

$$FT\left\{\sum_{n=1}^{N}\delta\left(x-X_n\right)a_n\exp\left(j\phi_n\right)\right\}^{*}\left(v\right)=\sum_{n=1}^{N}\exp\left(j2\pi X_n v\right)a_n\exp\left(-j\phi_n\right), \tag{5.3}$$

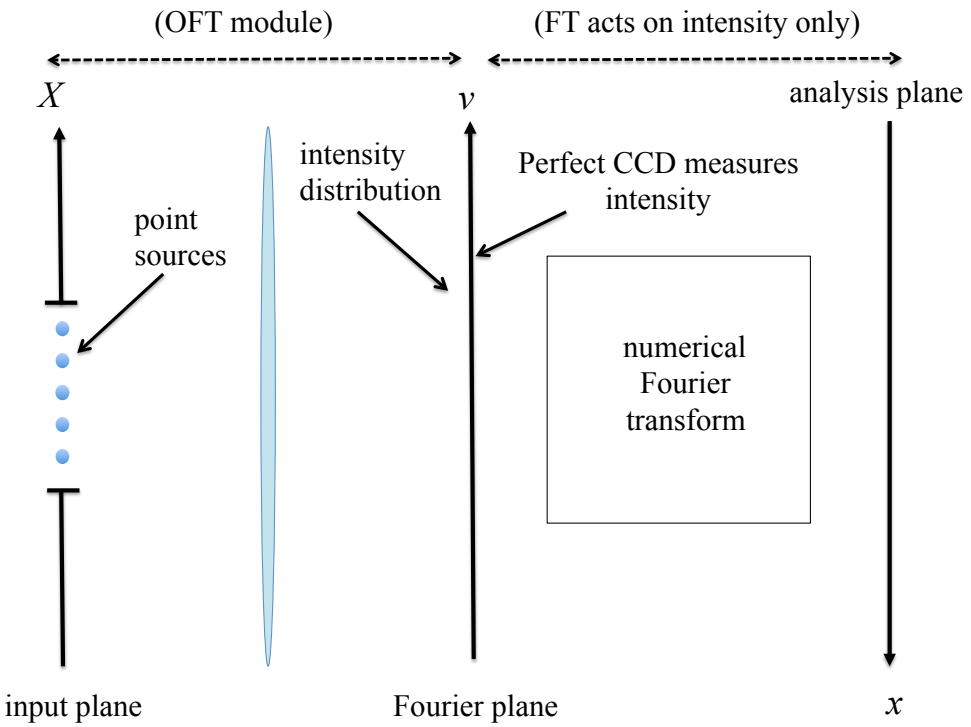

Figure 5.3 – Depiction of PR setup for an idealized 'Gedanken' experiment. A set of N point sources with known amplitude and unknown phase are Fourier transformed and the resulting intensity distribution appears in the Fourier plane. This intensity distribution is processed to determine the phase values of the N point sources in its Fourier domain - hence in this 'Gedanken' experiment the second OFT (Optical Fourier Transform) module acts on the intensity values only.

where '*' refers to a complex conjugate operation. We can now write an analytical expression for the intensity distribution in the Fourier plane which when simplified can be written in the following form

$$I_{\mathrm{FT}}(v) = \sum_{n=1}^{N} a_n^2 + 2\sum_{n=1}^{N-1}\sum_{m=1}^{N-n} a_m a_{m+n}\left\{\cos\left[2\pi\left(n\Delta\right)v + \phi_m - \phi_{m+n}\right]\right\}. \quad (5.4)$$

From Eq. (5.4) we can see that we have a sum of cosines. For each given value of n there is a specific spatial frequency component $f_s = n\Delta$, and there are $N-1$ terms. It is easier to analyze this double summation by initially concentrating on a single spatial frequency component, i.e. for a specific value of n, and we refer to such a component as $I_{\mathrm{FT}}^{n}(v)$. Noting the following trigonometric relationship: $\cos(A+B) =$

$\cos(A)\cos(B) - \sin(A)\sin(B)$, we can express $I_{\mathrm{FT}}(v)$ as

$$I_{\mathrm{FT}}(v) = \sum_{n=1}^{N} a_n^2 + \sum_{n=1}^{N-1} I_{\mathrm{FT}}^n(v), \tag{5.5}$$

where

$$\begin{aligned} I_{\mathrm{FT}}^n(v) &= 2\sum_{m=1}^{N-n} a_m a_{m+n} \cos\left[2\pi n\Delta v + (\phi_m - \phi_{m+n})\right] \\ &= 2\cos(2\pi n\Delta v) \sum_{m=1}^{N-n} a_m a_{m+n} \cos(\phi_m - \phi_{m+n}) \\ &\quad +2\sin(2\pi n\Delta v) \sum_{m=1}^{N-n} a_m a_{m+n} \sin(\phi_m - \phi_{m+n}). \end{aligned} \tag{5.6}$$

We now consider the inverse Fourier transform of $I_{\mathrm{FT}}^n(v)$, which we specifically define

$$\overline{I}_{\mathrm{FT}}(x) = \int_{-\infty}^{\infty} I_{\mathrm{FT}}^n(v) \exp(+j2\pi xv)\, dv, \tag{5.7}$$

where are now in a spatial domain once again. We note that in the idealized optical system, see Fig. 6.1, two forward optical Fourier transforms [defined with a kernel $\exp(-j2\pi vx)$] are performed, whereas in Eq. (5.7), we have defined an inverse Fourier transform operation, [with a kernel $\exp(+j2\pi vx)$]. We account for the sign change by flipping the direction of the axis in the spatial domain, see Fig. 6.1. Noting that

$$\begin{aligned} FT\left\{\sin(2\pi k_0 x)\right\}(k) &= \frac{j}{2}\left[\delta(k+k_0) - \delta(k-k_0)\right], \\ FT\left\{\cos(2\pi k_0 x)\right\}(k) &= \frac{1}{2}\left[\delta(k+k_0) + \delta(k-k_0)\right], \end{aligned}$$

then

$$\begin{aligned} I_{\mathrm{FT}}^n(v) &= \delta(x+n\Delta)\left\{\sum_{m=1}^{N-n} a_m a_{m+n}\cos(\phi_m - \phi_{m+n}) - j\sum_{m=1}^{N-n} a_m a_{m+n}\sin(\phi_m - \phi_{m+n})\right\} \\ &+ \delta(x-n\Delta)\left\{\sum_{m=1}^{N-n} a_m a_{m+n}\cos(\phi_m - \phi_{m+n}) + j\sum_{m=1}^{N-n} a_m a_{m+n}\sin(\phi_m - \phi_{m+n})\right\}. \end{aligned} \tag{5.8}$$

We see from Eq. (5.8) that the complex numbers (arising from the summation of sines and cosines) multiplying the $\delta(x-n\Delta)$ and $\delta(x+n\Delta)$ components are complex

conjugates of each other. Hence we see that

$$Re\left\{I_{\mathrm{FT}}^{n}\left(n\Delta\right)\right\} = \sum_{m=1}^{N-n} a_m a_{m+n} \cos\left(\phi_m - \phi_{m+n}\right), \tag{5.9}$$

and that

$$Im\left\{I_{\mathrm{FT}}^{n}\left(n\Delta\right)\right\} = -\sum_{m=1}^{N-n} a_m a_{m+n} \sin\left(\phi_m - \phi_{m+n}\right). \tag{5.10}$$

We also remember that the iterator n above spans the range: $1 \leq n \leq N-1$. Examining Eq. (5.9) and Eq. (5.10) we recognize that the only unknowns are the values for the phase parameters, ϕ_n. Both the initial amplitudes a_n are given and the LHS of each of equation is found by calculating the Fourier transform of the intensity distribution that we measure in the Fourier plane. We also note that the larger the value of n is, the lower the number of terms from Eq. (5.9) and Eq. (5.10) that contribute to both $Im\left\{I_{\mathrm{FT}}^{n}\left(n\Delta\right)\right\}$ and $Re\left\{I_{\mathrm{FT}}^{n}\left(n\Delta\right)\right\}$. When we set about trying to find ϕ_n from Eq. (5.9) and Eq. (5.10), we should start by first setting $n = N-1$, in which case the equations reduce to the following:

$$Re\left\{I_{\mathrm{FT}}^{N-1}\left[(N-1)\Delta\right]\right\} = a_1 a_N \cos\left(\phi_1 - \phi_N\right), \tag{5.11}$$

and that

$$Im\left\{I_{\mathrm{FT}}^{n}\left[(N-1)\Delta\right]\right\} = -a_1 a_N \sin\left(\phi_1 - \phi_N\right). \tag{5.12}$$

If we arbitrarily set $\phi_1 = 0$, then we can calculate ϕ_N from the following

$$\phi_N = \arctan\left[\frac{\sin\left(\phi_N\right)}{\cos\left(\phi_N\right)}\right], \tag{5.13}$$

which means that we now have values for both ϕ_1 and ϕ_N. Now setting $n = N-2$, Eq. (5.9) and Eq. (5.10) will reduce to the following:

$$Re\left\{I_{\mathrm{FT}}^{N-1}\left[(N-2)\Delta\right]\right\} = a_1 a_{N-1} \cos\left(\phi_1 - \phi_{N-1}\right) + a_2 a_N \cos\left(\phi_2 - \phi_N\right), \tag{5.14}$$

and that

$$Im\left\{I_{\mathrm{FT}}^{n}\left[(N-1)\Delta\right]\right\} = -a_1 a_{N-1} \sin\left(\phi_1 - \phi_{N-1}\right) - a_2 a_N \sin\left(\phi_2 - \phi_N\right). \tag{5.15}$$

This is where the difficulties with PR begin in earnest. This pair of coupled equations has eight different solution for (ϕ_2, ϕ_{N-2}), which are all valid. However only one of the solution pairs corresponds to the actual correct physical result, another solution is its complex conjugate. If we randomly choose from these solutions we will have a probability of 1/8 that we have chosen the physically correct answer.

Having decided on a particular choice of (ϕ_2, ϕ_{N-2}), we can then set $n = N - 3$ and repeat the process. We have found from analysis that each step leads to equations that have the form of Eq. (5.14) and Eq. (5.15), with two unknown values and each with a set of eight solution pairs. Hence at each step we have a 1/8 chance of guessing the physically correct solution, and for N point sources we will need to make approximately $N/2$ guesses at each step of the algorithm. Hence the chances that we correctly guess the correct phase for each point source is $(1/8)^{N/2}$ - a vanishingly small probability. In the experimental work described at the beginning of this chapter $N \approx 4$ million. Hence there are very fundamental limits on our ability to recover the physically correct phase values from intensity measurements made in an imaging and Fourier plane.

In iterative PR algorithms an initial guess is made as to the correct phase solution. The iterative algorithm is run which behaves like a gradient descent optimization process. For a given set of intensity measurements these algorithms do indeed find a set of phase values that minimize the error between the measured intensity values and the calculated intensities. However since there is such a large number of possible solutions to this problem, these optimized phase values are very unlikely to be the physically correct solution.

Chapter 6

Appendices.

Determining the entrance and exit pupils of an imaging system

When discussing general imaging systems, consisting of several lens and aperture stops, it is important to define what are known as the entrance and exit pupils of the optical system. These pupils (entrance and exit) are in fact images of the limiting aperture as seen from the entrance and exit planes respectively. Here by examining several figures we will demonstrate how the entrance an exit pupils are determined. We begin with an analysis of the entrance pupil in Fig. A.1A.1. The optical path that is actually travelled by the marginal ray leaving from Point A is marked as a solid black line in Fig. A.1. This however will appear different to an observer looking along the same path. It will appear that the ray travels along the path marked as a dashed black line after it passes through the lens L_1. Now imagine that the ray that passes through the centre of lens L_1 and just grazing the real physically limiting aperture. The point where this ray intercepts the marginal ray marks the plane entrance pupil plane. We see that the size of the entrance pupil, in this example is larger than the real limiting aperture. We now consider the exit pupil, which is determined in the same manner as the entrance pupil. Again we follow the path of the marginal ray, see Fig. A.2. Secondly we follow the ray that passes through the centre of lens, L_2 and find where it just grazes the limiting aperture. This interception point between these two rays marks the exit pupil. Again in this example we see that the exit pupil is larger than the real limiting aperture.

Exit pupil in a 4-f imaging system

From the discussion of general optical systems in Chapter 3, we now specifically examine how to determine the exit pupil for a 4-f imaging system. We start by looking into the

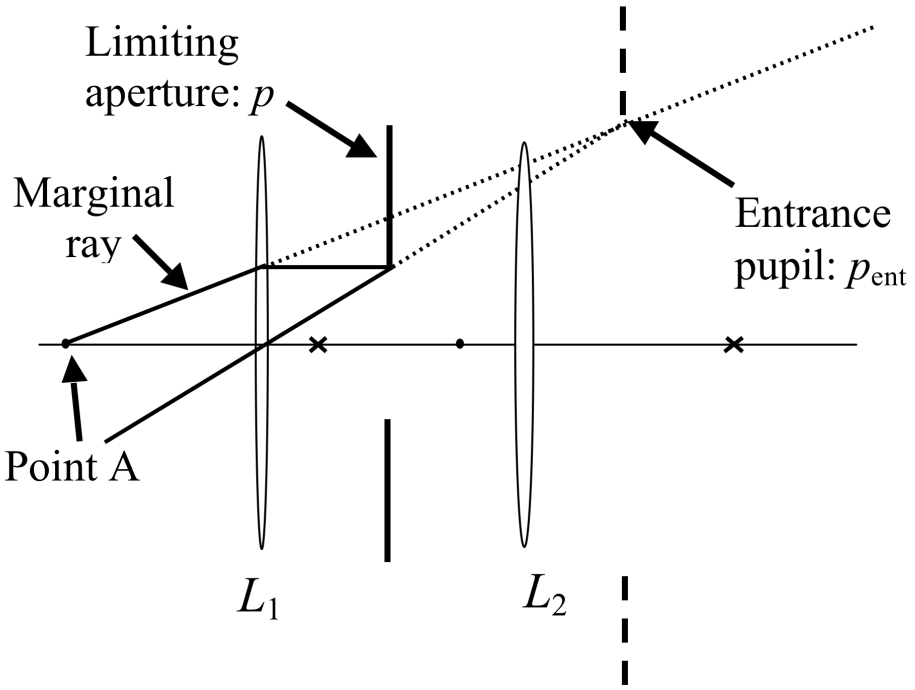

Figure 6.1 – Determining the entrance pupil, figure taken from [40].

imaging system from the output plane. The marginal rays are as usual important and are marked in black in Fig. A.3. We see that the marginal ray is bent by L_2 and just grazes the limiting aperture. Its apparent path is marked as a dashed black line.

We now determine the path of the ray the passes through the centre of L_2 and just grazes the limiting aperture. This ray follows the path marked as a dashed black line. Unlike in the previous examples where these two rays (marked with dashed lines) intercepted each other thereby identifying the location of the entrance or exit pupil plane, here the two rays are parallel and the exit pupil is located at infinity, [7, 40].

Consequently, there are an infinite number of exit pupils in this system and we can however choose any number of exit pupils, geometrically projected down the path that the marginal ray appears to follow. In this case we choose the pupil plane as the plane where the marginal ray intercepts L_2. In this example though it can be shown that the exit pupil and the real limiting aperture have the same size.

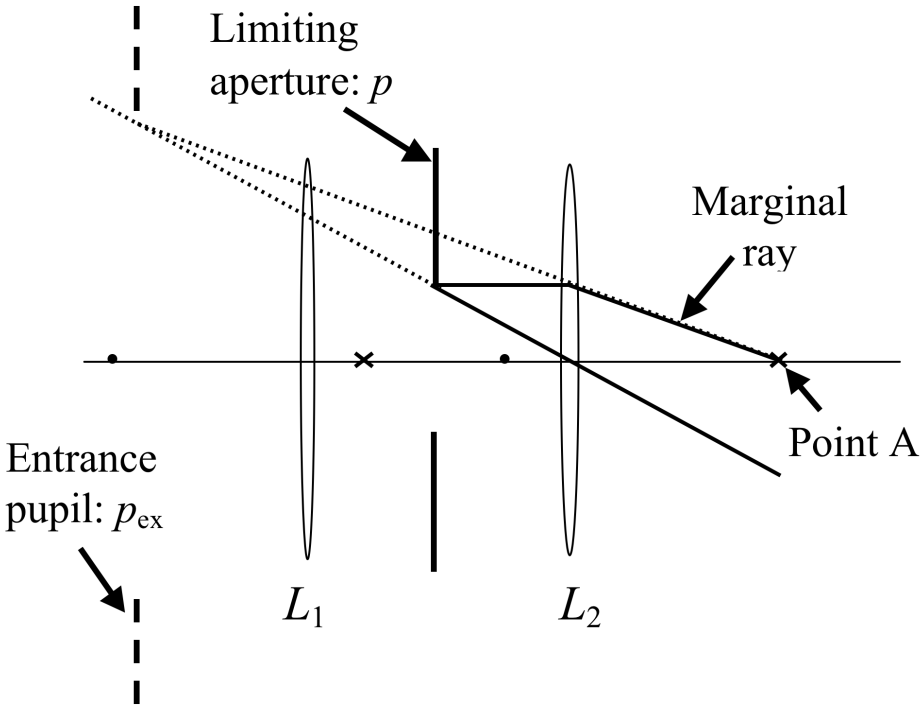

Figure 6.2 – Determining the exit pupil, figure taken from [40].

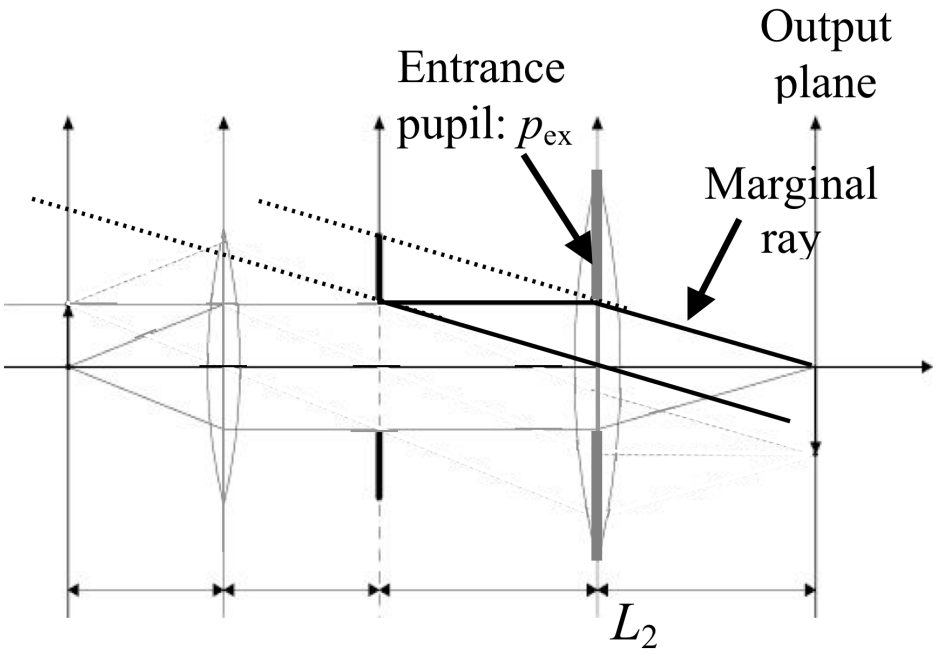

Figure 6.3 – Schematic of a 4-f imaging system.

Bibliography

[1] Dayan Li, Raoul Kirner, Damien P. Kelly, and John T. Sheridan. Speckle: two new metrology techniques, 2012.

[2] Unnikrishnan Gopinathan, John J. Healy, Damien P. Kelly, and John T. Sheridan. *Linear Canonical Transforms: Theory and Applications*, chapter Deterministic Phase Retrieval Using the LCT, pages 331–346. Springer New York, New York, NY, 2016.

[3] Changliang Guo, Dayan Li, Damien P. Kelly, and John T. Sheridan. Measuring refractive index of glass by using two captures under speckle field illumination, 2015.

[4] Matthias Hillenbrand, Damien P. Kelly, and Stefan Sinzinger. Numerical solution of nonparaxial scalar diffraction integrals for focused fields. *J. Opt. Soc. Am. A*, 31(8):1832–1841, Aug 2014.

[5] Matthias Hillenbrand, Armin Hoffmann, Damien P. Kelly, and Stefan Sinzinger. Fast nonparaxial scalar focal field calculations. *J. Opt. Soc. Am. A*, 31(6):1206–1214, Jun 2014.

[6] Damien P. Kelly, Bryan M. Hennelly, Alexander Grün, and Karl Unterrainer. Numerical sampling rules for paraxial regime pulse diffraction calculations. *J. Opt. Soc. Am. A*, 25(9):2299–2308, 2008.

[7] Damien P. Kelly, John T. Sheridan, and William T. Rhodes. Fundamental diffraction limitations in a paraxial 4-f imaging system with coherent and incoherent illumination. *J. Opt. Soc. Am. A*, 24(7):1911–1919, 2007.

[8] Damien P. Kelly, Nitesh Pandey, Bryan M. Hennelly, and Thomas J. Naughton. Quantization noise: An additional constraint for the extended sampling theorem. In *Digital Holography and Three-Dimensional Imaging*, page DWB12. Optical Society of America, 2009.

[9] Damien P. Kelly, Nail Sabitov, Thomas Meinecke, and Stefan Sinzinger. Some considerations when numerically calculating diffraction patterns. In *Digital Holography and Three-Dimensional Imaging*, page DTuC5. Optical Society of America, 2011.

[10] Damien P. Kelly and Daniel Claus. Filtering role of the sensor pixel in fourier and fresnel digital holography. *Appl. Opt.*, 52(1):A336–A345, Jan 2013.

[11] Damien P. Kelly. Numerical calculation of the fresnel transform. *J. Opt. Soc. Am. A*, 31(4):755–764, Apr 2014.

[12] Damien P. Kelly, Bryan M. Hennelly, Alexander Grun, Juraj Darmo, and Karl Unterrainer. Fast numerical algorithm for ultrashort thz pulse diffraction. volume 6697, page 66970Q. SPIE, 2007.

[13] Damien P. Kelly, Bryan M. Hennelly, Nitesh Pandey, Thomas J. Naughton, and William T. Rhodes. Resolution limits in practical digital holographic systems. *Optical Engineering*, 48(9):095801, 2009.

[14] D. P. Kelly, B. M. Hennelly, C. McElhinney, and T. J. Naughton. A practical guide to digital holography and generalized sampling. volume 7072, page 707215. SPIE, 2008.

[15] D. P. Kelly, B. M. Hennelly, N. Pandey, T. J. Naughton, and W. T. Rhodes. Resolution limits in practical digital holographic systems. *Optical Engineering*, Accepted, 2009.

[16] Damien P. Kelly, David S. Monaghan, Nitesh Pandey, Tomasz Kozacki, Aneta Michałkiewicz, Bryan M. Hennelly, and Malgorzata Kujawinska. Digital holographic capture and display: Digital holographic capture and display: futuristic solutions for 3d tv. *Internation Journal of Digital Multimedia Broadcasting*, under review, 2009.

[17] D. P. Kelly, J. J. Healy, and J. T. Sheridan B. M. Hennelly. Quantifying the 2.5d imaging performance of digital holographic systems. *J. Europ. Opt. Soc. Rap. Public.*, 6:11034, 2011.

[18] Damien P. Kelly, Lysann Megel, Thomas Meinecke, and Stefan Sinzinger. A theoretical comparison of fresnel based digital holography and phase retrieval from the transport of intensity equation, 2013.

[19] Damien P. Kelly, Lysann Megel, Thomas Meinecke, and Stefan Sinzinger. *Fringe 2013: 7th International Workshop on Advanced Optical Imaging and Metrology*, chapter Axial Decorrelation of Paraxial Wavefields: Theory and Experiment, pages 213–216. Springer Berlin Heidelberg, Berlin, Heidelberg, 2014.

[20] Damien P. Kelly and John T. Sheridan. *Linear Canonical Transforms: Theory and Applications*, chapter Analyzing Digital Holographic Systems with the LCT, pages 347–365. Springer New York, New York, NY, 2016.

[21] Damien P. Kelly, Thomas Meinecke, Nail Sabitov, Stefan Sinzinger, and John T. Sheridan. Digital holography and phase retrieval: a theoretical investigation, 2011.

[22] Dayan Li, Damien P. Kelly, and John T. Sheridan. Three-dimensional static speckle fields. part i. theory and numerical investigation. *J. Opt. Soc. Am. A*, 28(9):1896–1903, Sep 2011.

[23] Dayan Li, Damien P. Kelly, and John T. Sheridan. Three-dimensional static speckle fields. part ii. experimental investigation. *J. Opt. Soc. Am. A*, 28(9):1904–1908, Sep 2011.

[24] Dayan Li, Damien P. Kelly, Raoul Kirner, and John T. Sheridan. Speckle orientation in paraxial optical systems. *Appl. Opt.*, 51(4):A1–A10, Feb 2012.

[25] Dayan Li, Damien P. Kelly, and John T. Sheridan. Speckle suppression by doubly scattering systems. *Appl. Opt.*, 52(35):8617–8626, Dec 2013.

[26] Dayan Li, Damien P. Kelly, and John T. Sheridan. K speckle: space–time correlation function of doubly scattered light in an imaging system. *J. Opt. Soc. Am. A*, 30(5):969–978, May 2013.

[27] Dayan Li, Damien P. Kelly, and John T. Sheridan. *Fringe 2013: 7th International Workshop on Advanced Optical Imaging and Metrology*, chapter Some Characteristics of Doubly Scattered Speckle Fields, pages 289–292. Springer Berlin Heidelberg, Berlin, Heidelberg, 2014.

[28] Liang Zhao, Yang Wu, Chang-liang Guo, Damien P. Kelly, and John T. Sheridan. Reconstruction of digital holograms from three intensity measurements, 2015.

[29] Dayan Li, Damien P. Kelly, and John T. Sheridan. Experimental exploration of the correlation coefficient of static speckles in fresnel configuration, 2011.

[30] Lysann Megel, Damien P. Kelly, Thomas Meinecke, and Stefan Sinzinger. *Fringe 2013: 7th International Workshop on Advanced Optical Imaging and Metrology*,

chapter Iterative Phase Retrieval and the Important Role Played by Initial Conditions, pages 123–128. Springer Berlin Heidelberg, Berlin, Heidelberg, 2014.

[31] Karen M. Molony, Bryan M. Hennelly, Damien P. Kelly, and Thomas J. Naughton. Reconstruction algorithms applied to in-line gabor digital holographic microscopy. *Optics Communications*, 2010.

[32] David S. Monaghan, Damien P. Kelly, Nitesh Pandey, and Bryan M. Hennelly. Twin removal in digital holography using diffuse illumination. *Opt. Lett.*, 34(23):3610–3612, 2009.

[33] Nail Sabitov, Thomas Meinecke, Damien P. Kelly, and Stefan Sinzinger. Two-step phase-shift interferometry with known but arbitrary reference waves: a graphical interpretation. *Appl. Opt.*, 51(28):6831–6838, Oct 2012.

[34] John Sheridan and Damien P. Kelly. Opto-numeric systems: lenses and pixels. In *Biomedical Optics and 3-D Imaging*, page DTu3C.2. Optical Society of America, 2012.

[35] Jennifer E. Ward, Damien P. Kelly, and John T. Sheridan. Three-dimensional speckle size in generalized optical systems with limiting apertures. *J. Opt. Soc. Am. A*, 26(8):1858–1867, 2009.

[36] Yang Wu, Matthias Hillenbrand, Liang Zhao, Stefan Sinzinger, and Damien P. Kelly. Fresnel transform as a projection onto a nijboer–zernike basis set. *Opt. Lett.*, 40(15):3472–3475, Aug 2015.

[37] Yang Wu, James P. Ryle, Shi Liu, Damien P. Kelly, and Adrian Stern. Experimental evaluation of inline free-space holography systems. *Appl. Opt.*, 54(13):3991–4000, May 2015.

[38] Yang Wu and Damien P. Kelly. Paraxial light distribution in the focal region of a lens: a comparison of several analytical solutions and a numerical result. *Journal of Modern Optics*, 61(sup1):S57–S67, 2014. PMID: 25705089.

[39] Yang Wu, Damien P. Kelly, Adrian Stern, and Stefan Sinzinger. Fluctuations in the intensity read out of ccd/cmos arrays in digital holographic setups: an experimental investigation, 2014.

[40] Damien P. Kelly. *The Analysis of Linear Quadratic Phase Optical Systems and their application to Speckle Based Metrology Systems.* PhD thesis, University College Dublin, 2006.

[41] Damien P. Kelly, Thomas Meinecke, Changliang Guo, Christoph Schierz, and John T. Sheridan. Speckle contrast reduction in display systems: A simple model. In *Laser Display Conference*, 2015.